nagra.

TECHNICAL REPORT 23-06

Sorption Databases for Opalinus Clay, Confining Geological Units and Bentonite: Methods, Concepts and Upscaling of Data

October 2024

Nagra | National Cooperative for the Disposal of Radioactive Waste
Hardstrasse 73 | 5430 Wettingen | Switzerland
T. +41 56 437 11 11 | info@nagra.ch | nagra.ch

nagra.

TECHNICAL REPORT 23-06

Sorption Databases for Opalinus Clay, Confining Geological Units and Bentonite: Methods, Concepts and Upscaling of Data

October 2024

G.D. Miron[1], M. Marques Fernandes[1], D. A. Kulik[1,2], O. Marinich[1], B. Baeyens[1,3], R.A.J. Wüst[4], J.K. Becker[4] & X. Li[4]

[1]PSI, 5232 Villigen, Switzerland

[2]CONGINEER GmbH, 5200 Brugg, Switzerland

[3]CWL Solutions GmbH, 5314 Kleindöttingen, Switzerland

[4]Nagra

Nagra | National Cooperative for the Disposal of Radioactive Waste
Hardstrasse 73 | 5430 Wettingen | Switzerland
T. +41 56 437 11 11 | info@nagra.ch | nagra.ch

The report titled "Sorption Databases for Opalinus Clay, Confining Geological Units and Bentonite: Methods, Concepts and Upscaling of Data" presents the fundamental modelled sorption databases derived from Nagra's extensive deep drilling campaign.

The electronic look-up tables and data are part of Nagra's data management system and available upon request from Nagra.

The authors express their gratitude to Dr. V. Brendler for the careful review and quality assurance of this document. They extend sincere thanks to several key individuals who contributed significantly to this work, specifically M. Montovani, A. Schaible, V. Kalbermatter, and E. Eltayeb for their technical support and the numerous experimental data acquired over the years, which form the foundation of this report. The graphic design team at Nagra are also acknowledged for their efforts in finalising the document and figures. The authors extend special thanks to Nagra for providing financial support, which enabled the successful completion of this study.

ISSN 1015-2636

Abstract

The safety analysis of deep geological repositories relies on values for the retention and transport properties of radionuclides under site-specific geochemical conditions. Retention on mineral surfaces of sedimentary hist rocks and their confining geological units (containment-providing rock zone) is one of the pillars on which the safety analysis is based. Consequently, solid-liquid distribution coefficients (R_d) for dose-relevant elements for the *in-situ* conditions (porewater composition, mineralogy) are required.

This report describes the development of sorption databases (SDBs) that contain element-specific R_d values for the Opalinus Clay and confining geological units in the candidate siting regions and for MX-80 bentonite in their respective porewater types. Delivered in the form of look-up tables with R_d values for varying illite, smectite and illite-smectite mixed layer (ISML) contents in the confining rock units, R_d values were used to expand the available downhole data with high-resolution sorption profiles, and to produce the statistical distributions for the abstracted litho-stratigraphic units used in performance assessments.

The R_d values were calculated within a "one-step" thermodynamic equilibrium system using GEMS codes, which rely on a comprehensive chemical framework based on the state-of-the-art PSI/Nagra TDB 2020, the updated ClaySor sorption model for illite and montmorillonite, and the *in-situ* porewaters for Opalinus Clay and bentonite. This approach has been validated through blind predictions of sorption measurements for key radionuclides on numerous rock samples from cores extracted from deep boreholes across the three siting regions.

Calculations at realistic solid-liquid ratios involved the relevant redox reactions and allowed for competition in cation exchange and surface complexation between divalent cations. For elements with existing thermodynamic sorption model parameters (i.e. selectivity coefficients and surface complexation constants), R_d values were calculated for the site-specific porewater conditions together with the upper and lower bounds of the 95% confidence interval, derived based on the model parameter uncertainties. The resulting R_d values were then arranged into look-up tables for given intervals of the total weight-% of the 2:1 clay minerals illite, smectite and ISML.

The dominant factor influencing the sorption capacity of Opalinus Clay and the confining units is the weight content of illite/smectite/ISML in the rock samples. This factor outweighs other potential sources of variability, such as differences in porewater composition between lithostratigraphic units, which, except for the calcareous units, are not expected to differ significantly. The variability of illite/smectite/ISML content is accounted for in statistical analysis of the sorption data for the abstracted lithostratigraphic units. Look-up tables, along with newly established correlations between the illite/smectite/ISML content and the R_d values, systematically combined with the available high-resolution geological data, allow the calculation of R_d profiles along any stratigraphic profile of known clay mineralogical composition. In this way, the detailed downhole data plots for sorption R_d values can be prepared for reactive transport simulations. The profiles include reference, upper and lower bounding values for each abstracted unit used in performance assessment models. The present approach is superior to that applied in Stage 2 of the Sectoral Plan for Deep Geological Repositories where R_d values for only a few selected units, based on very few samples, represented the SDBs.

Zusammenfassung

Die Sicherheitsanalyse von geologischen Tiefenlagern stützt sich auf Rückhalte- und Transporteigenschaften von Radionukliden unter standortspezifischen geochemischen Bedingungen. Ein zentraler Pfeiler dieser Analyse ist die Quantifizierung der Rückhaltung von Radionukliden an mineralischen Oberflächen des einschlusswirksamen Gebirgsbereichs, der sowohl das Wirtgestein als auch die Rahmengesteine umfasst. Aus diesem Grund werden Feststoff-Flüssigkeits-Verteilungskoeffizienten (R_d) für dosisrelevante Elemente unter in-situ Bedingungen (d. h. Porenwasserzusammensetzung, Mineralogie) benötigt.

Dieser Bericht beschreibt die Entwicklung der Sorptionsdatenbanken (SDBs) für den Opalinuston und die Rahmengesteine in den potenziellen Standortgebieten sowie für den MX-80-Bentonit unter Berücksichtigung ihrer jeweiligen Porenwässer. Die Daten werden in Form von Nachschlagetabellen geliefert und enthalten die R_d-Werte in Abhängigkeit der Zusammensetzung von Illit, Smektit und Illit-Smektit-Wechsellagerungen (ISML) im einschlusswirksamen Gebirgsbereich. Die R_d-Werte dienen der Erweiterung der verfügbaren Bohrlochdaten mit hochauflösenden Sorptionsprofilen und der Erstellung der statistischen Verteilungen für die abstrahierten lithostratigraphischen Einheiten, die zur Prüfung der Barrierenwirksamkeit verwendet werden.

Die R_d-Werte wurden in einem «einstufigen» thermodynamischen Gleichgewichtssystem mit dem GEMS-Code berechnet. GEMS verwendet ein umfassendes chemisches Modell, das die aktuelle PSI/Nagra TDB 2020, das aktualisierte ClaySor-Sorptionsmodell für Illit und Montmorillonit sowie die in-situ Porenwässer von Opalinuston und Bentonit berücksichtigt. Der Ansatz wurde durch Blindvorhersagen von Sorptionsmessungen für wichtige Radionuklide an zahlreichen Gesteinsproben aus Bohrkernen, die im Rahmen von der Tiefbohrkampagne der Nagra in den drei Standortgebieten gewonnen werden konnten, erfolgreich validiert.

Die Berechnungen, die unter realistischen Feststoff-Flüssigkeits-Verhältnissen durchgeführt wurden, berücksichtigten relevante Redoxreaktionen und die Kompetition zwischen zweiwertigen Kationen hinsichtlich Kationenaustausch und Oberflächenkomplexierung. Für Elemente, deren thermodynamische Sorptionsmodellparameter (z.B., Selektivitätskoeffizienten und Oberflächenkomplexierungskonstanten) verfügbar sind, wurden R_d-Werte für die standortspezifischen Porenwasserzusammensetzungen berechnet, einschliesslich der oberen und unteren Grenzwerte des 95-%-Konfidenzintervalls, basierend auf Unsicherheiten in den Modellparametern. Die berechneten R_d-Werte wurden dann in Nachschlagetabellen für bestimmte Intervalle des Gesamtgewichtsanteils der 2:1-Tonminerale (Illit, Smektit und ISML) zusammengefasst.

Die grösste Auswirkung auf die Sorptionskapazität des Opalinustons und der Rahmengesteine hat der Gewichtsanteil an Illit/Smektit/ISML in den Gesteinsproben. Dieser Faktor überwiegt gegenüber anderen potenziellen Variabilitätsquellen, wie etwa Unterschiede in der Porenwasserzusammensetzung zwischen den lithostratigraphischen Einheiten, die – mit Ausnahme der kalkreichen Einheiten – voraussichtlich nicht wesentlich variieren.

Die Variabilität des Gehalts an Illit, Smektit und ISML wird bei der statistischen Analyse der Sorptionsdaten für die abstrahierten lithostratigraphischen Einheiten berücksichtigt. Nachschlagetabellen, zusammen mit neu erstellten Korrelationen zwischen dem Gehalt an Illit, Smektit sowie ISML und den R_d-Werten, systematisch kombiniert mit den verfügbaren hochauflösenden geologischen Daten, ermöglichen die Berechnung von R_d-Profilen entlang eines beliebigen stratigraphischen Profils, deren tonmineralogische Zusammensetzung bekannt ist. Auf diese Weise können die detaillierten Bohrlochdatenplots für R_d-Werte für reaktive Transportsimulationen vorbereitet werden. Die Profile enthalten für jede abstrahierte Einheit, die in den Modellen zur Prüfung der Barrierenwirksamkeit verwendet wurden, Referenzwerte sowie obere und untere Eckwerte. Der vorliegende Ansatz ist besser als der, der in Etappe 2 des Sachplans geologische Tiefenlager angewandt wurde, bei dem R_d-Werte für nur wenige ausgewählte Einheiten, die wiederum auf sehr wenigen Stichproben basierten, die SDBs repräsentierten.

Table of Contents

List of Tables

List of Figures

List of Acronyms

2SPNE SC/CE	2-site protolysis non-electrostatic surface complexation and cation exchange (sorption model)
AM	Arithmetic mean
ATW	Alpha-toxic waste
CA	Component additive (method)
CE	Cation exchange
CEC	Cation exchange capacity
CF	Conversion factor
CRZ	Containment-providing rock zone (defined as the units between the Malm (NL/ZNO) and Klingnau/Hauptrogenstein (JO) aquifers above the Opalinus Clay and the Keuper/Muschelkalk aquifers below the Opalinus Clay)
ENSI	Swiss Federal Nuclear Safety Inspectorate (*Eidgenössisches Nuklearsicherheitsinspektorat*)
FES	Frayed edge sites
GCS	Generalised Cs sorption (model)
GEMS	Gibbs energy minimisation software
GM	Geometric mean
HLW	High-level waste (spent fuel assemblies and high-level waste from reprocessing)
HM	Harmonic mean
ISML	Illite smectite mixed layers
JO	Jura Ost (potential siting region)
L/ILW	Low- and intermediate-level waste
LES	Laboratory for Waste Management
LFER	Linear free energy relationship
LUT	Look-up table
NAB	Nagra Work Report (*Nagra Arbeitsbericht*)
NEA	Nuclear Energy Agency
NTB	Nagra Technical Report (*Nagra Technischer Bericht*)
NL	Nördlich Lägern (potential siting region)
PS	Planar sites
PW	Porewater
RBG	General licence application (*Rahmenbewilligungsgesuch*)

SC	Surface complexation
SDB	Sorption database (R_d values for *in-situ* conditions)
SF	Spent fuel
SFOE	Swiss Federal Office of Energy (*Bundesamt für Energie, BFE*)
SGT	Sectoral Plan for Deep Geological Repositories (*Sachplan geologische Tiefenlager*)
SIT	Specific ion-interaction theory
S/L	Solid-liquid
STDB	Sorption thermodynamic database (model parameters)
T2S	Type II sites
TDB	Thermodynamic database
XRD	X-ray diffraction
ZNO	Zürich Nordost (potential siting region)

List of Symbols

C_{eq}	Total aqueous equilibrium concentration of the element in mol m^{-3}
C_{sorb}	Quantity of sorbed element per unit mass of sorbent in mol kg^{-1}
$CF_{MIN, ROCK}$	Mineralogical conversion factor for rock compositions
$CF_{MIN, BENT}$	Mineralogical conversion factor for bentonite
$G°$	Standard molar Gibbs energy (in its standard state at reference temperature of 25 °C or 298 K and pressure of 1 bar)
MIN_{BENT}	Total bentonite wt.% fraction
MIN_{ROCK}	Total clay mineral wt.% fraction in the rock
$MIN_{IL/SM/ISML}$	Total illite/smectite/ISML wt.% fraction in the rock
MIN_{MONT}	Total montmorillonite wt.% fraction in bentonite
R_d	Solid-liquid distribution coefficient in m^3 kg^{-1}
$R_{d, BENT}$	R_d value for bentonite in m^3 kg^{-1}
$R_{d, IL/SM/ISML}$	R_d value for 100% illite/smectite/ISML in m^3 kg^{-1}
$R_{d, ROCK}$	R_d value for rocks in m^3 kg^{-1}
W_c	Total clay mineral content [wt.%]

1 Introduction

In Switzerland, legal regulations (Nuclear Energy Act (KEG 2003) and Nuclear Energy Ordinance (KEV 2004)) and guidelines are in place for the management of radioactive waste. The Nuclear Energy Ordinance (KEV) classifies Switzerland's radioactive waste into low- and intermediate-level waste (L/ILW), alpha-toxic waste[1] and high-level waste (HLW), the latter comprising spent fuel (SF) and vitrified HLW from reprocessing. The Nuclear Energy Act (KEG) requires the disposal of all these types of radioactive waste in deep geological repositories. The feasibility of this disposal solution was demonstrated for L/ILW in Nagra (1985) and for L/ILW and HLW in Nagra (2002).

The Sectoral Plan for Deep Geological Repositories (SGT) regulates the search for suitable siting regions for the disposal of radioactive waste in Switzerland. This site selection process is conducted in three stages (BFE 2008). Stages 1 (SGT-E1) and 2 (SGT-E2) have already been completed and Nagra is currently in Stage 3 (SGT-E3). In SGT-E3, the three siting regions – Jura Ost (JO), Nördlich Lägern (NL) and Zürich Nordost (ZNO) – located in Northern Switzerland (Fig. 1-1) are being evaluated.

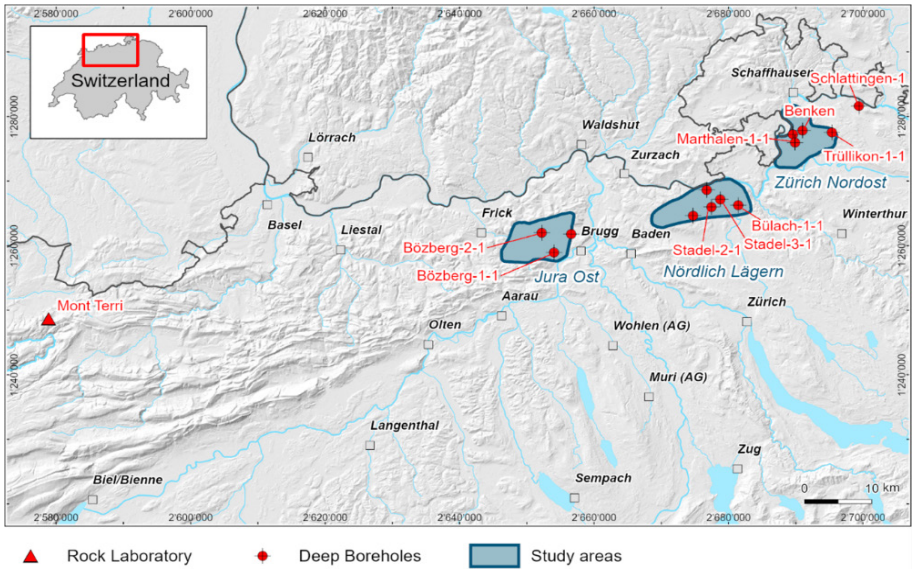

Fig. 1-1: Map of the three siting regions JO, NL and ZNO with the locations of the deep boreholes

[1] According to Nagra (2024a), alpha-toxic waste can coexist with L/ILW within the same emplacement caverns. As a result, for the sake of simplicity, the term L/ILW encompasses alpha-toxic waste without explicit mention.

The disposal of radioactive waste in deep argillaceous rock formations aims to effectively contain radionuclides, preventing their migration into the geosphere and biosphere. In the clay mineral-rich geological barrier of the Opalinus Clay host rock and its confining units (collectively, the containment-providing rock zone, or CRZ), the migration of nuclides will be primarily governed by retention processes, such as sorption onto mineral constituents, and by the extremely low hydraulic conductivities, which result in transport being diffusion-dominated. These processes, particularly sorption within the far-field (i.e. the CRZ) and the near-field (i.e. MX-80 bentonite buffer) of the HLW, are important parameters in safety analysis, allowing critical insights into the geochemical performance of potential disposal sites (Leupin et al. 2017).

The safety assessment for the general licence application (RBG) requires site-specific state-of-the-art sorption databases (SDBs) for relevant radionuclides (Nagra 2024d) across the specific argillaceous barriers of the near- and far-field (i.e. Opalinus Clay, confining units and bentonite buffer). This report compiles SDBs, expressed as solid-liquid distribution coefficients (R_d values), representative of the different rock/water systems for JO, NL and ZNO and for bentonite, at trace concentrations of elements typically below the solubility limits. Since the porewater composition initially defined for ZNO is identical to that for NL (subsequently termed NL-ZNO porewater), the R_d values for ZNO are assumed to be comparable to NL. Therefore, no separate SDBs are compiled for ZNO and they are denoted as NL-ZNO throughout this report. The various aspects related to the development of SDBs for JO, NL-ZNO and MX-80 bentonite, and their respective different porewater types (i.e. reference and high-pCO_2, i.e. partial pressure of CO_2 gas) are comprehensively described.

Chapter 2 briefly outlines the methodology employed to create the SDBs. The site-specific porewater compositions used for the calculations are provided in Chapter 3. The porewaters were defined based on drill core measurements (Mäder & Wersin 2023), with validation conducted for realistic solid-porewater mass ratios in GEMS calculations (Kulik & Miron 2024). Chapter 4 presents the R_d calculation results for 35 radionuclides for the JO and NL-ZNO far-field systems, and for the MX-80 bentonite near-field. Chapter 5 details the derivation of the R_d values presented in look-up tables (LUTs) specific to various ranges and gradations of clay mineral content. These LUTs, combined with the downhole profiles of the clay mineral contents, result in detailed radionuclide sorption profiles for all boreholes and siting regions. Chapter 6 details the calculation of the upper and lower bounds of the 95% confidence interval, based on model parameter uncertainties assessed in Marinich et al. (2024).

The thermodynamic parameters of the ClaySor model used to calculate the R_d values are compiled in App. A.1 to A.4 (Tab. A-1 to Tab. A-6), including surface complexation (SC) constants and selectivity coefficients, which have been re-evaluated in Marinich et al. (2024). App. B summarises the metal hydrolysis equilibrium constants used in the refitting process. A comparison with the SDBs developed in SGT-E2 by Baeyens et al. (2014b) is presented in App. C.

2 Methodology for deriving sorption databases

2.1 Sorption model

Since the sorption properties of the sedimentary rocks and bentonite buffer cannot be practically determined in laboratory experiments because of the numerous combinations of rock-porewater compositions, thermodynamic sorption models have become essential tools for accurately quantifying the sorption of elements across a wide range of geochemical conditions. Over the past three decades, the Laboratory for Waste Management (LES) of the Paul Scherrer Institute (PSI) has dedicated significant research efforts to developing thermodynamic sorption models for key clay minerals, namely montmorillonite and illite. The quasi-mechanistic 2-site protolysis non-electrostatic surface complexation and cation exchange (2SPNE SC/CE) model for montmorillonite (Baeyens & Bradbury 1997, Bradbury & Baeyens 1997) and illite (Bradbury & Baeyens 2009a, Bradbury & Baeyens 2009b) has undergone extensive refinement for a wide range of key elements, including Cs(I), Ra(II), Ni(II), Co(II), Pb(II), Eu(III), Am(III), Th(IV), Sn(IV), Np(V), Pa(V) and U(VI) (Baeyens & Marques Fernandes 2018). For Cs sorption on illite specifically, the Generalised Cs Sorption (GCS) model was developed (Bradbury & Baeyens 2000).

In recent years, these sorption models have been integrated into the GEM-Selektor geochemical code (Kulik et al. 2013) under the name 'ClaySor model' (Kulik et al. 2018). Recent upgrades to these models (Marinich et al. 2024) ensure consistency with the recently updated chemical thermodynamic database (TDB), PSI/Nagra TDB 2020 (Hummel & Thoenen 2023). Standard thermodynamic properties of cation exchange (CE) and surface complexation (SC) constants at 1 bar pressure, and 25 °C temperature and with 95% confidence level uncertainties, were derived by re-fitting experimental sorption data used to develop the 2SPNE SC/CE and GCS models, incorporating current PSI/LES sorption data. For some elements lacking experimental data (i.e. Cd(II) and Fe(II) for illite; Pu(III, IV), Np(IV) and U(IV) for illite and montmorillonite), SC constants were evaluated from linear free energy relationships (LFERs) without uncertainties (Marinich et al. 2024).

The ClaySor model for illite and montmorillonite, along with the aqueous speciation and solubility-limiting solids from the PSI/Nagra TDB 2020, form a coherent chemical system implemented in the GEMS geochemical modelling package and was used in calculations related to porewaters, radionuclide solubility (Hummel et al. 2023, Hummel et al. 2022, Kulik & Miron 2024) and sorption (Marques Fernandes et al. 2024a).

2.2 "Bottom-up" modelling approach

As stated in the introduction, the safety assessment for a deep geological repository requires state-of-the-art SDBs for relevant elements in the Opalinus Clay and confining geological units of the regions JO, NL and ZNO and for bentonite. The present SDBs contain R_d values for elements calculated based on different rock mineralogical compositions and porewater compositions relevant to the individual siting regions. The R_d value is defined as:

$$R_d = \frac{C_{sorb}}{C_{eq}} \text{ (m}^3 \text{ kg}^{-1}\text{)} \qquad 2\text{-}1$$

where $C_{sorb.}$ represents the quantity of sorbed element per unit mass of sorbent (mol kg^{-1}) at its equilibrium total aqueous concentration of $C_{eq.}$ (mol m^{-3}). R_d is equivalent to what is denoted as K_d in the SDBs used for the safety analysis calculations.

In SGT-E2, the R_d values were calculated by multiplying the source R_d values derived from sorption measurements on illite and montmorillonite with different conversion factors to adjust for the change in aqueous complexation and the clay mineral content between the simple system and the *in-situ* conditions (Baeyens et al. 2014b). This methodology was already based on a kind of “simplified” component additive (CA) approach. In this approach, the overall sorption in a system is treated as the sum of sorption contributions from the individual mineral components of the system considered, assuming that each component acts independently. The approach can be significantly streamlined when one mineral component is assumed to dominate sorption (Payne et al. 2013). Within complex mineral/argillaceous water systems, the simplified approach operates under the assumption that the uptake of contaminants can be quantified by focusing on sorption on individual 2:1 clay minerals, such as illite, smectite and illite-smectite mixed layers (ISML), which are considered the primary sorbents.

The calculation methodology used to derive SDBs builds on the same conceptual framework as used in Baeyens et al. (2014b), while using a more comprehensive thermodynamic modelling approach. This enhanced methodology, known as the "bottom-up" approach, incorporates the inhouse thermodynamic ClaySor model specifically developed for illite and montmorillonite. In a defined porewater environment, radionuclide interactions with argillaceous rocks are assumed to be controlled by equilibrium, resulting in a no net mass transfer between the solid phase (the mineral surface) and the aqueous phase (the porewater).

The R_d values for the elements of interest are consistently calculated based on the sorption capacity of illite, smectite and ISML and the input chemical composition under thermodynamic equilibrium conditions. This approach, similar to the smart distribution coefficients method (Stockmann et al. 2017), incorporates a chemical system comprising thermodynamic models for sorption on illite and montmorillonite, an aqueous speciation model, and the consideration of solubility-limiting solids. The use of this thermodynamic framework provides several distinct advantages:

(i) Sorption calculations are conducted in a single, consistent, fully coupled thermodynamic equilibrium step, simultaneously considering aqueous speciation including redox, CE, SC and solubility.

(ii) The method can consider competition between radionuclides, as well as dissolved forms in the pore solution undergoing CE and/or SC on illite and montmorillonite.

The applicability of the bottom-up approach has been demonstrated for several types of radionuclides on various argillaceous rocks and bentonite in their respective porewaters (Marques Fernandes et al. 2015, Marques Fernandes & Baeyens 2021, Bradbury & Baeyens 2011). Furthermore, this approach was recently verified through blind predictions of experimentally determined sorption isotherms for Cs(I), Ni(II), Eu(III), Th(IV) and U(VI) in their corresponding synthetic porewaters on nearly 100 rock samples taken from deep drill cores originating from the NL, ZNO and JO siting regions (Marques Fernandes et al. 2024a), concluding that this thermodynamic approach is a reliable tool for estimating the sorption properties of sedimentary rocks in Northern Switzerland provided that the 2:1 clay minerals are the dominant retention phases.

In the present report, SDBs for Opalinus Clay, rock types from the confining units and MX-80 bentonite were developed. For Opalinus Clay and the confining units, the clay minerals illite, smectite, and ISML are assumed to control sorption and are collectively represented by a single sorbent, namely illite. Experimental and modelling studies have demonstrated similar SC behaveiour between illite and montmorillonite (Bradbury & Baeyens 2017, Baeyens & Bradbury 2017, Baeyens & Marques Fernandes 2018), allowing sorption on illite to be treated as representative for both minerals. A similar assumption is applied ISML, simplifying the treatment of sorption across these clay mineral systems. The potential contributions of kaolinite (a 1:1 clay mineral) and chlorite (also a 2:1 clay mineral) to the overall sorption in the argillaceous rocks have not

been considered. While these minerals have a significantly lower cation exchange capacity (CEC) (Allard et al. 1983), they certainly contribute to sorption through SC on amphoteric edge sites. However, comparable thermodynamic sorption models for kaolinite and chlorite, similar to those available for illite and montmorillonite, are currently lacking. As such, the current sorption SDBs, derived without considering the contribution of kaolinite and chlorite, remain conservative. In the case of MX-80 bentonite, montmorillonite is the main clay mineral, up to 90 weight percentage (wt.%) and is therefore assumed to be the dominant sorbing phase.

2.3 Thermodynamic calculations

For elements with available thermodynamic SC constants and selectivity coefficients (Marinich et al. 2024), R_d values were directly calculated using the ClaySor model in GEMS, incorporating sorption site capacities and species along with their thermodynamic properties, while accounting for CE competition on planar sites. These R_d values were derived in a "one-step" process within a single, consistent chemical system, integrating all necessary models and databases defined in the GEMS geochemical modelling package (Kulik et al. 2013). For divalent transition metals, competition on SC sites, with Fe(II) and Mn(II) present in the porewaters, was also considered (Marques & Baeyens 2019, Marques Fernandes & Baeyens 2020, Orucoglu et al. 2022). In all cases, solubility and aqueous speciation for each element were evaluated for the different argillaceous rock/porewater systems of the JO and NL-ZNO Opalinus Clay and confining units, as well as for MX-80 bentonite.

GEMS calculates chemical equilibrium for given input conditions, yielding the concentration of the element in all phases, and allowing the evaluation of R_d values for *in-situ* modelled pore solutions (composition, pH, Eh and I). The R_d values obtained are then scaled stepwise for different clay mineral contents in the different rock systems and collected into the LUTs (Chapter 5).

Three main components are relevant in the methodology for producing site-specific R_d values:

(i) The state-of-the-art PSI/Nagra TDB 2020 (Hummel & Thoenen 2023) serving as the reference thermodynamic data source for all substances describing aqueous speciation and mineral solubility.

(ii) The 2SPNE SC/CE models for illite and montmorillonite and the GCS model for illite, implemented in the GEMS code as the ClaySor model, together with the model parameter values from Marinich et al. (2024) which are summarised in App. A.

(iii) Input data for these calculations include the different porewater compositions (i.e. reference and high-pCO_2) for JO, NL-ZNO and for bentonite given in Chapter 3.

The R_d values were generally calculated at trace concentrations of the element of interest by adding 10^{-11} to 10^{-7} mol kg^{-1} illite or montmorillonite as the sorbing element as input to the equilibrium calculation, with the upper bound depending on the solubility limit and sorption capacity. For elements that are part of the pore solution composition, the sorption was calculated at the highest aqueous concentration, set by the solubility-limiting solid as a boundary condition.

For elements lacking a specific ClaySor model, chemical analogues were used as a basis for estimation. Tab. 2-1 outlines the key differences between the SDB methodology used in SGT-E2 (Baeyens et al. 2014b) and in SGT-E3 (this report).

Tab. 2-1: Methodologies used for the SDB calculations in SGT-E2 (Baeyens et al. 2014b) and SGT-E3 (this report)

	NTB 12-04 (Baeyens et al. 2014b)	**This report**
Sorption model	2SPNE SC/CE + GCS (status as of 2012)	ClaySor (2SPNE SC/CE + GCS) with STDB 2023 (parameter uncertainties at 95% confidence level) (Marinich et al. 2024)
PSI/Nagra TDB version	TDB 12/07 (Thoenen et al. 2014)	TDB 2020 (Hummel & Thoenen 2023)
Upscaling	Bottom-up approach, sorption on 2:1 clay minerals, scaling with illite/smectite/ISML mineral content wt.%. sorption reduction through aqueous speciation in porewater	
R_d values	Reference source values taken from the modelled experimental data at trace concentrations and adjusted to *in-situ* conditions with correction factors; speciation calculated separately using PHREEQC	R_d values directly calculated from the full illite and montmorillonite sorption models and porewater speciation in systems computed in GEMS using the ClaySor model + PSI/Nagra TDB 2020
Validation	Sorption measurements on generic argillaceous rock samples (Bradbury & Baeyens 2000) and on Opalinus Clay and MX-80 bentonite (Baeyens et al. 2014a)	Sorption measurements on pristine drill core samples from JO, NL and ZNO siting regions (Marques Fernandes et al. 2024a)
Uncertainty	Uncertainty of the source data or model calculations (a factor of 3 or higher) Uncertainty in speciation (Monte Carlo calculations)	Upper and lower bounds of the 95% confidence interval of calculated R_d values based on parameter uncertainties of the sorption model for a given radionuclide
Sorption database	R_d values for different types of sedimentary rocks: Opalinus Clay, Brauner Dogger, Effingen Member and Helvetic Marls with fixed illite/smectite contents and for MX-80 bentonite with fixed montmorillonite content	LUTs with R_d values for Opalinus Clay and CRZ in JO, NL and ZNO siting regions for different illite/smectite/ISML contents and for MX-80 bentonite with three different montmorillonite contents

3 Porewater chemistry of the near- and far-field

The composition of porewaters for argillaceous rocks of the near- and far-field is assumed to be governed by chemical equilibrium with the surrounding mineral assemblages. The only variable considered is the total inorganic carbon (TIC) concentrations, expressed as pCO_2. While local and temporal variations in porewater composition may occur, the predominance of argillaceous rocks and the long timescales involved make the assumption of a strongly buffered porewater composition highly reliable. Although the relative proportions of minerals may shift over time, the composition of the porewaters remains stable as long as the overall mineral assemblage remains unchanged.

3.1 Near-field: MX-80 bentonite

The near-field reference bentonite porewater, referred to as E3-BPW-Ref, is based on calculations by Curti (2023) performed using GEMS and the PSI7Nagra TDB 2020 with the specific ion-interaction (SIT) aqueous activity model. These calculations consider the representative Opalinus Clay porewater model for the NL siting region, assuming equilibrium with montmorillonite and the following mineral phases: barite ($BaSO_4$), calcite ($CaCO_3$), dolomite ($CaMg(CO_3)_2$), celestite ($SrSO_4$), kaolinite ($Al_2Si_2O_5(OH)_4$), gypsum ($CaSO_4 \cdot 2H_2O$), quartz (SiO_2), rhodochrosite ($MnCO_3$), magnetite ($Fe^{II}Fe^{III}{}_2O_4$), and pyrite ($Fe^{II}S_2$). A second variant, E3-BPW-high-pCO_2, representing the highest expected TIC concentration, is selected as a bounding case. Details on the modelling approach are given in Curti (2023).

The porewater compositions given in Tab. 3-1 were used as input for calculating the LUTs for MX-80 bentonite. For bentonite, only montmorillonite is assumed to be the sorbent, and in the ClaySor calculations, the site capacities were therefore scaled to the montmorillonite wt.%.

Tab. 3-1: Porewater compositions for MX-80 bentonite (E3-BPW)
From Curti (2023).

System characteristics	**Reference**	**High-pCO_2**
pH	7.24	7.05
Eh [mV]	-173.0	-159.0
Log pCO_2 [bar]	-2.20	-1.80
Ionic strength [mol kg^{-1}]	0.45	0.45
Solutes	***Concentration*** [mol kg^{-1} H_2O]	
Na	3.75E-01	3.66E-01
K	1.83E-03	1.79E-03
Mg	1.02E-02	9.78E-03
Ca	1.77E-02	1.69E-02
Sr	1.72E-04	1.64E-04
Al	2.08E-08	2.39E-08
Fe	2.09E-05	4.65E-05
Mn	1.84E-05	1.86E-05
Si	1.70E-04	1.70E-04
Cl	2.39E-01	2.40E-01
S(VI)	7.85E-02	8.30E-02
C(IV)[2]	2.94E-03	4.99E-03
F	1.74E-04	1.74E-04

3.2 Far-field: Opalinus Clay and confining units

The reference porewater compositions for the Opalinus Clay and the CRZ in the JO, NL and ZNO siting regions are based on the geochemical concepts and model calculations of Mäder & Wersin (2023) using the PHREEQC code and the PSI/Nagra TDB 2020 with the SIT aqueous activity model and were implemented in GEMS. These porewaters were constrained in agreement with squeezing and advective displacement measurements of natural samples from deep boreholes located in the JO, NL and ZNO siting regions (Kiczka et al. 2023). As mentioned before, due to strong similarities in composition, NL and ZNO are treated as a single porewater composition referred to as NL-ZNO. For each region, additional high-pCO_2 variants were defined using the highest expected TIC concentration. The porewater compositions for the JO and NL-ZNO siting regions are shown in Tab. 3-2. The main differences between the two porewater systems are their ionic strengths of 0.17 M for JO and 0.31 M for NL-ZNO. This difference in salinity essentially affects the retention of elements that sorb through CE. Noteworthy for the NL-ZNO porewater is

[2] C(IV) refers to the dissolved inorganic carbon.

the slightly lower redox potential and the higher concentration of Fe and Mn, which impacts the sorption of divalent cations through competition (Orucoglu et al. 2022, Marques & Baeyens 2019, Marques Fernandes & Baeyens 2020).

The sorption database R_d LUTs for the JO and NL-ZNO siting regions were calculated for the porewater compositions given in Tab. 3-2. Only illite, smectite and ISML are assumed to be the sorbents, with sorption behaviour similar to that of illite. The calculations were performed using the ClaySor model for illite and the site capacities were scaled to the illite/smectite/ISML wt.% contents.

Tab. 3-2: Porewater compositions for the JO and NL-ZNO siting regions

From Mäder & Wersin (2023).

	JO		**NL-ZNO**	
	Reference	**High-pCO_2**	**Reference**	**High-pCO_2**
System characteristics				
pH	7.34	7.13	7.08	6.86
Eh [mV]	-180.7	-166.5	-163.5	-148.5
Log pCO_2 [bar]	-2.2	-1.8	-2.2	-1.8
Ionic strength [mol kg^{-1}]	0.17	0.17	0.32	0.34
Solutes	***Concentration*** [mol kg^{-1} H_2O]			
Na	1.29E-01	1.21E-01	1.99E-01	2.04E-01
K	8.31E-04	8.21E-04	1.13E-03	1.17E-03
Mg	4.47E-03	4.65E-03	1.49E-02	1.55E-02
Ca	7.59E-03	7.90E-03	2.52E-02	2.80E-02
Sr	1.93E-04	1.94E-04	3.71E-04	3.80E-04
Al	2.40E-08	2.83E-08	2.60E-08	2.71E-08
Fe	3.40E-05	3.50E-05	9.80E-05	1.07E-04
Mn	2.91E-05	3.05E-05	9.65E-05	1.00E-04
Si	1.76E-04	1.76E-04	1.73E-04	1.72E-04
Cl	8.50E-02	9.20E-02	2.40E-01	2.70E-01
S(VI)	2.77E-02	2.75E-02	2.34E-02	2.40E-02
C(IV) [3]	3.20E-03	5.16E-03	2.11E-03	3.43E-03
F	2.19E-04	2.16E-04	1.59E-04	1.55E-04

[3] C(IV) refers to the dissolved inorganic carbon.

4 Sorption databases for JO, NL-ZNO and MX-80 bentonite

The R_d values were determined using GEMS version 3.9.6 (Kulik et al. 2013) and its Python interface to GEMS, based on the compositions of rocks from the CRZ of the three siting regions and MX-80 bentonite, along with their respective porewaters. These calculations employed the PSI/Nagra TDB 2020 (Hummel & Thoenen 2023) and the ClaySor model for illite and montmorillonite incorporating the updated sorption thermodynamic database (STDB) (Marinich et al. 2024).

4.1 Safety-relevant elements

The safety-relevant radionuclides from SF, HLW and L/ILW were defined in NTB 24-18 (Nagra 2024d) and are listed in Tab. 4-1. Note that some elements are associated with more than one waste type. Compared to the SDB in SGT-E2 (Baeyens et al. 2014b), the current SDB includes several additional elements, namely Al, Cf, Fe, Hg and Si, while K, Be and Co are no longer part of the present SDB.

Tab. 4-1: Dose-relevant elements with associated waste types considered in the present report (Nagra 2024d)

Element	SF, HLW	L/ILW
Ac	√	√
Ag	√	√
Al		√
Am	√	√
C	√	√
Ca	√	
Cf	√	√
Cl	√	√
Cm	√	√
Cs	√	√
Eu	√	
Fe		√
Hg		√
Ho	√	

Tab. 4-1: Cont.

Element	SF, HLW	L/ILW
I	√	√
Mo	√	√
Nb	√	√
Ni	√	√
Np	√	√
Pa	√	√
Pb	√	√
Pd	√	
Po	√	√
Pu	√	√
Ra	√	√
Se	√	√
Si		√
Sm	√	
Sn	√	√
Sr	√	√
Tc	√	
Th	√	√
Ti	√	√
U	√	√
Zr	√	

Fig. 4-1 provides a periodic table overview of the 35 elements considered in the SDB. The figure highlights the main sorption uptake mechanism (i.e. CE, SC) and calculation approaches for each element (i.e. ClaySor (CE, SC), chemical analogy (LFER), special cases), as well as the non-sorbing elements. Four radionuclides occur in different oxidation states in the porewaters and, depending on the redox state, belong to different groups. Each of these groups are detailed in the following sections.

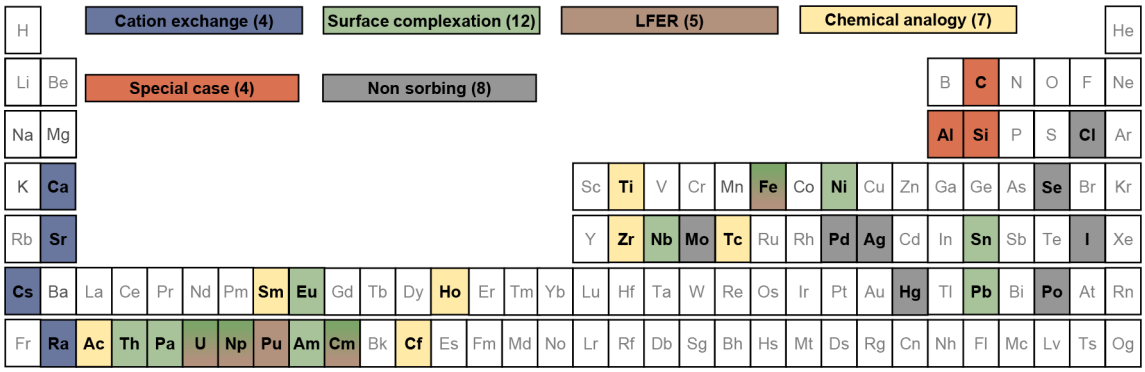

Fig. 4-1: Chemical elements considered in the SDB

The elements are grouped by the calculation approach used and their main sorption mechanisms under the prevailing conditions of the porewaters. Elements shown in two colours are treated differently for different oxidation states or are modelled differently for sorption on either illite or montmorillonite.

4.2 Cs, Ca, Sr and Ra: cation exchange modelling

The sorption of Ca, Sr and Ra occurs mainly via CE and is thus calculated using the ClaySor CE sorption model for illite and montmorillonite (Marinich et al. 2024). The GCS model was used in the case of Cs sorption on illite. Values for the selectivity coefficients (K_c) of these elements with respect to Na on both illite and montmorillonite are given in App. A.2 and A.3 (Tab. A-2, Tab. A-3 and Tab. A-4), respectively. For the SDB calculations, CE competition on illite and montmorillonite are taken into account, considering the major alkaline and alkaline-earth metals present in the porewaters, i.e. Na, K, Mg, Ca and Sr.

The results of the R_d calculations for Cs, Ca, Sr and Ra at 100 wt.% clay mineral content are summarised in Tab. 4-2 together with the aqueous speciation in the porewater compositions for JO, NL-ZNO and MX-80 bentonite. In the case of Cs, the sorption values for the argillaceous rocks of JO, NL and ZNO are much higher compared to those for the MX-80 bentonite since Cs sorption is dominated by the frayed edge sites (FES) of illite, whereas Cs adsorbs weaker on the planar sites (PS) sites of montmorillonite. A similar trend is observed for Ra because of the higher selectivity of Ra for illite than for montmorillonite (see Tab. 4-2). It should be noted that the retardation of Ra is also affected by recrystallisation of accessory sulphates with formation of $(Ba,Sr,Ra)SO_4$ solid solutions (Brandt et al. 2020, Vinograd et al. 2018), which was not considered in these calculations. Aqueous speciation of the elements in this group is dominated by free aqueous cations. For Cs, there are no aqueous complexes, whereas ion pairs of sulphate with alkaline-earth metals comprise ~10 to 30 mol% of total dissolved concentration.

Tab. 4-2: R_d values for Cs, Ca, Sr and Ra for JO, NL-ZNO and MX-80 bentonite and total aqueous concentration for each radionuclide and their speciation for the different porewaters

	JO		NL-ZNO		MX-80 bentonite	
Porewater	**Reference**	**High-pCO_2**	**Reference**	**High-pCO_2**	**Reference**	**High-pCO_2**
Caesium						
R_d (m^3 kg^{-1})	**8.14E+00**	**8.16E+00**	**5.38E+00**	**5.31E+00**	**3.51E-02**	**3.61E-02**
$Cs_{aq\ TOT}$ (mol L^{-1})	1.22E-11	1.22E-11	1.86E-11	1.88E-11	4.15E-09	4.03E-09
Aqueous speciation (mol%)						
Cs^+	100	100	100	100	100	100
Calcium						
R_d (m^3 kg^{-1})	**3.21E-03**	**3.35E-03**	**1.18E-03**	**1.10E-03**	**2.81E-03**	**2.91E-03**
$Ca_{aq\ TOT}$ (mol L^{-1})	7.59E-03	7.90E-03	2.52E-02	2.80E-02	1.71E-02*	1.64E-02*
Aqueous speciation (mol%)						
Ca^{2+}	71.7	71.4	85.2	85.3	67.7	66.2
$CaSO_4^0$	27.4	27.3	14.4	14.0	31.8	33.1
Strontium						
R_d (m^3 kg^{-1})	**3.24E-03**	**3.38E-03**	**1.18E-03**	**1.10E-03**	**2.95E-03**	**3.05E-03**
$Sr_{aq\ TOT}$ (mol L^{-1})	1.93E-04	1.94E-04	3.71E-04	3.80E-04	1.65E-04*	1.59E-04*
Aqueous speciation (mol%)						
Sr^{2+}	72.6	72.3	85.8	85.9	68.9	67.3
$SrSO_4^0$	26.4	26.2	13.7	13.3	30.6	31.8
Radium						
R_d (m^3 kg^{-1})	**2.15E+00**	**2.22E+00**	**7.59E-01**	**7.04E-01**	**2.59E-02**	**2.62E-02**
$Ra_{aq\ TOT}$ (mol L^{-1})	4.68E-11	4.49E-11	1.32E-10	1.42E-10	5.61E-09	5.56E-09
Aqueous speciation (mol%)						
Ra^{2+}	73.4	73.2	86.6	86.7	70.1	68.6
$RaSO_4^0$	25.8	25.6	13.0	12.7	29.4	30.7

* Includes SC not accounted for in the model pore solution listed in Tab. 3-1.

4.3 Surface complexation modelling: Fe, Ni, Pb, Eu, Am, Sn, Th, Pa and Nb

For the elements Fe, Ni, Pb, Eu, Am, Sn, Th, Pa and Nb considered in this section, the R_d values were calculated for their prevalent oxidation states in the porewaters: i.e. (+II) for Fe, Ni and Pb, (+III) for Eu and Am, (+IV) for Sn and Th and (+V) for Pa and Nb. Calculations were conducted using GEMS and the ClaySor model (Marinich et al. 2024) with the K_c values and SC constants given in App. A4 (Tab. A-5 and Tab. A-6). The ClaySor model parameters for these elements were derived from experimental data, and the calculations were carried out following the methodology described in Chapter 2.

The calculated R_d values for each radionuclide at 100% clay mineral content are summarised in the following tables for the three rock-porewater systems (Tab. 4-3 and Tab. 4-4). The aqueous species of elements in the corresponding porewater are also presented, their concentrations (Tab. 4-3) are influenced by their surface complexation, which was not considered in the porewater calculations (Tab. 3-1 and Tab. 3-2) and only protolysis reactions were taken into account. In Tab. 4-3, alongside the R_d values and total dissolved concentrations of elements, their aqueous speciation fractions (expressed in mol%) are provided. These fractions may exhibit slight variations from those speciation fractions given in Kulik & Miron (2024, Tab. B-2) due to the effect of surface complexations on the speciation calculations of solubility limits. The R_d results and the potential influence of aqueous speciation are briefly discussed below. The aqueous metal complexes present at levels below 1 mol% are not shown in the tables.

4.3.1 Divalent transition and heavy metals: Fe, Ni and Pb

The calculated R_d values and aqueous speciation for Fe, Ni and Pb are summarised in Tab. 4-3. An important distinction from previous SDBs is that the R_d calculations for these metals now incorporate competitive sorption with Mn^{2+} and Fe^{2+}, which are natural constituents in the porewaters. The concentrations of these ions in porewaters are determined by equilibria with magnetite or siderite and pyrite for Fe and rhodochrosite for Mn. By taking competition into account, the sorption is lowered since large parts of SC are shifted from the low-capacity high affinity strong sites to the high-capacity lower affinity weak sites. Competition on the strong sites is controlled by the strength of their SC constants and the concentration of the competing cations (Marques & Baeyens 2019, Marques Fernandes & Baeyens 2020). The R_d values for Fe were calculated at the porewater equilibrium concentration. For the reference NL-ZNO system, for example, the following sequence of R_d values can be observed from Tab. 4-3: Pb > Fe ~ Ni. This sequence is reflected by the strength of the SC constants on strong and weak sites on illite as illustrated in App. A.4 (Tab. A-5). On montmorillonite, a similar trend is seen for these metals, however, the R_d values are generally lower as the SC constants are weaker than on illite. The aqueous speciation shown in Tab. 4-3 indicates that the adsorbing free metal species are present at levels from ~10 mol% (Pb) to ~60 mol% (Fe, Ni).

Tab. 4-3: Summary of the R_d values and aqueous speciation mole fractions of Fe, Ni and Pb for JO, NL-ZNO and MX-80 bentonite

The model pore waters were calculated in their respective reports without using the surface complexation model for Fe and Mn (only a simple clay model with protolysis reactions and CE was used). R_d and aqueous concentration values calculated in this table were done with full SC for Mn and Fe, therefore the aqueous concentrations of Mn and Fe in the PW are not the same (but close) in the porewater and SDB tables.

	JO		**NL-ZNO**		**MX-80 bentonite**	
Porewater	**Reference**	**High-pCO_2**	**Reference**	**High-pCO_2**	**Reference**	**High-pCO_2**
pH	**7.34**	**7.14**	**7.07**	**6.87**	**7.24**	**7.05**
Ferrous iron						
R_d (m^3 kg^{-1})	**3.09E-01**	**3.05E-01**	**2.79E-01**	**2.57E-01**	**1.24E+00**	**6.96E-01**
$Fe_{aq\ TOT}$ (mol L^{-1})	1.62E-05	1.67E-05	3.58E-05	4.09E-05	1.67E-05	3.67E-05
Aqueous speciation (mol%)						
Fe^{2+}	43.3	43.3	64.4	65.6	46.5	46.3
$FeSO_4^0$	28.0	28.7	22.6	22.5	44.1	43.8
$FeCO_3^0$	27.9	27.3	12.2	11.1	7.6	8.0
Nickel						
R_d (m^3 kg^{-1})	**1.23E-01**	**1.35E-01**	**1.04E-01**	**1.04E-01**	**1.80E-02**	**1.30E-02**
$Ni_{aq\ TOT}$ (mol L^{-1})	8.12E-10	7.36E-10	9.57E-10	9.60E-10	8.04E-09	1.11E-08
Aqueous speciation (mol%)						
Ni^{2+}	42.7	48.1	58.5	64.3	47.0	47.1
$NiSO_4^0$	22.9	26.0	19.7	18.1	36.2	40.4
$NiSiO(OH)_3^+$	31.0	21.6	16.9	11.7	13.7	9.1
$NiCl^+$	1.3	1.6	3.8	4.5	2.4	2.3

Tab. 4-3: Cont.

	JO		NL-ZNO		MX-80 bentonite	
Porewater	**Reference**	**High-pCO_2**	**Reference**	**High-pCO_2**	**Reference**	**High-pCO_2**
Lead						
R_d (m^3 kg^{-1})	**8.90E+00**	**8.24E+00**	**8.34E+00**	**7.02E+00**	**6.10E-01**	**3.33E-01**
$Pb_{aq\ TOT}$ (mol L^{-1})	1.12E-11	1.21E-11	1.20E-11	1.42E-11	2.40E-10	4.39E-10
Aqueous speciation (mol%)						
Pb^{2+}	8.8	8.5	12.4	11.6	12.1	11.1
$PbOH^{+}$	4.7	2.8	3.5	1.9	3.0	1.8
$PbCO_3^0$	44.6	41.3	18.2	15.0	15.3	15.6
$PbHCO_3^{+}$	12.5	18.6	8.5	11.8	7.2	8.3
$Pb(CO_3)_2^{2-}$	3.7	3.3	<1	<1	<1	<1
$PbCO_3Cl^{-}$	4.0	4.0	4.7	4.4	4.0	4.1
$PbCl^{+}$	7.8	8.1	26.6	27.3	20.1	18.2
$PbCl_2^0$	1.5	2.8	13.7	15.7	9.3	11.0
$PbCl_3^{-}$	<1	<1	2.7	3.4	1.8	1.6
$PbSO_4^0$	11.0	10.5	8.2	7.3	21.0	21.4
$Pb(SO_4)_2^{2-}$	<1	<1	<1	<1	4.8	5.5

4.3.2 Trivalent lanthanides and actinides: Eu and Am

The calculated R_d values and aqueous speciation for Eu and Am in the different rock/porewater systems are summarised in Tab. 4-4. The sorption values for both elements are within the same order of magnitude. In the case of JO and NL-ZNO, the R_d values for Eu are higher compared to Am, whereas the opposite trend is observed for sorption on MX-80 bentonite. The aqueous speciation is very similar for both elements and is dominated by carbonate, sulphate and silicate complexes. Eu and Am are selected as chemical analogues for Ho and Sm and for Ac, Cm and Cf, respectively (see Section 4.4).

Tab. 4-4: Summary of R_d values and aqueous speciation of Eu and Am for JO, NL-ZNO and MX-80 bentonite

	JO		NL-ZNO		MX-80 bentonite	
Porewater	**Reference**	**High-pCO_2**	**Reference**	**High-pCO_2**	**Reference**	**High-pCO_2**
pH	**7.34**	**7.14**	**7.07**	**6.87**	**7.24**	**7.05**
Europium						
R_d (m^3 kg^{-1})	**8.18E+00**	**6.40E+00**	**1.22E+01**	**1.03E+01**	**3.27E+00**	**2.15E+00**
$Eu_{aq\ TOT}$ (mol L^{-1})	1.22E-11	1.56E-11	8.17E-12	9.69E-12	4.48E-11	6.80E-11
Aqueous speciation (mol%)						
Eu^{3+}	2.3	2.6	8.6	10.4	5.1	5.2
$EuCO_3^+$	58.9	63.0	43.1	46.4	39.4	42.4
$EuSO_4^+$	19.3	13.3	15.5	18.0	22.3	23.9
$Eu(SO_4)_2^{2-}$	3.9	4.3	2.6	3.0	11.15	12.5
$EuSiO(OH)_3^{2+}$	12.0	13.2	26.9	18.8	18.9	12.8
Americium						
R_d (m^3 kg^{-1})	**4.08E+00**	**3.85E+00**	**7.74E+00**	**7.91E+00**	**1.50E+01**	**1.07E+01**
$Am_{aq\ TOT}$ (mol L^{-1})	1.12E-11	1.21E-11	1.20E-11	1.42E-11	2.40E-10	4.39E-10
Aqueous speciation (mol%)						
Am^{3+}	2.8	3.1	10.6	13.0	7.1	7.3
$AmCO_3^+$	55.8	60.4	42.2	46.2	43.5	48.1
$Am(CO_3)_2^{2-}$	9.6	10.0	2.3	2.3	5.1	6.0
$AmHCO_3^{2+}$	1.6	2.9	2.6	4.7	2.1	3.5
$AmSiO(OH)_3^{2+}$	22.8	15.8	32.4	23.0	25.8	17.4
$AmSO_4^+$	5.1	5.7	6.6	7.8	10.8	11.8
$Am(SO_4)_2^{2-}$	<1	1.1	<1	<1	3.8	4.5

4.3.3 Tetravalent Sn and Th and pentavalent Pa and Nb

For Sn(IV), Th(IV), Pa(V) and Nb(V), SC models are available and the methodology described in Chapter 2 is applicable. The results of R_d and aqueous speciation calculations in the different rock / porewater systems are summarised in Tab. 4-5. In the case of Th, the negatively charged hydroxo-carbonato complexes are dominant and this reduces the R_d values (since no ternary surface complex- is considered in the ClaySor model for Th). For Pa and Sn, the presence of non-sorbing aqueous complexes is negligible. On the other hand, the aqueous speciation of Nb is dominated by the non-sorbing, negatively charged hydroxy complexes. Nonetheless, this effect is accounted for in the thermodynamic equilibrium model calculations as the sorption is still high for this element.

Tab. 4-5: Summary of the R_d values and aqueous speciation of Th, Pa, Sn and Nb for JO, NL-ZNO and MX-80 bentonite

	JO		**NL-ZNO**		**MX-80 bentonite**	
Porewater	**Reference**	**High-pCO_2**	**Reference**	**High-pCO_2**	**Reference**	**High-pCO_2**
pH	**7.34**	**7.14**	**7.07**	**6.87**	**7.24**	**7.05**
Thorium						
R_d (m^3 kg^{-1})	**3.78E+01**	**1.99E+01**	**6.58E+01**	**3.75E+01**	**3.52E+01**	**1.69E+01**
$Th_{aq\ TOT}$ (mol L^{-1})	2.64E-11	5.01E-11	1.52E-11	2.66E-11	4.15E-11	8.66E-11
Aqueous speciation (mol%)						
$Th(OH)_4^0$	7.7	4.1	13.48	7.8	8.1	4.0
$Th(OH)_3CO_3^-$	50.8	42.1	53.51	46.9	48.4	53.0
$Th(OH)_2(CO_3)_2^{2-}$	38.5	49.6	27.82	37.1	40.3	38.9
$Th(OH)_2CO_3^0$	2.7	3.6	4.8	7.0	2.9	3.6
Protactium						
R_d (m^3 kg^{-1})	**7.63E+01**	**7.29E+01**	**7.25E+01**	**6.70E+01**	**5.14E+01**	**5.14E+01**
$Pa_{aq\ TOT}$ (mol L^{-1})	1.31E-11	1.37E-11	1.38E-11	1.49E-11	2.85E-11	2.85E-11
Aqueous speciation (mol%)						
$PaO(OH)_3^0$	98.2	98.2	98.1	97.5	98.1	97.9
$PaO(OH)^{2+}$	1.2	1.1	1.3	2.1	1.0	1.4
Tin						
R_d (m^3 kg^{-1})	**3.15E+02**	**3.20E+02**	**3.22E+02**	**3.30E+02**	**1.33E+03**	**1.45E+03**
$Sn_{aq\ TOT}$ (mol L^{-1})	3.17E-12	3.12E-12	3.10E-12	3.03E-12	1.10E-12	1.01E-12
Aqueous speciation (mol%)						
$Sn(OH)_4^0$	93.1	95.6	95.8	97.4	93.7	95.8
$Sn(OH)_5^-$	6.9	4.4	4.2	2.6	6.2	4.2
Niobium						
R_d (m^3 kg^{-1})	**3.44E+01**	**3.46E+01**	**4.34E+01**	**4.66E+01**	**1.32E+02**	**1.31E+02**
$Nb_{aq\ TOT}$ (mol L^{-1})	2.90E-12	2.88E-12	2.30E-12	2.15E-12	1.11E-12	1.11E-12
Aqueous speciation (mol%)						
$Nb(OH)_5^0$	<1	<1	<1	<1	<1.0	1.4
$Nb(OH)_6^-$	97.8	98.3	98.1	98.0	97.5	97.6
$Nb(OH)_7^{2-}$	1.8	1.2	1.2	1.3	1.5	1.0

4.3.4 Mixed oxidation state elements: U(IV/VI), Np(IV/V) and Pu(III/IV/V)

Pu, Np and U prevail in several oxidation states under the given redox conditions defined by the porewater compositions. U occurs as +IV and +VI, Np as +IV and +V and Pu as +III, +IV and +V. The derivation of the R_d values for each of these radionuclides is briefly described below.

Uranium

The ClaySor model parameters used in the SDB calculations were derived for hexavalent U based on experimental sorption data and for tetravalent U based on LFER estimates for both illite and montmorillonite (Marinich et al. 2024). The calculations were conducted for fully coupled redox conditions set by the porewater composition. The sorption of U in the porewaters is predicted to be as U(VI) SC, whereas the aqueous speciation of U is dominated by the ternary UO_2-Ca-CO_3 complex (Tab. 4-6). There is a clear and strong disproportionation between adsorbed and solid uranium that exists in the tetravalent state in reducing porewater systems and the aqueous dissolved uranyl in the hexavalent state. The latter is due to high TIC and Ca porewater concentrations resulting in large stability fields of UO_2-CO_3 and UO_2-Ca-CO_3 complexes.

Neptunium

For both illite and montmorillonite, Np(V) sorption parameters were derived from experimental data, while Np(IV) sorption parameters were based on LFER, detailed in Marinich et al. (2024) and given in App. A.4 (Tab. A-5 and Tab. A-6). The calculated R_d values together with the main aqueous speciation are given in Tab. 4-6. The adsorbed Np is predicted to be tetravalent, with the aqueous Np(IV) hydroxo-carbonato complex being dominant across all porewater compositions.

Plutonium

The Pu sorption model parameters were derived by Marinich et al. (2024) based on LFER estimates for Pu(III) and Pu(IV) sorption on both illite and montmorillonite. The SC reactions and equilibrium constants derived from this approach are given in App. A.4 (Tab. A-5 and Tab. A-6). For Pu, the dominant oxidation state is trivalent in both porewaters and surface complexes, as shown in Tab. 4-6. A significant fraction of the Pu(III) is present as carbonato and hydroxo-silicato complexes and the minor contribution of Pu(IV) and Pu(V) comprises carbonato and hydroxo-carbonato complexes.

Tab. 4-6: Summary of the R_d values and aqueous speciation of U, Np and Pu for JO, NL-ZNO and MX-80 bentonite

	JO		**NL-ZNO**		**MX-80 bentonite**	
Porewater	**Reference**	**High-pCO_2**	**Reference**	**High-pCO_2**	**Reference**	**High-pCO_2**
pH	**7.34**	**7.14**	**7.07**	**6.87**	**7.24**	**7.05**
Uranium						
R_d (m^3 kg^{-1})	**3.74E-02**	**2.04E-02**	**6.63E-02**	**3.54E-02**	**5.91E-01**	**1.91E-01**
$U_{aq\ TOT}$ (mol L^{-1})	2.66E-09	4.85E-09	1.50E-09	2.81E-09	2.48E-10	7.66E-10
Aqueous speciation (mol%)						
$Ca_2U^{VI}O_2(CO_3)_3^0$	70.9	72.0	86.2	87.2	67.9	66.5
$CaU^{VI}O_2(CO_3)_3^{2-}$	22.5	22.0	11.0	10.4	22.2	23.1
$U^{VI}O_2(CO_3)_3^{4-}$	3.2	3.1	1.1	<1	6.5	7.2
Neptunium						
R_d (m^3 kg^{-1})	**3.75E+00**	**2.53E+00**	**1.49E+01**	**1.06E+01**	**6.78E+01**	**2.86E+01**
$Np_{aq\ TOT}$ (mol L^{-1})	2.67E-11	3.96E-11	6.72E-12	9.39E-12	2.16E-12	5.11E-12
Aqueous speciation (mol%)						
$Np^{IV}(OH)_2(CO_3)_2^{2-}$	94.9	97.8	88.4	94.7	95.4	98.1
$Np^{IV}(OH)_4^0$	4.9	2.1	11.2	5.0	4.5	1.7
Plutonium						
R_d (m^3 kg^{-1})	**1.60E+01**	**1.20E+01**	**2.15E+01**	**1.64E+01**	**2.04E+01**	**1.07E+01**
$Pu_{aq\ TOT}$ (mol L^{-1})	6.25E-12	8.30E-12	4.64E-12	6.08E-12	7.17E-12	1.37E-11
Aqueous speciation (mol%)						
Pu^{3+}	2.3	2.7	8.7	10.8	5.0	5.3
$Pu^{III}OH^{2+}$	1.4	1.0	2.2	1.6	1.5	1.1
$Pu^{III}CO_3^+$	45.3	51.5	33.8	37.4	30.2	33.7
$Pu^{III}SiO(OH)_3^{2+}$	19.6	14.4	30.8	22.5	21.2	14.5
$Pu^{III}SO_4^+$	10.4	12.2	13.7	16.3	19.2	21.3
$Pu^{III}(SO_4)_2^{2-}$	4.0	4.8	2.9	3.5	13.5	16.0
$Pu^{III}Cl^{2+}$	<1	<1	3.5	4.7	1.6	1.7
$Pu^{IV}CO_3(OH)^{3-}$	8.3	3.9	2.1	<1	3.8	2.0
$Pu^{V}(CO_3)^{2-}$	7.8	8.5	1.8	1.9	3.5	4.2

4.4 Chemical analogues

Chemical analogues were used for elements with either unavailable or highly uncertain experimental data and therefore no sorption model was developed for these elements. This approach assumes that the sorption R_d values are approximately similar, within the experimental uncertainty, for chemically similar elements (similar ionic radii, oxidation states, hydrolysis behaviour).

Tab. 4-7 summarises the elements and their chemical analogues used in this work. Their R_d values, together with the upper and lower boundary values, were taken as equal in the SDB. No differences in aqueous speciation were considered, since the analogy assumes similar speciation and sorption.

Trivalent lanthanides and actinides are known to show a similar chemical behaviour with respect to solubility, speciation and sorption, and chemical analogy is often used to estimate missing properties.

The hydrolysis behaviour of the tetravalent elements listed in Tab. 4-7 is very strong and Th is taken as a chemical analogue. However, it should be noted that there is no strong argument for why the tetravalent Th is the most suitable analogue for tetravalent Tc, Ti, or Zr. This uncertainty regarding the choice of analogues can be reduced by additional sorption experiments for these elements. Compared to the R_d values of SGT-E2, presented in App. C, for which alternative analogues were used, the newly selected values are within the uncertainties of the previously selected values, except for Zr, which, based on Th analogy in this report, is predicted to have a lower sorption, and, is thus conservative.

Tab. 4-7: Summary of chemical analogues used for elements where no sorption model is available

Chemical analogue	Elements
Eu(III)	Ho(III), Sm(III)
Am(III)	Ac(III), Cm(III), Cf(III)
Th(IV)	Tc(IV), Ti(IV), Zr(IV)

4.5 Special cases

Inorganic carbon

The methodology for deriving R_d values for inorganic carbon is similar to the one used in SGT-E2. The main sorption mechanism for inorganic carbon ($H^{14}CO_3^-/^{14}CO_3^{2-}$) is assumed to be isotope exchange on calcite surfaces (Cowan et al. 1990, Davis et al. 1987). Stipp et al. (1994) and Stipp et al. (1996) showed that Ca in the first approximately 30 monolayers of calcite, i.e. to a depth of ~10^{-8} m, is readily accessible within a matter of a few months. Considering this and taking the accessible surface area of intact calcite to be ~0.1 $m^2\ g^{-1}$ (Bradbury & Baeyens 1998), the volume of calcite available for isotopic exchange is ~10^{-6} $m^3\ kg^{-1}$. For a calcite density of 2,700 kg m^{-3}, this converts to ~2.7×10^{-3} kg kg^{-1}, or ~0.3 wt.% of pure calcite. This estimate is certainly conservative since more calcite is likely to become available over time.

If 0.3 wt.% of the bulk calcite is taken to be available for exchange with $H^{14}CO_3^-/^{14}CO_3^{2-}$, then the total number of moles of exchangeable carbonate in the solid phase is 2.7×10^{-2} mol kg^{-1}. Thus, the $H^{14}CO_3^-/^{14}CO_3^{2-}$ sorption values for the different groundwaters can be readily obtained using their respective aqueous concentrations and considering 100 wt.% calcite. The actual calcite contents of the rock samples or MX-80 bentonite can be used to reduce the R_d values in the LUTs. In Tab. 4-8, the calculated R_d values for inorganic ^{14}C are presented for JO, NL-ZNO and MX-80 bentonite in their respective porewater compositions.

Tab. 4-8: Calculated inorganic ^{14}C R_d values for JO, NL-ZNO and MX-80 bentonite

	JO		**NL-ZNO**		**MX-80 bentonite**	
Porewater	**Reference**	**High-pCO_2**	**Reference**	**High-pCO_2**	**Reference**	**High-pCO_2**
pH	**7.34**	**7.14**	**7.07**	**6.87**	**7.24**	**7.05**
Isotopically exchangeable calcite	2.70E-02 mol kg^{-1}					
Aqueous C(IV) conc. (mol L^{-1})	3.20E-03	5.16E-03	2.11E-03	3.43E-03	2.98E-03	5.03E-03
R_d (m^3 kg^{-1})	**8.44E-03**	**5.23E-03**	**1.28E-02**	**7.87E-03**	**9.06E-03**	**5.37E-03**

Aluminium and silicon

For Al and Si, no sorption models on illite or montmorillonite are available. Both elements, however, constitute major elemental compositions of clay minerals. To derive R_d values for both metals, a similar approach as for inorganic ^{14}C was applied. Illite and montmorillonite exhibit 0.08 mol kg^{-1} amphoteric edge sites, which are assumed to be available for isotopic exchange with Al and Si present in the porewater. The ratio of the exposed edge sites to the corresponding aqueous concentration of both elements makes it possible to derive R_d values for the case considering 100 wt.% illite or montmorillonite. The results are summarised in Tab. 4-9. The R_d values for Al are ~4 orders of magnitude higher compared to those for Si, which can be explained by rather low Al concentrations in the porewaters compared to Si concentrations.

Tab. 4-9: Calculated Al and Si R_d values for JO, NL-ZNO and MX-80 bentonite

	JO		NL-ZNO		MX-80 bentonite	
Porewater	**Reference**	**High-pCO_2**	**Reference**	**High-pCO_2**	**Reference**	**High-pCO_2**
Aluminium						
Isotopically exchangeable Al (mol kg^{-1})			0.080			
$Al_{aq\ TOT}$ (mol L^{-1})	2.40E-08	2.83E-08	2.60E-08	2.71E-08	2.07E-08	2.36E-08
R_d (m^3 kg^{-1})	**3.34E+03**	**2.82E+03**	**3.08E+03**	**2.95E+03**	**3.86E+03**	**3.40E+03**
Silicon						
Isotopically exchangeable Si (mol kg^{-1})			0.080			
$Si_{aq\ TOT}$ (mol L^{-1})	1.76E-04	1.76E-04	1.73E-04	1.72E-04	1.69E-04	1.69E-04
R_d (m^3 kg^{-1})	**4.54E-01**	**4.55E-01**	**4.64E-01**	**4.66E-01**	**4.73E-01**	**4.72E-01**

4.6 Non-sorbing elements

The non-sorbing elements, Ag, Cl, Hg, I, Mo, Pd, Po and Se have been assigned an R_d values of zero. The elements Cl, I and Mo, which are predicted to be stable in the aqueous phase only as anionic species, are assumed to be non-sorbing. Cl and I are present as free negatively charged non-complexed aqueous ions. Dissolved Mo is predicted to be present in the hexavalent state, predominantly as the molybdate anion, MoO_4^{2-}, and with ~14 to 31 mol% as calcium molybdate species.

Based on experimental observations, it is suggested that some elements can exist as zerovalent neutral aqueous species, e.g. $S^0_{(aq)}$ and $Hg^0_{(aq)}$. In the updated PSI/Nagra TDB 2020, zerovalent neutral aqueous species were proposed for Ag, Se, Pd and Po. These data are evaluated as highly uncertain, but suitable for qualitative and scoping calculations (Hummel & Thoenen 2023).

For the porewater compositions under consideration, calculations predict that Ag, Hg, Se, Pd and Po elements are stable in the aqueous phase only as zerovalent species and are, therefore, conservatively accounted for as non-sorbing elements. Test calculations, performed by suppressing these zerovalent aqueous species, predict that chloride and anionic sulphur species would otherwise dominate. Thus, considering this negative charge, designating these elements as non-sorbing remains valid, regardless of the uncertainty in the properties of the zerovalent neutral species.

Collectively, the assumptions made for non-sorbing elements are conservative, particularly regarding the non-hydroxo neutral zerovalent species. Hydrolysed cations that form neutral hydroxo-species in certain pH ranges and non-hydroxo neutral zerovalent species may still react with the clay mineral surface or form colloidal particles that may contribute to retardation in argillaceous rocks.

Tab. 4-10: Calculated aqueous complexation of non-sorbing elements in the porewater compositions of JO, NL-ZNO and MX-80 bentonite (mol%)

	JO		NL-ZNO		MX-80 bentonite	
Porewater	**Reference**	**High-pCO_2**	**Reference**	**High-pCO_2**	**Reference**	**High-pCO_2**
Mo						
$Mo^{VI}O_4^{2-}$	85.8	85.4	70.6	69.0	85.2	86.0
$CaMo^{VI}O_4(aq)$	14.1	14.6	29.4	30.9	14.7	13.9
Cl^-	100	100	100	100	100	100
I^-	100	100	100	100	100	100
Ag^0	100	100	100	100	100	100
Hg^0	100	100	100	100	100	100
Se^0	100	100	100	100	100	100
Pd^0	100	100	100	100	100	100
Po^0	100	100	100	100	100	100

4.7 Summary of the SDBs for JO, NL-ZNO and MX-80 bentonite

Tab. 4-11 summarises the R_d values derived for the two far-field rock systems, JO and NL-ZNO and the near-field MX-80 bentonite for the two porewater composition variants (reference and high-pCO_2) considered in this report. This table forms the basis for the LUTs used to describe sorption along the depth profiles of boreholes from potential repository sites as discussed in Chapter 5.

Tab. 4-11: SDBs for JO and NL-ZNO (100 wt.% illite/smectite/ISML) and for MX-80 bentonite (100 wt.% montmorillonite) (R_d in m^3 kg^{-1})

	JO		NL-ZNO		MX-80 bentonite	
Porewater	**Reference**	**High-pCO_2**	**Reference**	**High-pCO_2**	**Reference**	**High-pCO_2**
Ac	4.08E+00	3.85E+00	7.74E+00	7.91E+00	1.50E+01	1.07E+01
Ag	0.00E+00	0.00E+00	0.00E+00	0.00E+00	0.00E+00	0.00E+00
Al	3.34E+03	2.82E+03	3.08E+03	2.95E+03	3.86E+03	3.40E+03
Am	4.08E+00	3.85E+00	7.74E+00	7.91E+00	1.50E+01	1.07E+01
C^{IV}	8.47E-03	5.25E-03	1.29E-02	7.89E-03	9.06E-03	5.37E-03
Ca	3.21E-03	3.35E-03	1.18E-03	1.10E-03	2.81E-03	2.91E-03
Cf	4.08E+00	3.85E+00	7.74E+00	7.91E+00	1.50E+01	1.07E+01
Cl	0.00E+00	0.00E+00	0.00E+00	0.00E+00	0.00E+00	0.00E+00
Cm	4.08E+00	3.85E+00	7.74E+00	7.91E+00	1.50E+01	1.07E+01
Cs	8.14E+00	8.16E+00	5.38E+00	5.31E+00	3.51E-02	3.61E-02
Eu	8.18E+00	6.40E+00	1.22E+01	1.03E+01	3.27E+00	2.15E+00
Fe	3.09E-01	3.05E-01	2.79E-01	2.57E-01	1.24E+00	6.96E-01
Hg	0.00E+00	0.00E+00	0.00E+00	0.00E+00	0.00E+00	0.00E+00
Ho	8.18E+00	6.40E+00	1.22E+01	1.03E+01	3.27E+00	2.15E+00
I	0.00E+00	0.00E+00	0.00E+00	0.00E+00	0.00E+00	0.00E+00
Mo	0.00E+00	0.00E+00	0.00E+00	0.00E+00	0.00E+00	0.00E+00
Nb	3.44E+01	3.46E+01	4.34E+01	4.66E+01	1.32E+02	1.31E+02
Ni	1.23E-01	1.35E-01	1.04E-01	1.04E-01	1.80E-02	1.30E-02
Np^{IV}	3.74E+00	2.52E+00	1.49E+01	1.06E+01	6.76E+01	2.86E+01
Pa	7.63E+01	7.29E+01	7.25E+01	6.70E+01	5.14E+01	5.14E+01
Pb	8.90E+00	8.24E+00	8.34E+00	7.02E+00	6.10E-01	3.33E-01
Pd	0.00E+00	0.00E+00	0.00E+00	0.00E+00	0.00E+00	0.00E+00
Po	0.00E+00	0.00E+00	0.00E+00	0.00E+00	0.00E+00	0.00E+00
$Pu^{III/IV}$	1.60E+01	1.20E+01	2.15E+01	1.64E+01	2.04E+01	1.07E+01
Ra	2.15E+00	2.22E+00	7.59E-01	7.04E-01	2.59E-02	2.62E-02
Se	0.00E+00	0.00E+00	0.00E+00	0.00E+00	0.00E+00	0.00E+00
Si	4.55E-01	4.56E-01	4.65E-01	4.68E-01	4.73E-01	4.72E-01
Sm	8.18E+00	6.40E+00	1.22E+01	1.03E+01	3.27E+00	2.15E+00
Sn	3.15E+02	3.20E+02	3.22E+02	3.30E+02	1.33E+03	1.45E+03
Sr	3.24E-03	3.38E-03	1.18E-03	1.10E-03	2.95E-03	3.05E-03
Tc	3.78E+01	1.99E+01	6.58E+01	3.75E+01	3.52E+01	1.69E+01
Th	3.78E+01	1.99E+01	6.58E+01	3.75E+01	3.52E+01	1.69E+01
Ti	3.78E+01	1.99E+01	6.58E+01	3.75E+01	3.52E+01	1.69E+01
$U^{IV/VI}$	3.74E-02	2.04E-02	6.63E-02	3.54E-02	5.91E-01	1.91E-01
Zr	3.78E+01	1.99E+01	6.58E+01	3.75E+01	3.52E+01	1.69E+01

[$] For inorganic ^{14}C, 100 wt.% calcite is considered.

The R_d values for the reference and high-pCO_2 porewater variants compiled in Tab. 4-11 were graphically compared for JO, NL-ZNO and MX-80 bentonite in Fig. 4-2a, Fig. 4-2b and Fig. 4-2c, respectively. The error bars depict the upper and lower values of the 95% confidence intervals calculated using the uncertainties of model parameters detailed in Chapter 6. For the elements C, Ca, Sr, Fe, Al, Pu, Np, Si and U, for which no model uncertainty can be obtained from the available measured data, the error bars represent an assumed sorption model uncertainty factor of 3, as in Baeyens et al. (2014b). The observable differences in Fig. 4-2 originate solely from the difference in the porewater composition since the SDBs refer to a 100 wt.% clay mineral content. Hence, the porewater compositions, within the assumed pCO_2 range, have only a limited influence on the SDBs compiled in this report.

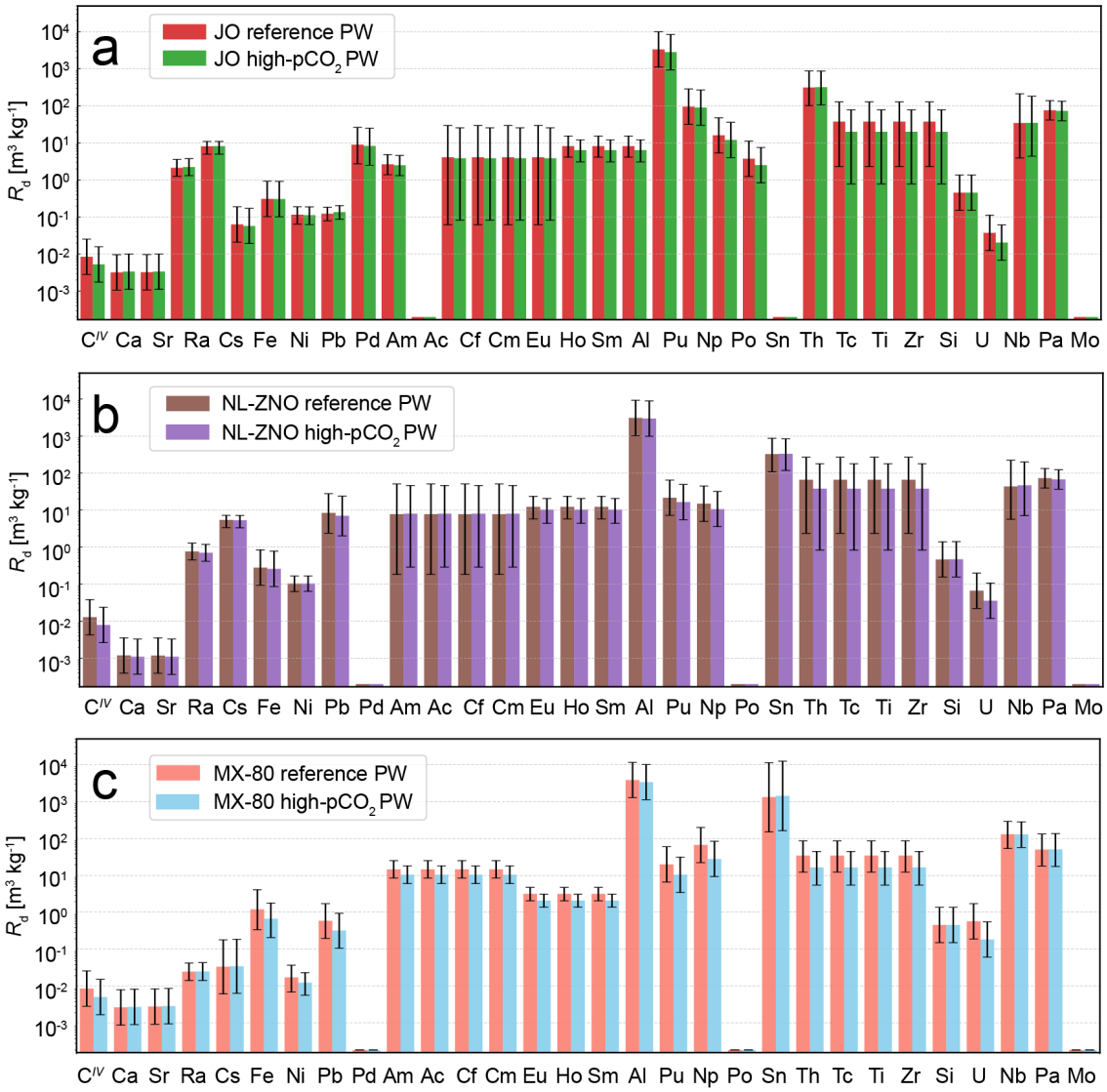

Fig. 4-2: Comparison of calculated R_d values for SGT-E3 using the new methodology for reference and high-pCO_2 porewaters

(a) JO, (b) NL-ZNO and (c) MX-80 bentonite.

Fig. 4-3 compares the SDBs for the two geological environments, i.e. Opalinus Clay and confining units of JO and NL-ZNO, for both reference and high-pCO_2 porewater composition variants. This comparison demonstrates that the SDBs for JO and NL-ZNO are remarkably similar and hence, are independent of the rock type. Any apparent differences originate from the different porewater compositions of the siting regions. As mentioned before, the influence of the porewater composition has only a limited influence on the calculated R_d values compiled for both regions.

Hence, these results suggest that, based on the sorption properties alone, there is no apparent preference for one particular siting region. However, in Chapter 5, a more precise picture is presented of the SDBs when applied for the different deep boreholes.

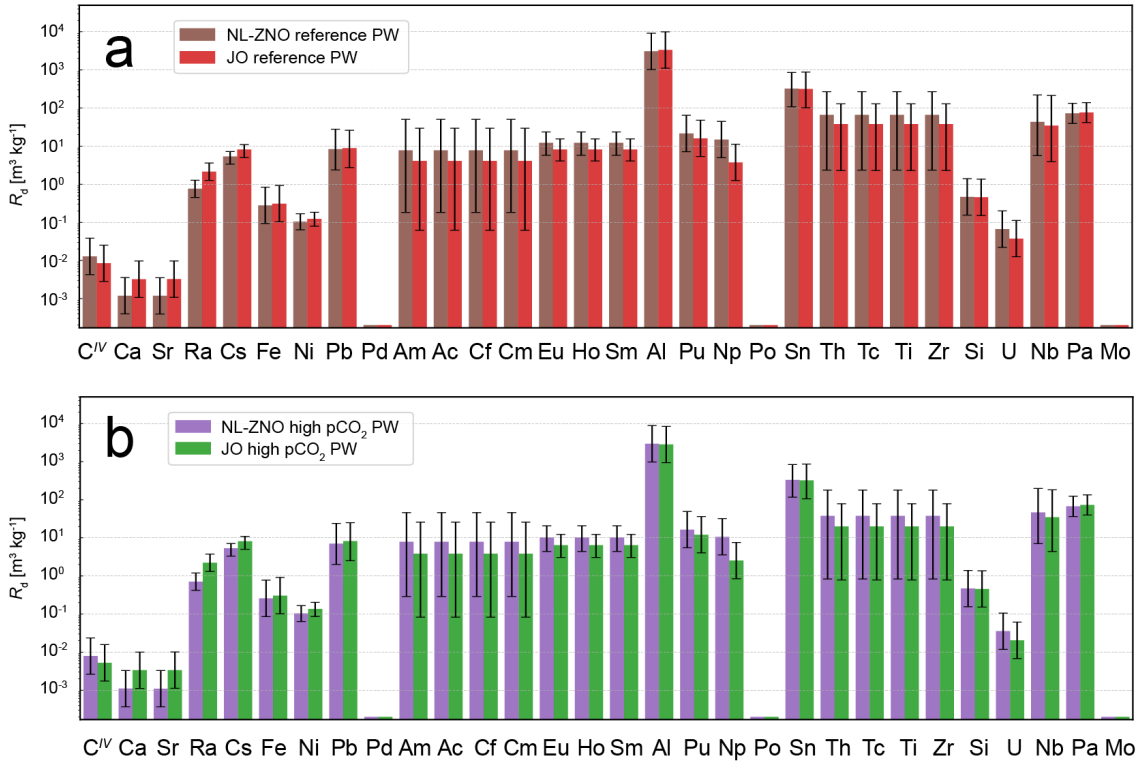

Fig. 4-3: Comparison of R_d values for JO and NL-ZNO

(a) Reference porewater and (b) high-pCO_2 porewater.

5 Sorption data LUTs and applications for safety assessment

5.1 Methodology

The SDBs for *in-situ* conditions were produced in the form of LUTs by re-scaling the calculated R_d values for different illite/smectite/ISML contents to total clay mineral contents of Opalinus Clay and rocks of the CRZ ($R_{d,\ ROCK}$) and to different montmorillonite contents of MX-80 bentonite ($R_{d,\ BENT}$). These tables list columns of the $R_{d,\ ROCK}$ and $R_{d,\ BENT}$ values calculated for the reference and high-pCO_2 porewater compositions for JO and NL-ZNO (Tab. 3-2) and for the porewater compositions of MX-80 bentonite (Tab. 3-1). For each column with calculated R_d values, two additional columns are given that contain the upper and lower bounds of the 95% confidence interval are also given (see Chapter 6 for details). This section details the methodology for generating LUTs for the far-field is detailed. An example of the results is presented for Cs and Eu in Tab. 5-1. SDBs for bentonite are shown in Tab. 5-2.

5.1.1 LUTs for the far-field: Opalinus Clay and CRZ

The methodology is similar to that used for SGT-E2 (Baeyens et al. 2014b) where a mineralogy conversion factor was introduced, which takes into account the differences in mineralogy between the R_d values obtained on pure illite/smectite/ISML and the illite/smectite/ISML wt.% of the rock samples. In the previous SDBs, only few selected units (e.g. Opalinus Clay, Effinger Member, Brauner Dogger) based on reference mineralogy and detailed clay mineralogy (i.e. illite/smectite/ ISML wt.%) were selected. In contrast, the present approach is based on the extensive dataset (150 samples) derived during Nagra's recent deep borehole campaign.

Hence, according to measurements of CECs on 150 rock samples across all major geological units within the CRZ and thus representative of the amount of 2:1 clay minerals (Marques et al. 2024b), an average illite/smectite/ISML mass fraction of the total clay mineral component of 0.64 was obtained from the empirical linear relation based on the available extensive mineralogical data (Nagra 2024a). This is illustrated in Fig. 5.1 showing a clear corelation between the total clay mineral content (including all clay minerals) and the total of the illite/smectite/ISML content.

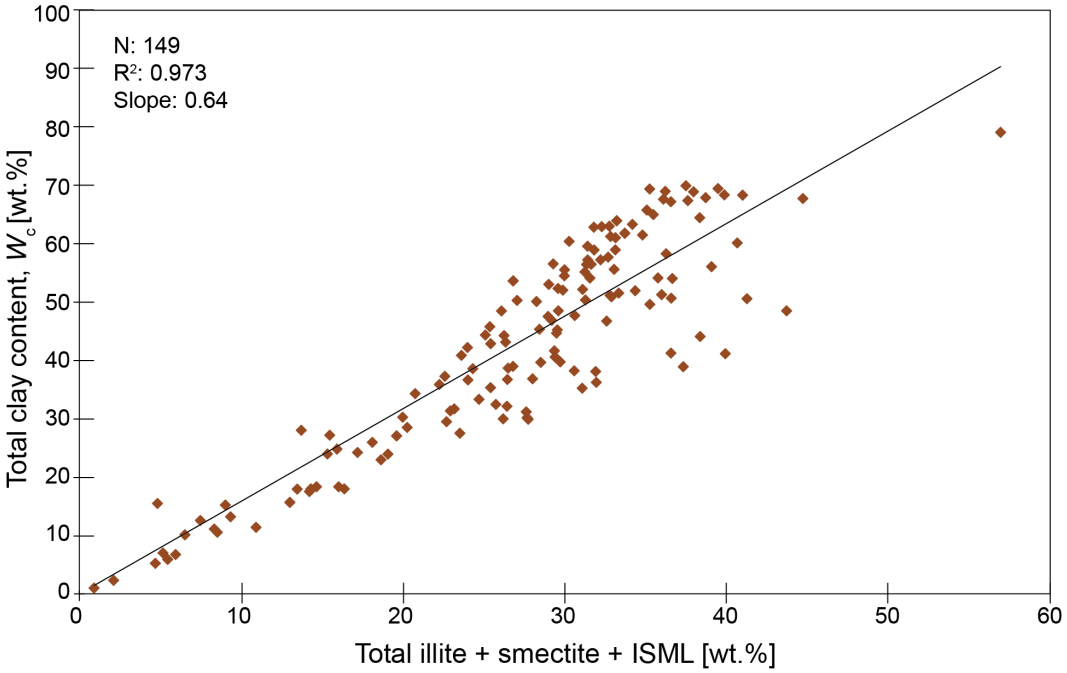

Fig. 5-1: Total clay mineral content versus total illite/smectite/ISML content derived from XRD quantitative analysis showing a slope of 0.64

The cross-plot shows 150 samples of Opalinus Clay and CRZ from all lithological units of the boreholes drilled in the three siting regions (Fig. 1-1) (Nagra 2024b).

The conversion factor, which considers the differences in mineralogy, is given by the equation:

$$CF_{MIN,\,ROCK} = (MIN_{ROCK}/MIN_{IL/SM/ISML}) \times 0.64 \qquad 5\text{-}1$$

where:

MIN_{ROCK} = total clay mineral weight fraction in the rock sample

$MIN_{IL/SM/ISML}$ = 1 (100 % illite/smectite/ISML)

0.64 = the scaling factor between total clay mineral content and the illite/smectite/ISML content

The solid liquid distribution coefficient, $R_{d,\,ROCK}$ required for the rocks can be expressed by:

$$R_{d,\,ROCK} = R_{d,IL/SM/ISML} \times CF_{MIN,ROCK} \qquad 5\text{-}2$$

where:

$R_{d,\,IL/SM/ISML}$ = R_d for pure illite, smectite, ISML as tabulated in Tab. 4-11, and

$CF_{MIN,\,ROCK}$ as defined in Eq. (5-1)

The advantage of this approach is that, in the LUTs, the total clay mineralogy can be varied from 1 to 100 wt.% in steps of 1 wt.%. This is illustrated in the second column of Tab. 5-1 which lists the wt.% of the total clay mineral content of the rock unit. The wt.% of the illite/smectite/ISML contents are scaled using a conversion factor of 0.64 and are shown in the third column of Tab. 5-1. The corresponding $R_{d,ROCK}$ values can be calculated using Eq. (5-2) for the lower, best and upper values as illustrated for Cs and Eu in Tab. 5-1.

Tab. 5-1: Tabulated clay-rock $R_{d,ROCK}$ data between 41 and 60 wt.% total clay mineral content (lower bound, best, upper bound) in $m^3\ kg^{-1}$ for Cs and Eu using the NL-ZNO reference porewater

Element			Cs	Cs	Cs	Eu	Eu	Eu
Unit	wt.%	wt.%	$m^3\ kg^{-1}$	$m^3\ kg^{-1}$	$m^3\ kg^{-1}$	$m^3\ kg^{-1}$	$m^3\ kg^{-1}$	$m^3\ kg^{-1}$
Label	Clay minerals	Illite/ smectite	Rd_low_ Cs	Rd_best_ Cs	Rd_up_ Cs	Rd_low_ Eu	Rd_best_ Eu	Rd_up_ Eu
	41	26.2	8.83E-01	1.41E+00	1.89E+00	1.50E+00	3.21E+00	6.16E+00
	42	26.9	9.05E-01	1.45E+00	1.94E+00	1.54E+00	3.29E+00	6.31E+00
	43	27.5	9.26E-01	1.48E+00	1.98E+00	1.58E+00	3.36E+00	6.47E+00
	44	28.2	9.48E-01	1.51E+00	2.03E+00	1.62E+00	3.44E+00	6.62E+00
	45	28.8	9.69E-01	1.55E+00	2.08E+00	1.65E+00	3.52E+00	6.77E+00
	46	29.4	9.91E-01	1.58E+00	2.12E+00	1.69E+00	3.60E+00	6.92E+00
	47	30.1	1.01E+00	1.62E+00	2.17E+00	1.73E+00	3.68E+00	7.07E+00
	48	30.7	1.03E+00	1.65E+00	2.21E+00	1.76E+00	3.76E+00	7.22E+00
	49	31.4	1.06E+00	1.69E+00	2.26E+00	1.80E+00	3.83E+00	7.37E+00
	50	32.0	1.08E+00	1.72E+00	2.31E+00	1.84E+00	3.91E+00	7.52E+00
	51	32.6	1.10E+00	1.75E+00	2.35E+00	1.87E+00	3.99E+00	7.67E+00
	52	33.3	1.12E+00	1.79E+00	2.40E+00	1.91E+00	4.07E+00	7.82E+00
	53	33.9	1.14E+00	1.82E+00	2.44E+00	1.95E+00	4.15E+00	7.97E+00
	54	34.6	1.16E+00	1.86E+00	2.49E+00	1.98E+00	4.22E+00	8.12E+00
	55	35.2	1.18E+00	1.89E+00	2.54E+00	2.02E+00	4.30E+00	8.27E+00
	56	35.8	1.21E+00	1.93E+00	2.58E+00	2.06E+00	4.38E+00	8.42E+00
	57	36.5	1.23E+00	1.96E+00	2.63E+00	2.09E+00	4.46E+00	8.57E+00
	58	37.1	1.25E+00	2.00E+00	2.67E+00	2.13E+00	4.54E+00	8.72E+00
	59	37.8	1.27E+00	2.03E+00	2.72E+00	2.17E+00	4.62E+00	8.87E+00
	60	38.4	1.29E+00	2.06E+00	2.77E+00	2.20E+00	4.69E+00	9.02E+00

5.1.2 LUTs for the near-field: MX-80 bentonite

Similar as for the far-field, the SDB for MX-80 bentonite is calculated from the sorption data obtained on pure montmorillonite scaled to bentonite by using a mineralogical conversion factor.

The conversion factor for bentonite is given by the equation:

$$CF_{MIN,\ BENT} = (MIN_{BENT}/MIN_{MONT}) \qquad 5\text{-}3$$

where:

$CF_{MIN,\ BENT}$ = mineralogy conversion factor for bentonite

MIN_{BENT} = total montmorillonite weight fraction in bentonite

MIN_{MONT} = 1 (100 % montmorillonite)

Since for the bentonite buffer, the clay mineral component can be considered to solely consist of smectite, the montmorillonite mass fraction for the bentonite was taken to be 70, 80 and 90 wt.%. Note that in the previous SDB (Baeyens et al. 2014), the montmorillonite content was taken to be 75 wt.% and was based on one mineralogical analysis from Müller-von Moos et al. (1983).

The R_d values for the MX-80 bentonite SDB ($R_{d,BENT}$) were calculated from the following equation:

$$R_{d,\,BENT} = R_{d,\,MONT} \times CF_{MIN,\,BENT} \qquad 5\text{-}4$$

The $R_{d,\,MONT}$ values used in Eq. (5-4) are given in Tab. 4-11, and the $CF_{MIN,\,BENT}$ values used to calculate the SDB for bentonite were 0.7, 0.8 and 0.9, respectively. The results for all elements in the reference and high-pCO_2 bentonite porewaters are summarised in Tab. 5-2.

Tab. 5-2: Tabulated bentonite $R_{d,BENT}$ data (best) in $m^3\ kg^{-1}$ for the reference (left) and high-pCO_2 (right) MX-80 bentonite porewaters as derived from Nagra's sorption LUT

Element	**R_d ($m^3\ kg^{-1}$) reference PW**			**R_d ($m^3\ kg^{-1}$) high pCO_2 PW**		
	Montmorillonite wt.%			***Montmorillonite wt.%***		
	70	***80***	***90***	***70***	***80***	***90***
Ac_as_ Am	1.05E+01	1.20E+01	1.35E+01	7.50E+00	8.57E+00	9.65E+00
Am	1.05E+01	1.20E+01	1.35E+01	7.50E+00	8.57E+00	9.65E+00
Ca	1.97E-03	2.25E-03	2.53E-03	2.03E-03	2.33E-03	2.62E-03
Cf_as_Am	1.05E+01	1.20E+01	1.35E+01	7.50E+00	8.57E+00	9.65E+00
Cm_as_Am	1.05E+01	1.20E+01	1.35E+01	7.50E+00	8.57E+00	9.65E+00
Cs	2.46E-02	2.81E-02	3.16E-02	2.53E-02	2.89E-02	3.25E-02
Eu	2.29E+00	2.61E+00	2.94E+00	1.51E+00	1.72E+00	1.94E+00
Fe	8.68E-01	9.93E-01	1.12E+00	4.87E-01	5.57E-01	6.27E-01
Ho_as_Eu	2.29E+00	2.61E+00	2.94E+00	1.51E+00	1.72E+00	1.94E+00
Nb	9.24E+01	1.06E+02	1.19E+02	9.19E+01	1.05E+02	1.18E+02
Ni	1.26E-02	1.44E-02	1.62E-02	9.11E-03	1.04E-02	1.17E-02
Np	4.75E+01	5.43E+01	6.11E+01	2.01E+01	2.29E+01	2.58E+01
Pa	3.60E+01	4.11E+01	4.62E+01	3.60E+01	4.11E+01	4.63E+01
Pb	4.27E-01	4.88E-01	5.49E-01	2.33E-01	2.66E-01	3.00E-01
Pu	1.43E+01	1.63E+01	1.84E+01	7.46E+00	8.52E+00	9.59E+00
Ra	1.82E-02	2.08E-02	2.33E-02	1.83E-02	2.09E-02	2.35E-02
Sm_as_Eu	2.29E+00	2.61E+00	2.94E+00	1.51E+00	1.72E+00	1.94E+00
Sn	9.33E+02	1.07E+03	1.20E+03	1.01E+03	1.16E+03	1.30E+03
Sr	2.06E-03	2.36E-03	2.65E-03	2.13E-03	2.44E-03	2.74E-03
Tc_as_Th	2.47E+01	2.82E+01	3.17E+01	1.18E+01	1.35E+01	1.52E+01
Th	2.47E+01	2.82E+01	3.17E+01	1.18E+01	1.35E+01	1.52E+01
Ti_as_Th	2.47E+01	2.82E+01	3.17E+01	1.18E+01	1.35E+01	1.52E+01
U	4.13E-01	4.73E-01	5.32E-01	1.34E-01	1.53E-01	1.72E-01
Zr_as_Th	2.47E+01	2.82E+01	3.17E+01	1.18E+01	1.35E+01	1.52E+01
Al	2.70E+03	3.09E+03	3.48E+03	2.38E+03	2.72E+03	3.06E+03
Si	3.31E-01	3.78E-01	4.26E-01	3.30E-01	3.78E-01	4.25E-01

The newly established correlations between the clay mineral content and the sorption and diffusion behaviour described in the previous chapters and in Glaus et al. (2024) provide the basis for an innovative approach to calculating continuous profiles of sorption properties along any borehole or stratigraphic column with known mineralogical compositions. Thus, the sorption coefficient LUTs are derived from rocks in Northern Switzerland of varying compositions, i.e. clay mineral contents, and can be systematically combined with the available high-resolution geological data (Nagra 2024c) to generate detailed R_d profiles, which can be statistically evaluated or upscaled to specific output needs. This also reduces uncertainties across the entire dataset.

Consequently, the resulting R_d profiles represent a wealth of data which can be extracted for use in radionuclide transport models for safety assessments. A statistical approach provides the reference, upper and lower bounding values for every abstracted unit. This approach is superior to the approach applied in Nagra's previous SDBs where R_d values for only a few selected units (based mostly on very few samples) were determined and tabulated (Baeyens et al. 2014b).

The new approach, developed for this report, is based on numerous samples and data from Nagra's recent exploratory borehole campaign where thousands of metres of new core material (Fig. 1-1) from the Opalinus Clay and the confining units were recovered (Nagra 2024c, Nagra 2024b). Over 170 rock samples were investigated to determine CEC (Marques Fernandes et al. 2024b) and sorption properties (Marques Fernandes et al. 2024a). The integration of these data with high-resolution mineralogical and petrophysical data (from MultiMin analyses, see Becker & Marnat, 2024) not only enhances their overall detail, but also provides more flexible and comprehensive application options.

5.2 Abstraction of lithostratigraphic units for implementation in performance and safety assessments

The first step in the generation of transport models is to develop a model setup with geological units and data. To achieve this, an abstraction and subsequent simplification of the litho-stratigraphic units determined from boreholes was performed, where the abstracted units have individual representative physical properties of the respective lithostratigraphic units. For this purpose, the detailed and complex Mesozoic lithologies were combined into manageable abstracted units. Details of this first lithostratigraphic abstraction, the unit delineation processes, and the representative geological (Nagra 2024b) and petrophysical (Becker & Marnat 2024) rock properties are considered. Fig. 5-2 gives an overview of the simplification of the lithostratigraphic units into abstracted units.

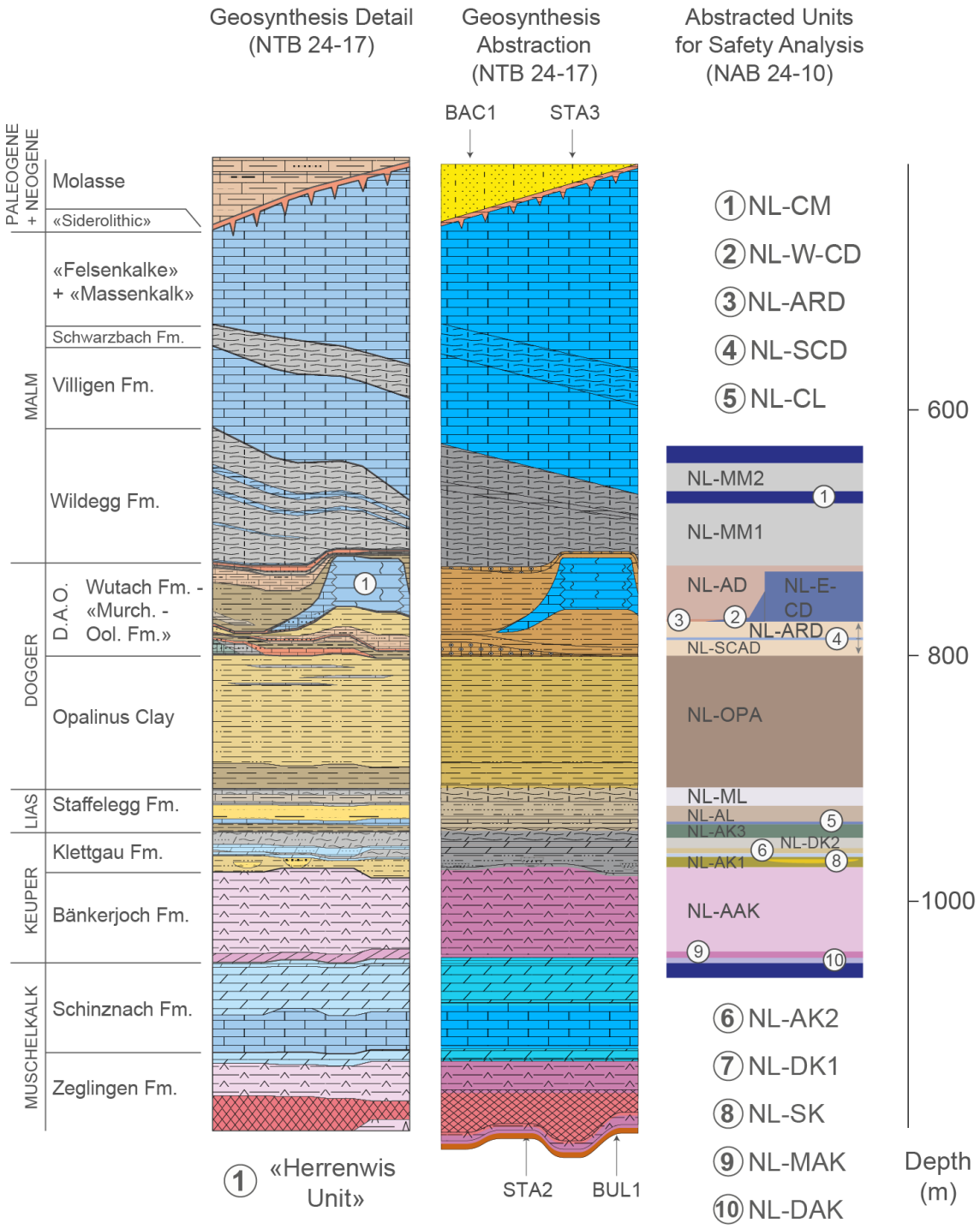

Fig. 5-2: Example of the abstraction of the sedimentary Mesozoic sequence (Nagra 2024b) in the NL siting region into abstracted units (Becker & Marnat 2024) for safety analysis

For the transport models used for performance and safety analyses, several of the thin abstracted units (Fig. 5-2) were further combined for the following reasons:

- The lowermost confining units DAK and MAK (argillaceous Keuper) (Fig. 5-3) overlying the Muschelkalk are thin and have minimal impact on the overall transport of radionuclides compared to AAK (similar in composition) or the other confining units. These two thin units have very similar geological and petrophysical properties. Combining them into a single unit (KAK) simplifies the model without compromising accuracy (individual contributions are negligible).
- The units DK and AK1/SK may contain water-bearing sedimentary subunits in the form of lenses or channels (Fig. 5-3). Combining these units into KAL acknowledges their hydro-geological similarity and encompasses the uncertainties associated with the location of such features within the lithostratigraphic section. This facilitates a coherent representation of possible groundwater flow and transport pathways and allows for conservative model setups and calculations.
- Some units are particularly thin (e.g. CL and DK) and often yielded no laboratory data and only limited MultiMin data. These have been amalgamated despite the different geological properties. In NL, AK2 was combined with DK2 (Fig. 5-3), and in ZNO AK2 was combined with DSK to collectively form the unit KAU. The thin carbonate-rich CL unit (Beggingen Member) together with AK2/3 (JO) or AK3 (NL and ZNO) formed the KEU model unit (Fig. 5-3). From a modelling perspective, this process expands the stratigraphic continuity and ensures a consistent stratigraphic framework across the different regions.
- The units SCAD and SCD (Fig. 5-4) are combined to streamline the modelling process. This simplification reduces complexity (i.e. from the variable number and thickness of the carbonate beds within the argillaceous layers), while still capturing the essential geological and hydrogeological characteristics necessary for accurate modelling and development of robust safety and performance assessments. Details of these highly heterogeneous units across all the siting regions are provided in Nagra (2024b).

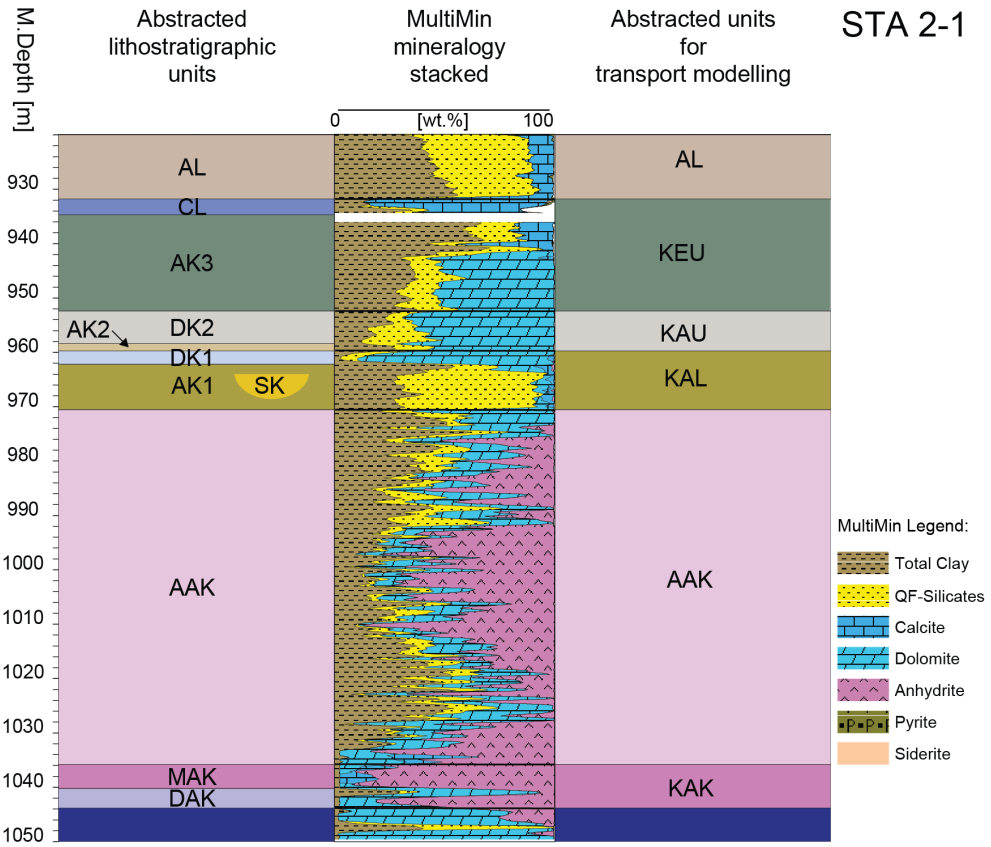

Fig. 5-3: Amalgamation of abstracted lithostratigraphic units below the Opalinus Clay into abstracted modelling units using the example from the Stadel borehole in NL

QF-Silicates is the combined quartz and feldspar content. The middle column (MultiMin) shows the fractional contribution of the minerals on a scale from 0% (left boundary) to 100 wt.% (right boundary).

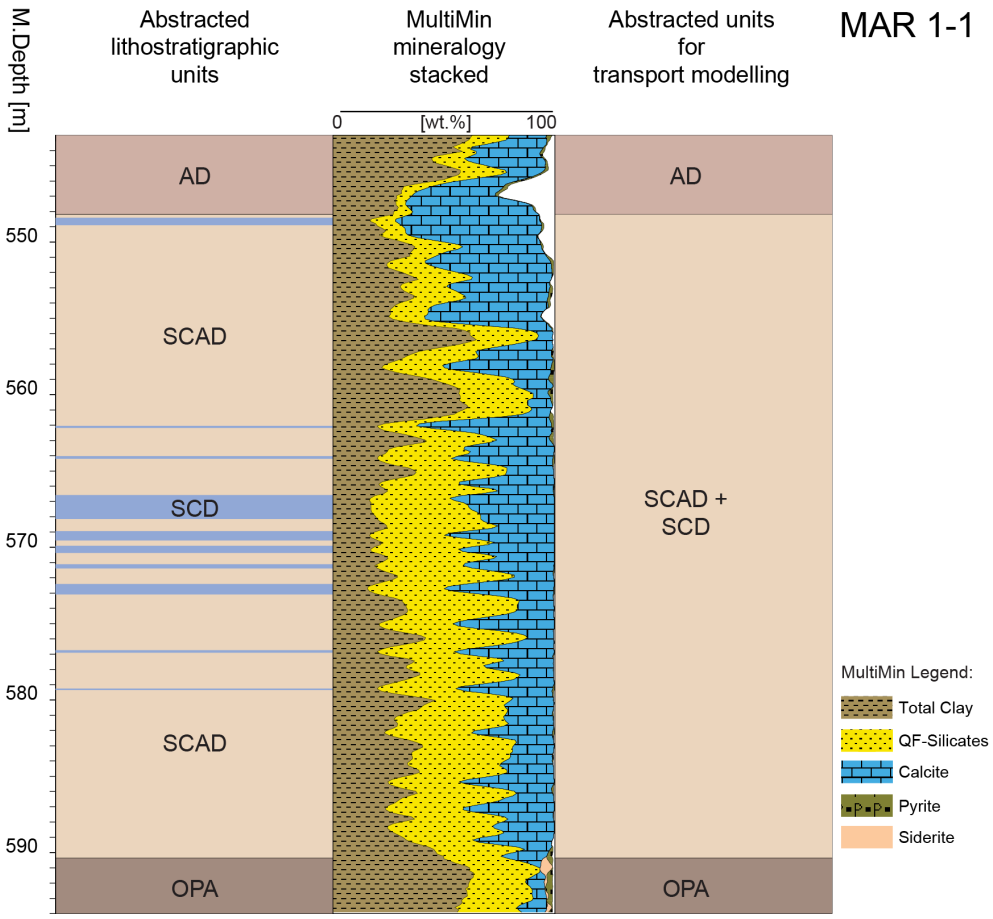

Fig. 5-4: Amalgamation of abstracted lithostratigraphic units above the Opalinus Clay (SCAD and SCD) into abstracted units for transport modelling using the example from the Marthalen borehole in ZNO

QF-Silicates is the combined quartz and feldspar content. The middle column (MultiMin) shows the fractional contribution of the minerals on a scale from 0% (left boundary) to 100 wt.% (right boundary).

In summary, the amalgamation of these units across the siting regions improved the clarity and efficiency of the geological and hydrogeological models used for the radionuclide transport analysis for the performance and safety assessments without losing information. The abstraction ensures that the models are both scientifically sound and practically applicable to the post-closure performance and safety assessments of the repository. Fig. 5-2 to Fig. 5-4 give an overview of the unit abstraction using the example of NL and ZNO.

The resulting high-resolution datasets of each of the aforementioned abstracted units were subsequently analysed to determine representative transport parameter ranges, including best estimate values. This procedure also allowed for detailed numerical and statistical analysis critical for a cohesive model setup for the radionuclide transport modelling and ensured that the most accurate and reliable data are used for subsequent modelling (comparing best estimates with upper and lower boundary values).

5.3 Sorption properties of downhole profiles

All of Nagra's exploratory boreholes in the siting regions have established precise and continuous downhole profiles of total clay mineral content. These were determined by combining petrophysical logs, XRD data from laboratory analyses, and results from a Multi Sensor Core Logger (MSCL). Each high-resolution profile represents an individual stochastic multimineral interpretation on a per-borehole basis (see Becker & Marnat, 2024). This multimineral interpretation method relies on the principle that downhole petrophysical measurement data (from petrophysical logs or core scans) are largely determined by the mineralogy and pore fluid. Therefore, the petrophysical measurement results can be used to determine mineralogy and porosity, amongst other parameters. Conversely, if the mineralogical content, pore fluid and porosity are known, a theoretical petrophysical measurement response can be predicted. By using known mineralogical compositions, porosity values and pore fluid compositions (in this case a slightly saline water) from laboratory analyses, continuous profiles of mineralogical composition and porosity can be predicted. This approach allows the determination of high-resolution total clay mineral content profiles for all boreholes.

For this integration, the total clay mineral content of the MultiMin data was first rounded to full numbers to be compatible with the total clay mineral content values in the LUT. The methodological approach of deriving high-resolution sorption property profiles based on LUTs is illustrated below (Fig. 5-5). For integration with the SDB, the total clay mineral content of the MultiMin data was first rounded to whole numbers to be compatible with the total clay mineral content values in the LUT. Values below 0.5 wt.% were set to 1 wt.%. When rounded correctly, these values would obviously result in a total clay mineral content of 0 wt.%. The method generates a significant number of datapoints which then can undergo robust statistical analyses to identify the bounding values for each abstracted unit. This data processing was implemented in computer scripts (using Python). If any new data become available in the future, the generation of continuous downhole profiles based on the LUTs and clay mineral contents can easily be repeated.

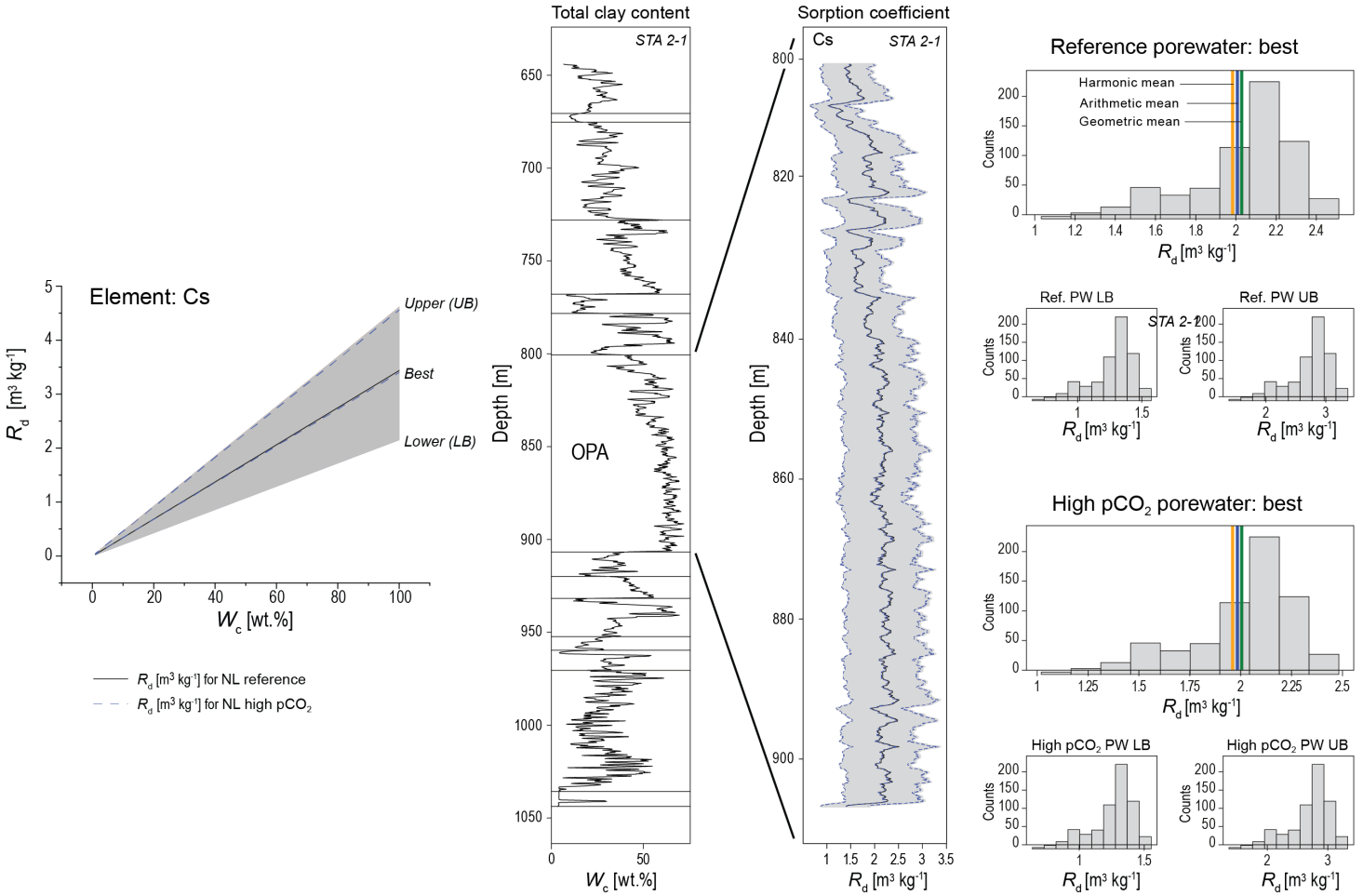

Fig. 5-5: Schematic processes showing how sorption properties are derived based on established total clay mineral content relationships

The LUT diagram (left side) shows the spectrum of the total clay mineral content with corresponding R_d, where best values (solid line) and upper and lower values are given. LUTs and MultiMin total clay mineral content data allow high-resolution R_d profiles to be determined, from which distribution histograms can be obtained and statistical analyses performed. Here, Cs data from borehole STA 2-1 is used as an example.

In Fig. 5-6, the R_d values derived from clay mineral contents are plotted downhole and their correlation with the clay mineral fraction is illustrated. These downhole profiles provide a high-resolution representation of the fluctuating R_d values within and across the geological layering, allowing for precise identification of transport properties at different depths.

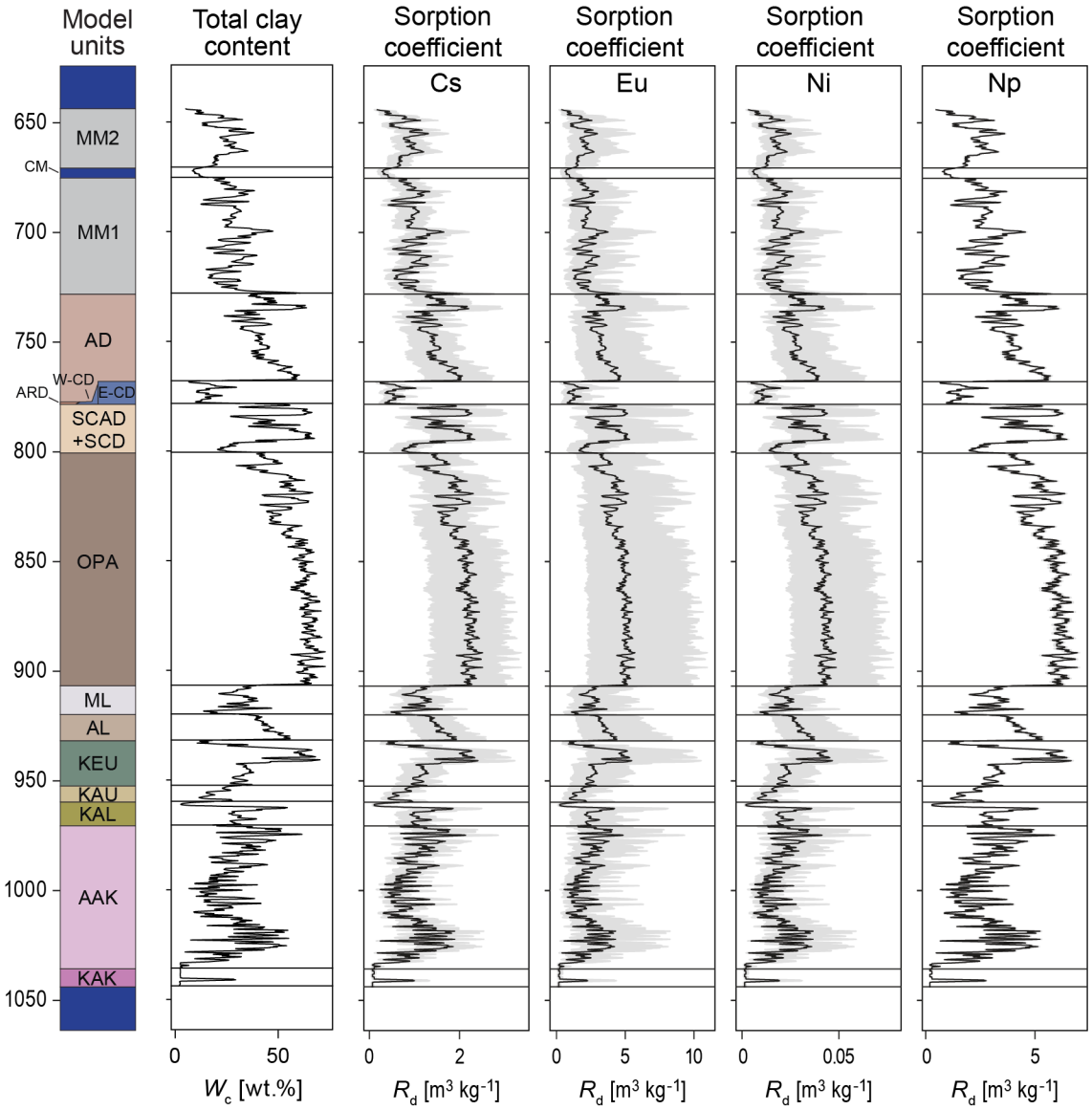

Fig. 5-6: Illustration of selected downhole R_d values for Cs, Eu, Ni and Np

These values were determined from the LUT of the STA 2-1 borehole and using the NL reference porewater. Total clay mineral content and rock density are also indicated. Elements with similar behaviour have comparable profile patterns.

Each abstracted unit has unique patterns of the R_d data in alignment with the identified mineralogical composition. The zigzag curves of the selected elements Cs, Eu, Ni and Np in the borehole profile of Stadel 2-1 serve as a visual indication of these variations, illustrating the rock compositional heterogeneity throughout the entire profile (from the basal Muschelkalk to the Malm at the top), as well as the occasional variability within geological units (e.g. AD). This detailed illustration helps to enhance the understanding of the unit-specific composition and how the sorption behaviour is influenced by the clay mineralogical composition. This, therefore, provides support for the development of more accurate predictive models for radionuclide transport behaviour at a high-resolution scale.

In Fig. 5-7, the R_d values for Cs derived from total clay mineral contents across four stratigraphic units (SCAD+SCD, Opalinus Clay, argillaceous Lias (AL) and marly Lias (ML)) provide an example of their relationship with the total clay mineral fraction of each unit. Note that the scale differs across all units due to their varying thicknesses. Like the figure above, the selected unit profiles exhibit distinctive zigzag curves, reflecting variations in total clay mineral content and thus rock properties. The blue line represents the data of the high-pCO_2 porewater and illustrates minimal deviations from the data of the reference porewater.

The high-resolution representation of the upper and lower bounding values, as well as the reference values, illustrates the overall variability of the R_d that can be determined based on the method of the LUTs. This detailed depiction helps visually with understanding the variability of sorption across each unit.

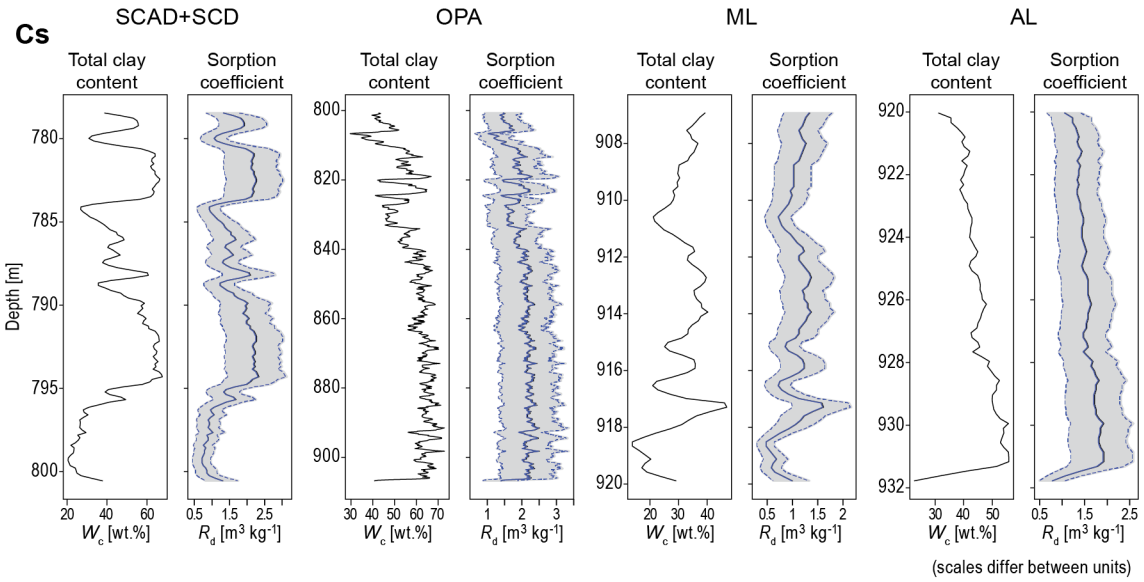

Fig. 5-7: Examples of R_d downhole plots of four selected units (SCAD+SCD, Opalinus Clay, ML and AL) derived from total clay mineral contents

The figures show values for both reference (dark grey) and high-pCO_2 (blue lines) values, indicating that the sorption behaviour shows little difference between these porewater compositions.

5.4 Statistical analysis of sorption data

The compilation of all data for the individual abstracted units also allows for a statistical investigation of the parameter distribution and spread or range of values (Fig. 5-8). Plotted as histograms, the R_d values for Cs and Eu have been illustrated (Fig. 5-8), showing their distribution across the four selected model units (SCD+SCAD, OPA, ML, AL). For example, the data distribution for Cs within the Opalinus Clay shows that most of R_d values range between 1.25 m^3 kg^{-1} and 2.4 m^3 kg^{-1}. The HM of R_d_best_Cs column is 1.93 m^3 kg^{-1}. The data distribution shows a unimodal pattern, and the spread of data is relatively narrow.

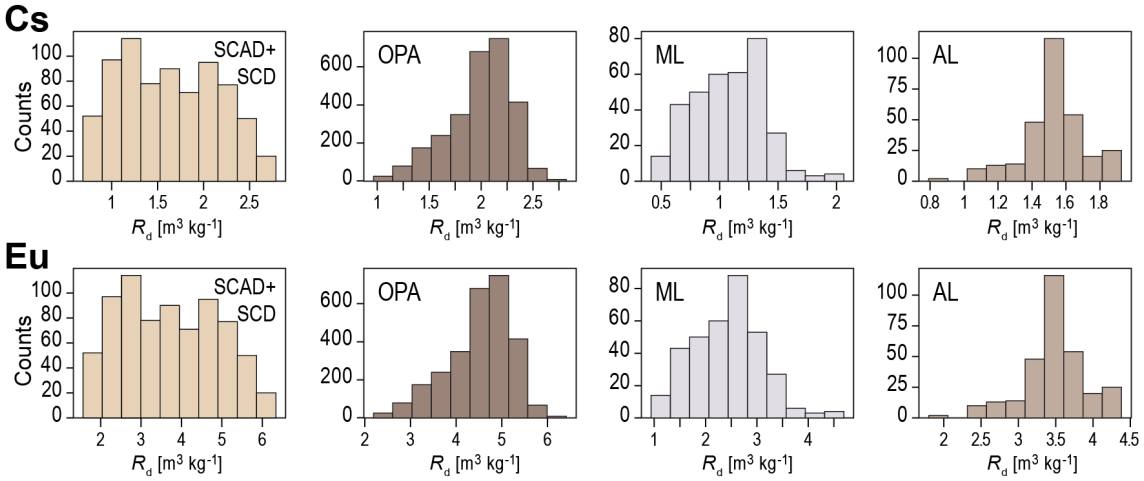

Fig. 5-8: Histograms of the harmonic mean of R_d data from all boreholes in the NL siting region

The histograms show data characteristics for each unit (i.e. reflecting compositional variabilities).

Following statistical analysis of the radionuclide sorption data for each abstracted unit in each borehole of the three siting regions, different datasets can be produced depending on the context of use. This implies that the data spread of the systematic statistical analysis can be displayed depending on the purpose of the data, including the:

- Harmonic mean (HM) (used for radionuclide transport modelling for safety assessments) (Nagra 2024d);
- Geometric mean (GM) (used for transport modelling in 3D models of the performance assessment) (Nagra 2024e); and
- Arithmetic mean (AM) and P50 values for each abstracted unit.

For all these means, details of reference and deviatory values for each radionuclide (i.e. upper and lower boundaries) can be displayed and determined. The subsequent applications of these robust datasets of the abstracted units within the different transport models are the basis of performance and safety assessment (e.g. Tab. 5-3).

In general, a quality check of these detailed characterisations and the different types of means, of transport parameters need to consider the following:

1) the variability of rock composition (wide or narrow);
2) the number of data points; and
3) data comparison with samples analysed in the laboratory (comparison of LUT data and laboratory data).

Tab. 5-3: Tabulated HM best values of R_d values for NL for selected abstracted units, calculated based on the LUTs

The values represent the mean value of all samples of each abstracted unit for NL. Here the data show the R_d data for all elements considered (in m^3 kg^1) for the modelling units SCD+SCAD, Opalinus Clay, ML and AL of NL for the reference porewater chemistry at 25 ºC.

Element	**R_d (m^3 kg^{-1}) reference porewater**											
	SCAD+SCD			**Opalinus Clay**			**ML**			**AL**		
	LB	Best	UB	LB	Best	UB	LB	Best	UB	LB	Best	UB
Ac as Am	4.93E-02	2.10E+00	1.38E+01	6.51E-02	2.77E+00	1.82E+01	3.31E-02	1.41E+00	9.25E+00	5.09E-02	2.17E+00	1.42E+01
Am	4.93E-02	2.10E+00	1.38E+01	6.51E-02	2.77E+00	1.82E+01	3.31E-02	1.41E+00	9.25E+00	5.09E-02	2.17E+00	1.42E+01
Ca	na	3.21E-04	na	na	4.24E-04	na	na	2.16E-04	na	na	3.32E-04	na
Cf as Am	4.93E-02	2.10E+00	1.38E+01	6.51E-02	2.77E+00	1.82E+01	3.31E-02	1.41E+00	9.25E+00	5.09E-02	2.17E+00	1.42E+01
Cm as AM	4.93E-02	2.10E+00	1.38E+01	6.51E-02	2.77E+00	1.82E+01	3.31E-02	1.41E+00	9.25E+00	5.09E-02	2.17E+00	1.42E+01
Cs	9.14E-01	1.46E+00	1.96E+00	1.21E+00	1.93E+00	2.58E+00	6.13E-01	9.80E-01	1.31E+00	9.44E-01	1.51E+00	2.02E+00
Eu	1.56E+00	3.32E+00	6.38E+00	2.06E+00	4.38E+00	8.42E+00	1.05E+00	2.23E+00	4.28E+00	1.61E+00	3.43E+00	6.59E+00
Fe	na	7.57E-02	na	na	9.99E-02	na	na	5.08E-02	na	na	7.82E-02	na
Ho as Eu	1.56E+00	3.32E+00	6.38E+00	2.06E+00	4.38E+00	8.42E+00	1.05E+00	2.23E+00	4.28E+00	1.61E+00	3.43E+00	6.59E+00
Nb	1.53E+00	1.18E+01	6.00E+01	2.02E+00	1.56E+01	7.92E+01	1.03E+00	7.92E+00	4.03E+01	1.58E+00	1.22E+01	6.20E+01
Ni	1.72E-02	2.83E-02	4.54E-02	2.27E-02	3.73E-02	5.99E-02	1.16E-02	1.90E-02	3.05E-02	1.78E-02	2.92E-02	4.69E-02
Np	3.96E+00	4.04E+00	4.10E+00	5.22E+00	5.33E+00	5.41E+00	2.65E+00	2.71E+00	2.75E+00	4.09E+00	4.17E+00	4.23E+00
Pa	1.07E+01	1.97E+01	3.61E+01	1.41E+01	2.60E+01	4.76E+01	7.17E+00	1.32E+01	2.42E+01	1.10E+01	2.03E+01	3.73E+01

Tab. 5-3: Cont.

Element	R_d (m^3 kg^{-1}) reference porewater											
	SCAD+SCD			Opalinus Clay			ML			AL		
	LB	Best	UB	LB	Best	UB	LB	Best	UB	LB	Best	UB
Pb	6.45E-01	2.27E+00	7.56E+00	8.51E-01	2.99E+00	9.97E+00	4.33E-01	1.52E+00	5.07E+00	6.66E-01	2.34E+00	7.80E+00
Pu	na	5.84E+00	na	na	7.71E+00	na	na	3.92E+00	na	na	6.04E+00	na
Ra	1.22E-01	2.06E-01	3.48E-01	1.61E-01	2.72E-01	4.60E-01	8.20E-02	1.38E-01	2.34E-01	1.26E-01	2.13E-01	3.60E-01
Sn as Eu	1.56E+00	3.32E+00	6.38E+00	2.06E+00	4.38E+00	8.42E+00	1.05E+00	2.23E+00	4.28E+00	1.61E+00	3.43E+00	6.59E+00
Sn	2.92E+01	8.75E+01	2.35E+02	3.86E+01	1.15E+02	3.10E+02	1.96E+01	5.87E+01	1.57E+02	3.02E+01	9.03E+01	2.42E+02
Sr	na	3.20E-04	na	na	4.22E-04	na	na	2.15E-04	na	na	3.31E-04	na
Tc as Th	6.40E-01	1.79E+01	7.28E+01	8.45E-01	2.36E+01	9.60E+01	4.30E-01	1.20E+01	4.88E+01	6.61E-01	1.85E+01	7.51E+01
Th	6.40E-01	1.79E+01	7.28E+01	8.45E-01	2.36E+01	9.60E+01	4.30E-01	1.20E+01	4.88E+01	6.61E-01	1.85E+01	7.51E+01
Ti as Th	6.40E-01	1.79E+01	7.28E+01	8.45E-01	2.36E+01	9.60E+01	4.30E-01	1.20E+01	4.88E+01	6.61E-01	1.85E+01	7.51E+01
U	1.75E-02	1.80E-02	1.85E-02	2.31E-02	2.38E-02	2.44E-02	1.18E-02	1.21E-02	1.24E-02	1.81E-02	1.86E-02	1.91E-02
Zr as Th	6.40E-01	1.79E+01	7.28E+01	8.45E-01	2.36E+01	9.60E+01	4.30E-01	1.20E+01	4.88E+01	6.61E-01	1.85E+01	7.51E+01
Al	na	8.38E+02	na	na	1.11E+03	na	na	5.62E+02	na	na	8.65E+02	na
Si	na	1.26E-01	na	na	1.67E-01	na	na	8.47E-02	na	na	1.30E-01	na

The statistical data can also be visually displayed for ease of comparison of ranges or means. In the figure below, a few selected elements and their sorption data are illustrated as box and whisker (box) plots. These plots easily summarise the data and outline the data range, inform about the skewness (box) and provide a cross-unit comparison. For example, the dotted lines provide the HM values of the Opalinus Clay.

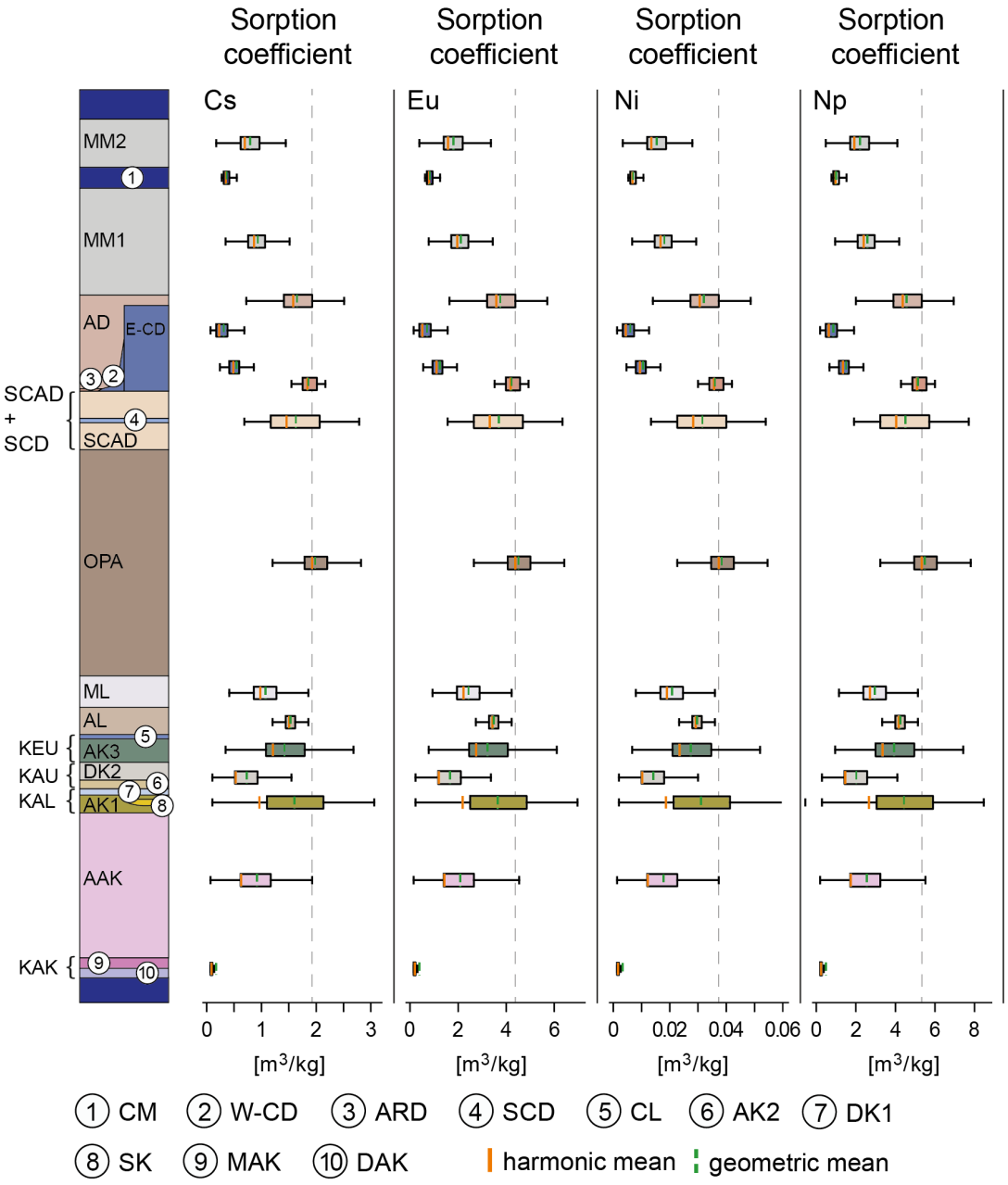

Fig. 5-9: Box plots showing the R_d distribution of selected elements across the abstracted units of NL

Grey dotted line indicates the harmonic mean value of Opalinus Clay. Box- and -whisker plots are informative tools to visually summarise the data, including the illustration of the data median, the quartiles and the potential outliers (whiskers). The shape of the box and the length of the whiskers indicates the skewness. Additional means (harmonic and geometric) are also included.

Similarly, following the methodology used to determine sorption data for the abstracted units, additional parameters such as clay mineral content, porosity and grain density were computed and compiled. An example of the table with the mean data for NL is provided in Tab. 5-4.

Tab. 5-4: Harmonic mean (HM), geometric mean (GM), arithmetic mean (AM) data of total clay mineral content, MultiMin porosity and grain density of all borehole data for NL

Unit	**Total clay mineral content** [wt.%]			**Porosity** [-]			**Grain density** [g cm^{-3}]		
	HM	**GM**	**AM**	**HM**	**GM**	**AM**	**HM**	**GM**	**AM**
MM2	20.2	21.7	23.1	0.06	0.06	0.07	2.70	2.70	2.70
CM	10.2	10.4	10.5	0.03	0.03	0.03	2.71	2.71	2.71
MM1	25.1	26.1	27.1	0.07	0.07	0.07	2.71	2.71	2.71
AD	45.9	47.0	48.0	0.12	0.12	0.12	2.73	2.73	2.73
E-CD	6.7	7.7	9.1	0.02	0.03	0.03	2.71	2.71	2.71
W-CD	14.1	14.9	15.8	0.04	0.04	0.04	2.71	2.71	2.71
ARD	53.6	53.8	54.0	0.13	0.13	0.13	2.74	2.74	2.74
SCD	20.0	20.0	20.0	0.06	0.06	0.06	2.72	2.72	2.72
SAD	42.5	44.9	47.4	0.11	0.12	0.12	2.73	2.73	2.73
SCAD+SCD	42.4	44.9	47.3	0.11	0.12	0.12	2.73	2.73	2.73
OPA	56.0	56.9	57.6	0.11	0.11	0.11	2.70	2.70	2.70
ML	28.5	29.9	31.1	0.07	0.08	0.08	2.66	2.66	2.66
AL	43.8	44.2	44.6	0.08	0.08	0.08	2.68	2.68	2.68
CL	21.7	24.4	27.7	0.05	0.06	0.07	2.79	2.79	2.79
AK3	39.3	41.3	43.6	0.11	0.12	0.12	2.76	2.76	2.76
KEU	35.2	38.2	41.3	0.10	0.11	0.11	2.76	2.76	2.77
DK2	13.3	16.1	18.1	0.07	0.08	0.08	2.80	2.80	2.80
AK2	22.9	25.4	27.7	0.10	0.10	0.11	2.79	2.79	2.79
KAU	15.4	18.7	21.2	0.08	0.08	0.09	2.80	2.80	2.80
DK1	8.0	10.5	13.7	0.06	0.07	0.08	2.81	2.81	2.81
SK	34.2	35.0	35.7	0.14	0.14	0.14	2.67	2.67	2.67
AK1	54.2	56.2	57.8	0.13	0.13	0.14	2.71	2.71	2.71
KAL	27.8	39.8	46.6	0.11	0.12	0.13	2.71	2.72	2.72
AAK	18.5	23.5	26.7	0.07	0.08	0.09	2.79	2.79	2.79
MAK	2.5	2.5	2.5	0.01	0.01	0.01	2.92	2.92	2.92
KAK	2.8	3.4	5.2	0.01	0.02	0.02	2.90	2.90	2.90
DAK	3.5	5.1	8.5	0.02	0.02	0.03	2.87	2.87	2.87

6 Uncertainties

The R_d values are calculated for elements where ClaySor model parameters are available (see Section 4.2 and 4.3) in the LUTs together with the upper and lower bounds of the 95% confidence interval of the model prediction. This confidence interval is based on the element-specific ClaySor model parameter uncertainties determined in the STDB 2023 from the fitting procedure (Marinich et al. 2024). This was evaluated using a global uncertainty propagation method implemented in the UpsaGEMS code (PSI/LES Progress Report 2021) and used in the JupyterLab notebook (https://jupyter.org/) to produce the SDB R_d LUT. The script uses the xGEMS code via its Python API to perform chemical equilibrium calculations and retrieve the R_d values, while the Uncertainpy Python library (Tennøe et al. 2018) is used for the statistical analysis to produce the confidence interval of the calculated R_d values.

The STDB 2023 for the ClaySor model was re-parametrised and the uncertainties of the apparent standard molar Gibbs energy (in its standard state at reference temperature of 25 °C, i.e. 298 K, and pressure of 1 bar) of SC and CE species, $G°_{298}$, were systematically evaluated from the experimental data (Marinich et al. 2024). Using the Monte Carlo sampling method (Miron et al. 2015, Motulsky & Christopoulos 2004), 1000 synthetic datasets of measurements were generated for each investigated element-clay mineral pair, and model parameters were refitted. For each case, the uncertainties of the $G°_{298}$ values were obtained by multiplying the standard deviation of the 1000 parameter values by 1.96, corresponding to the 95% confidence level, assuming a normal distribution. It should be noted that the derived uncertainty at the 95% confidence level is linked both to the model parameters and to how well the model is determined by the measured points.

The $G°_{298}$ values of species and their uncertainties from the ClaSor model were used in the calculation of the *in-situ* R_d values and 95% confidence interval. For given input conditions of the calculation, set by the porewater compositions, only some sorption species have a contribution of >1% in the predicted R_d values. For each of these parameters, the Uncertainpy script (Tennøe et al. 2018) samples many values for different parameter combinations and, through GEMS calculations, for each combination a spread of calculated *in-situ* R_d values is generated. The upper and lower R_d values in the LUTs are taken as the upper and lower bounds of the 95% confidence interval of these predicted *in-situ* R_d values.

The error propagation method does not account for parameter correlation. As a result, the 95% confidence interval will be wider for R_d values calculated from the contribution of two or more surface species that are highly correlated. The predicted *in-situ* R_d values can be treated as the average model-predicted sorption values for the given *in-situ* porewater compositions. Note that the confidence interval does not provide the probability of containing a measured value or future observations, which is instead indicated by a prediction interval (Hyndman 2013), rather it provides the likelihood that it contains the model-predicted R_d values if the model was refitted with additional measurements obtained using the exact same setup.

Upper and lower R_d values were not estimated for elements whose sorption parameters or $G°_{298}$ values were either not estimated or lacked uncertainty estimates (Marinich et al. 2024). These elements are: Al, C, Ca, Cr, Si and Sr, for both illite and montmorillonite and Cd, Fe for illite. An exception applies to elements whose R_d values, including upper and lower boundaries, were assumed to be identical to those of their corresponding chemical analogues (see Section 4.4).

Uncertainties due to variabilities of the porewater composition as well as the errors in the thermodynamic properties of the sorption of reducing aqueous complexes were not systematically accounted for in this work. The changes in R_d values that are due to the variability of the porewaters are within the model uncertainties (Fig. 4-2 and Fig. 4-3). The 2:1 clay mineral wt.% has the largest effect on the calculated R_d values, making it the dominant parameter. As such, the greatest uncertainties arise from the clay mineralogy of the rock samples.

7 Conclusions

The safety assessment of deep geological repositories relies on values for the retention and transport properties of safety-relevant elements under site-specific geochemical conditions. Sorption of radionuclides on mineral surfaces of the Opalinus Clay (and the confining geological rock units) is one of the most important retention processes.

This report describes the development of sorption databases with element-specific R_d values for JO, NL, ZNO and MX-80 bentonite and the respective porewater types. Furthermore, the generation of look-up tables with R_d values calculated for varying clay mineral content has been detailed, along with their utility for the generation of high-resolution borehole sorption profiles. The production of statistical distributions for the abstracted lithostratigraphic units has also been demonstrated.

The sorption distributions in the SDBs were calculated based on the simplified CA approach, assuming that montmorillonite for bentonite, and illite, smectite and ISML for the Opalinus Clay and the confining units are the dominant sorbing minerals. The approach was verified for a wide range of key radionuclides using blind predictions of experimentally determined sorption isotherms of rock samples taken from drill cores from the three siting regions in their corresponding synthetic porewaters. Calculations were performed with GEMS, both for SDBs and blind predictions, using a consistent chemical system based on the state-of-the-art PSI/Nagra TDB 2020, and the updated ClaySor (2SPNE CE/SC + GCS) thermodynamic sorption model for illite and montmorillonite. Calculations also accounted for redox-sensitive elements and their reactions in the defined porewater conditions and included competition between bivalent cations for planer sites (CE) and edge sites (SC). The inputs to the calculations were the site capacities and the porewaters from the different siting regions. For elements with existing thermodynamic sorption models, R_d values were calculated for the site-specific porewater conditions together with the upper and lower bound of the 95% confidence interval derived from the model parameter uncertainties. The resulting R_d values were then used to produce the look-up tables for ranges of illite/smectite/ISML wt.% content.

Compared to previous sorption databases, the calculated sorption coefficients for bentonite and Opalinus Clay are, in most cases lower, although within the model uncertainty for most elements. Differences exist mainly for elements that form predominantly zerovalent aqueous species or divalent cations subject to SC competition.

The porewater composition is overwhelmingly controlled by a rock buffered system, with the mineral assemblage fixing the redox conditions, pH and chemical composition. Changes in the calculated R_d values due to variations in the porewater of the different siting regions are well within the 95% confidence interval of the model. For the clay mineral-poor sedimentary rocks, the calculated values are conservative as retention mechanisms related to other minerals are not considered. Therefore, the dominant control on the sorption capacity of the Opalinus Clay and the confining units is the content of illite/smectite/ISML, outweighing other potential variabilities due to changes in the porewater composition between lithostratigraphic units. The variability of the illite/smectite/ISML content is accounted for in statistical analysis of the sorption data when producing the statistical distributions for the abstracted lithostratigraphic units used in performance and safety assessment.

The newly established correlations between the illite/smectite/ISML content and the sorption properties provide the basis for the novel approach used to calculate continuous profiles of sorption properties along any borehole or stratigraphic column with known mineralogical compositions. As these sorption coefficient look-up tables are derived from rocks in Northern Switzerland with varying mineralogical compositions, i.e. illite/smectite/ISML contents, they can be systematically combined with the available high-resolution geological data. This approach transforms downhole mineralogical data into detailed downhole data plots for sorption coefficients, effective diffusion coefficients, and accessible porosity, which can then be statistically evaluated or upscaled to specific output needs, thus reducing uncertainties across the entire dataset. Consequently, the resulting detailed sorption coefficient profiles contain data which are then extracted using a statistical approach to provide reference, upper and lower bounding values for every abstracted unit identified for the assessment models.

8 References

Allard, B., Karlsson, M., Tullborg, E.L. & Larsson, S.A. (1983): Ion exchange capacities and surface areas of some major components and common fracture filling materials of igneous rocks. KBS/TR 83-64. KBS, Stockholm.

Baeyens, B. & Bradbury, M.H. (1997): A mechanistic description of Ni and Zn sorption on Na-montmorillonite Part I: Titration and sorption measurements. Journal of Contaminant Hydrology 27/3-4, 199-222. DOI: 10.1016/S0169-7722(97)00008-9.

Baeyens, B. & Bradbury, M.H. (2017): The development of a thermodynamic sorption data base for montmorillonite and the application to bentonite. Nagra Technical Report NTB 17-13.

Baeyens, B. & Marques Fernandes, M. (2018): Adsorption of heavy metals including radionuclides. Chapter 5. Developments in Clay Science 9, 125-172. DOI: 10.1016/B978-0-08-102432-4.00005-6.

Baeyens, B., Marques Fernandes, M. & Bradbury, M.H. (2014a): Comparison of sorption measurements on argillaceous rocks and bentonite with predictions using the SGT-E2 approach to derive sorption data bases. Nagra Technical Report NTB 12-05.

Baeyens, B., Thoenen, T., Bradbury, M.H. & Marques Fernandes, M. (2014b): Sorption data bases for argillaceous rocks and bentonite for the provisional safety analyses for SGT-E2. Nagra Technical Report NTB 12-04.

Becker, J. & Marnat, S. (2024): Petrophysical Data and Core-Calibrated Multimineral Interpretation. Nagra Arbeitsbericht NAB 24-17.

BFE (2008): Sachplan Geologische Tiefenlager: Konzeptteil. BFE 2. April 2008 (Revision vom 30. November 2011). Departement für Umwelt, Verkehr, Energie und Kommunikation UVEK, Bern.

Bradbury, M.H. & Baeyens, B. (1997): A mechanistic description of Ni and Zn sorption on Na-montmorillonite Part II: Modelling. Journal of Contaminant Hydrology 27, 223-248. DOI: 10.1016/S0169-7722(97)00007-7

Bradbury, M.H. & Baeyens, B. (1998): N2-BET surface area measurements on crushed and intact minerals and rocks: A proposal for estimating sorption transfer factors. Nuclear Technology 122/2, 250-253. DOI: 10.13182/NT98-A2866.

Bradbury, M.H. & Baeyens, B. (2000): A generalised sorption model for the concentration dependent uptake of caesium by argillaceous rocks. Journal of Contaminant Hydrology 42/2-4, 141-163. DOI: 10.1016/S0169-7722(99)00094-7.

Bradbury, M.H. & Baeyens, B. (2009a): Sorption modelling on illite Part I: Titration measurements and the sorption of Ni, Co, Eu and Sn. Geochimica et Cosmochimica Acta 73/4, 990-1003. DOI: 10.1016/j.gca.2008.11.017.

Bradbury, M.H. & Baeyens, B. (2009b): Sorption modelling on illite. Part II: Actinide sorption and linear free energy relationships. Geochimica et Cosmochimica Acta 73/4, 1004-1013. DOI: 10.1016/J.GCA.2008.11.016.

Bradbury, M.H. & Baeyens, B. (2011): Predictive sorption modelling of Ni(II), Co(II), Eu(IIII), Th(IV) and U(VI) on MX-80 bentonite and Opalinus Clay: A “bottom-up” approach. Applied Clay Science 52/1-2, 27-33. DOI: 10.1016/J.CLAY.2011.01.022.

Bradbury, M.H. & Baeyens, B. (2017): The development of a thermodynamic sorption data base for illite and the application to argilaceous rocks. Nagra Technical Report NTB 17-14.

Brandt, F., Klinkenberg, M., Poonoosamy, J. & Bosbach, D. (2020): Recrystallization and uptake of ^{226}Ra into Ba-rich (Ba,Sr)SO_4 solid solutions. Minerals 10/9, 812. DOI: 10.3390/ min10090812.

Cowan, C.E., Zachara, J.M. & Resch, C.T. (1990): Solution ion effects on the surface exchange of selenite on calcite. Geochimica et Cosmochimica Acta 54/8, 2223-2234. DOI: 10.1016/ 0016-7037(90)90047-O.

Curti, E. (2023): Bentonite pore waters (BPW) for SGT-E3: Model development, testing and final calculations. Nagra Arbeitsbericht NAB 22-43.

Davis, J.A., Fuller, C.C. & Cook, A.D. (1987): A model for trace metal sorption processes at the calcite surface: Adsorption of Cd2+ and subsequent solid solution formation. Geochimica et Cosmochimica Acta 51/6, 1477-1490. DOI: 10.1016/0016-7037(87)90330-9.

Gamsjäger, H., Bugajski, J., Gajda, T., Lemire, R. & Preis, W. (2005): Chemical Thermodynamics of Nickel. (Chemical Thermodynamics, 6). Elsevier, Amsterdam.

Giffaut, E., Grivé, M., Blanc, P., Vieillard, P., Colàs, E., Gailhanou, H., Gaboreau, S., Marty, N., Madé, B. & Duro, L. (2014): Andra thermodynamic database for performance assessment: ThermoChimie. Applied Geochemistry 49, 225-236. DOI: 10.1016/ J.APGEOCHEM.2014.05.007.

Glaus, M.A., Kulik, D.A., Miron, G.D., van Loon, L.R., Wüst, R.A.J., Becker, J.K. & Li, X. (2024): Diffusion Databases for Opalinus Clay, Confining Geological Units and Bentonite: Methods, Concepts and Upscaling of Data. Nagra Technical Report NTB 23-08.

Grenthe, I., Fuger, J., Konings, R., Lemire, R.J., Muller, A.B., Nguyen-Trung C. & Wanner, H. (1992): Chemical Thermodynamics of Uranium. (Chemical Thermodynamics, 1). North-Holland, Amsterdam.

Guillaumont, R., Fanghänel, T., Fuger, J., Grenthe, I., Neck, V., Palmer, D.A. & Rand, M. (2003): Update of the Chemical Thermodynamics of Uranium, Neptunium, Plutonium, Americium and Technetium. (Chemical Thermodynamics, 5). Elsevier, Amsterdam.

Hummel, W., Berner, U., Curti, E., Pearson, F.J. & Thoenen, T. (2002): Nagra/PSI Chemical Thermodynamic Data Base 01/01. Radiochimica Acta 90, 805-813. DOI: 10.1524/ract.2002.90.9-11_2002.805.

Hummel, W., Kulik, D.A. & Miron, G.D. (2022): Solubility of radionuclides and influence of EDTA for use in the development of the cement sorption database (SDB 2022). Nagra Arbeitsbericht NAB 22-38.

Hummel, W., Kulik, D.A. & Miron, G.D. (2023): Solubility limits for bentonite near field (update of NTB 14-06). Nagra Technical Report NTB 23-04.

Hummel, W. & Thoenen, T. (2023): The PSI Chemical Thermodynamic Database 2020. Nagra Technical Report NTB 21-03.

Hyndman, R.J. (2013): The difference between prediction intervals and confidence intervals. WWW Dokument, available online at URL https://robjhyndman.com/hyndsight/intervals/, status as of September 20, 2024.

KEG (2003): Kernenergiegesetz (KEG) of March 21, 2003, status as of January 1, 2024. Systematische Sammlung des Bundesrechts SR 732.1, Schweiz.

KEV (2004): Kernenergieverordnung (KEV) of December 10, 2004, status as of January 1, 2024. Systematische Sammlung des Bundesrechts SR 732.11, Schweiz.

Kiczka, M., Wersin, P., Mazurek, M., Zwahlen, C., Jenni, A., Mäder, U. & Traber, D. (2023): Porewater composition in clay rocks explored by advective displacement and squeezing experiments. Applied Geochemistry 159, 105838. DOI: 10.1016/ j.apgeochem.2023.105838.

Kulik, D.A., Fernandes, M.M. & Baeyens, B. (2018): The 2SPNE SC/CE sorption model in GEM-Selektor v.3.4 code package (ClaySor): Implementation, tests, and user guide. Nagra Arbeitsbericht NAB 18-27.

Kulik, D.A. & Miron, G.D. (2024): Solubility limits for model Opalinus Clay porewaters as input for sorption (SDB) and diffusion (DDB) databases. Nagra Arbeitsbericht NAB 23-07.

Kulik, D.A., Wagner, T., Dmytrieva, V.S., Kosakowski, G., Hingerl, F.F., Chudnenko, V.K. & Berner, U.R. (2013): GEM-Selektor geochemical modeling package: Revised algorithm and GEMS3K numerical kernel for coupled simulation codes. Computational Geosciences 17/1, 1-24. DOI: 10.1007/s10596-012-9310-6.

Lemire, R.J., Fuger, J., Nitsche, H., Potter, P., Rand, M.H., Rydberg, J., Spahiu, K., Sullivan, J.C., Ullman, W.J., Vitorge, P. & Wanner, H. (2001): Chemical Thermodynamics of Neptunium and Plutonium. (Chemical Thermodynamics, 4). Elsevier, Amsterdam.

Leupin, O.X., van Loon, L.R., Gimmi, T., Wersin, P. & Soler, J.M. (2017): Exploring diffusion and sorption processes at the Mont Terri rock laboratory (Switzerland): lessons learned from 20 years of field research. Swiss Journal of Geosciences 110/1, 391-403. DOI: 10.1007/s00015-016-0254-z.

Mäder, U. & Wersin, P. (2023): Reference porewaters for SGT Stage 3 of the Opalinus Clay for the siting regions Jura Ost (JO), Nördlich Lägern (NL) and Zürich Nordost (ZNO). Nagra Arbeitsbericht NAB 22-47.

Marinich, O., Marques Fernandes, M., Miron, G.D. & Kulik, D.A. (2024): ClaySor 2023: Update of 2SPNE SC/CE Sorption Model for Illite and Montmorillonite in GEMS Implementation. Nagra Technical Report NTB 23-05.

Marques, F.M. & Baeyens, B. (2019): Cation exchange and surface complexation of lead on montmorillonite and illite including competitive adsorption effects. Applied Geochemistry 100, 190-202.

Marques Fernandes, M. & Baeyens, B. (2020): Competitive adsorption on illite and montmorillonite: Experimental and modelling investigations. Nagra Technical Report NTB 19-05.

Marques Fernandes, M. & Baeyens, B. (2021): Application of the bottom-up approach for the sorption of Cs(I), Co(II), Ni(II), Eu(III), Th(IV) and U(VI) onto sedimentary rocks. Nagra Technical Report NTB 19-04.

Marques Fernandes, M., Marinich, O., Miron, G.D. & Baeyens, B. (2024a): Sorption of Cs, Ni, Eu, Th and U on Drill Core Samples of Opalinus Clay and Confining Geological Units from Deep Boreholes in the Potential Siting Regions Nördlich Lägern, Zürich Nordost and Jura Ost: Measurements and Predictive Sorption Modelling. Nagra Technischer Bericht NTB 23-01.

Marques Fernandes, M., Mazurek, M., Wersin, P., Wüst, R.A.J. & Baeyens, B. (2024b): Cation-exchange properties of the Mesozoic sedimentary sequence of Northern Switzerland and modelling of the Opalinus Clay porewater. Applied Geochemistry. DOI: 10.1016/ j.apgeochem.2023.105852.

Marques Fernandes, M., Vér, N. & Baeyens, B. (2015): Predicting the uptake of Cs, Co, Ni, Eu, Th and U on argillaceous rocks using sorption models for illite. Applied Geochemistry 59, 189-199. DOI: 10.1016/J.APGEOCHEM.2015.05.006.

Mazurek, M., Gimmi, T., Zwahlen, C., Aschwanden, L., Gaucher, E.C., Kiczka, M., Rufer, D., Wersin, P., Fernandes, M.M., Glaus, M.A., van Loon, L.R., Traber, D., Schnellmann, M. & Vietor, T. (2023): Swiss deep drilling campaign 2019–2022: Geological overview and rock properties with focus on porosity and pore-space architecture. Applied Geochemistry 159, 105839. DOI: 10.1016/j.apgeochem.2023.105839.

Miron, G.D., Kulik, D.A., Dmytrieva, V.S. & Wagner, T. (2015): GEMSFITS: Code package for optimization of geochemical model parameters and inverse modeling. Applied Geochemistry 55, 28-45. DOI: 10.1016/j.apgeochem.2014.10.013.

Motulsky, H. & Christopoulos, A. (2004): Fitting models to biological data using linear and non-linear regression: a practical guide to curve fitting. Oxford University Press, Oxford.

Müller-von Moos, M.; Kahr, G.; ETHZ, Institut für Grundbau und Bodenmechanik (1983): Mineralogische Untersuchungen von Wyoming Bentonit MX-80 und Montigel. Nagra Technischer Bericht. NTB 83-12.

Nagra (1985): Project Gewähr 1985: Nuclear Waste Management in Switzerland: Feasibility Studies and Safety Analyses. Nagra Project Report NGB 85-09.

Nagra (2002): Project Opalinus Clay: Safety report: Demonstration of disposal feasibility for spent fuel, vitrified high-level waste and long-lived intermediate-level waste (Entsorgungs-nachweis). Nagra Technical Report NTB 02-05.

Nagra (2024a): Abfallzuteilung und Betrachtungszeitraum für den Standortvergleich und Nachweiszeitraum für den Sicherheitsnachweis für das geologische Tiefenlager. Nagra Arbeitsbericht NAB 24-05.

Nagra (2024b): Geological properties of the Jura Ost, Nördlich Lägern and Zürich Nordost siting regions for safety assessment. Nagra Arbeitsbericht NAB 24-10.

Nagra (2024c): Geosynthesis of Northern Switzerland. Nagra Technical Report NTB 24-17.

Nagra (2024d): Radiological consequence analysis for a deep geological repository in Northern Switzerland. Nagra Technical Report NTB 24-18.

Nagra (2024e): Synthesis of the performance assessment for a deep geological repository for radioactive waste. Nagra Technical Report NTB 24-22.

OECD/NEA (2012): Chemical thermodynamics of Tin. NEA TDB Chemical Thermodynamics 12. OECD/NEA, Paris, available online at doi.org/10.1787/9789264992061-en.

Orucoglu, E., Grangeon, S., Gloter, A., Robinet, J.-C., Madé, B. & Tournassat, C. (2022): Competitive adsorption processes at clay mineral surfaces: A coupled experimental and modeling approach. ACS Earth and Space Chemistry 6/1, 144-159. DOI: 10.1021/acsearthspacechem.1c00323.

Payne, T.E., Brendler, V., Ochs, M., Baeyens, B., Brown, P.L., Davis, J.A., Ekberg, C., Kulik, D.A., Lutzenkirchen, J., Missana, T., Tachi, Y., van Loon, L.R. & Altmann, S. (2013): Guidelines for thermodynamic sorption modelling in the context of radioactive waste disposal. Environmental Modelling & Software 42, 143-156. DOI: 10.1016/J.ENVSOFT.2013.01.002.

Powell, K.J., Brown, P.L., Yiu, M., Byrne, R.H., Gajda, T., Leuz, A.-K., Sjöberg, S. & Wanner, H. (2009): Chemical speciation of environmentally significant metals with inorganic ligands. Part 3: The Pb^{2+} + OH^-, Cl^-, CO_3^{2-}, SO_4^{2-}, and PO_4^{3-} systems (IUPAC Technical Report). Pure and Applied Chemistry 81/12, 2425-2476.

Rand, M., Fuger, J., Grenthe, I., Neck, V. & Rai, D. (2009): Chemical Thermodynamics of Thorium. (Chemical Thermodynamics, 11). OECD Publishing, Paris.

Stipp, S., Gutmannsbauer, W. & Lehmann, T. (1996): The dynamic nature of calcite surfaces in air. American Mineralogist 81/1-2, 1-8. DOI: 10.2138/AM-1996-1-201.

Stipp, S.L., Eggleston, C.M. & Nielsen, B.S. (1994): Calcite surface structure observed at microtopographic and molecular scales with atomic force microscopy (AFM). Geochimica et Cosmochimica Acta 58/14, 3023-3033. DOI: 10.1016/0016-7037(94)90176-7.

Stockmann, M., Schikora, J., Becker, D.-A., Flügge, J., Noseck, U. & Brendler, V. (2017): Smart K_d-values, their uncertainties and sensitivities - Applying a new approach for realistic distribution coefficients in geochemical modeling of complex systems. Chemosphere 187, 277-285. DOI: 10.1016/j.chemosphere.2017.08.115.

Tennøe, S., Halnes, G. & Einevoll, G.T. (2018): Uncertainpy: A Python toolbox for uncertainty quantification and sensitivity analysis in computational neuroscience. Frontiers in Neuroinformatics 12, Article 49. DOI: 10.3389/FNINF.2018.00049.

Thoenen, T., Hummel, W., Berner, U.R. & Curti, E. (2014): The PSI / Nagra Chemical Thermodynamic Database 12 / 07. Nagra Arbeitsbericht NAB 14-49.

Vinograd, V.L., Kulik, D.A., Brandt, F., Klinkenberg, M., Weber, J., Winkler, B. & Bosbach, D. (2018): Thermodynamics of the solid solution - Aqueous solution system (Ba,Sr,Ra)SO_4 + H_2O: I. The effect of strontium content on radium uptake by barite. Applied Geochemistry 89, 59-74. DOI: 10.1016/j.apgeochem.2017.11.009.

App. A ClaySor model parameters

A.1 2SPNE SC/CE model parameters

Tab. A-1: Summary of 2SPNE SC/CE model parameters (site types, site capacities and protolysis constants) used in this report for illite and montmorillonite

Details in Marinich et al. (2024).

	Illite		**Montmorillonite**	
Site type	Capacity (mol kg^{-1})			
$\equiv S^{S}OH$	2. 0E-03			
$\equiv S^{W1}OH$	4. 0E-02			
$\equiv S^{W2}OH$	4. 0E-02			
Protolysis reactions	$\log_{10}K_{app}$			
	$\equiv S^{S/W1}OH$	$\equiv S^{W2}OH$	$\equiv S^{S/W1}OH$	$\equiv S^{W2}OH$
$\equiv SOH + H^{+} \Leftrightarrow \equiv SOH_2^{+}$	4.0	8.5	4.5	6.0
$\equiv SOH \Leftrightarrow \equiv SO^{-} + H^{+}$	-6.2	-10.5	-7.9	-10.5

$\equiv S^{S}OH$ is a strong site and $\equiv S^{W1}OH$ and $\equiv S^{W2}OH$ are weak sites

A.2 GCS model parameters

Tab. A-2: Summary of GCS model parameters (site types and capacities) and selectivity coefficients (K_c) for the cation exchange equilibria used in this report, for the three site types of illite for Cs^+, K^+, Ca^{2+}, Mg^{2+} and Sr^{2+} with regards to Na on illite with a CEC = 225 meq kg^{-1}

Details in Marinich et al. (2024).

Site type	**Frayed edge sites (FES)**	
% of CEC	0.25%	
Site capacity (meq kg^{-1})	0.5625	
Exchange equilibrium	**$\log_{10}[K_c]$**	**$\log_{10}[K_V]$**
$Cs^+ + Na^+$-illite ⇔ **Cs^+-illite** + Na^+	6.64 ± 0.05	6.64 ± 0.05
$K^+ + Na^+$-illite ⇔ **K^+-illite** + Na^+	2.4 ± 0.2	2.4 ± 0.2
$Ca^{2+} + 2Na^+$-illite ⇔ **Ca^{2+}-illite** + $2Na^+$	0.2 ± 0.1	-0.1 ± 0.1
$Mg^{2+} + 2Na^+$-illite ⇔ **Mg^{2+}-illite** + $2Na^+$	0.2 ± 0.1	-0.1 ± 0.1
$Sr^{2+} + 2Na^+$-illite ⇔ **Sr^{2+}-illite** + $2Na^+$	0.2 ± 0.1	-0.1 ± 0.1
Site type	**Type II sites (T2S)**	
% of CEC	20%	
Site capacity (meq kg^{-1})	45	
Exchange equilibrium	**$\log_{10}[K_c]$**	**$\log_{10}[K_V]$**
$Cs^+ + Na^+$-illite ⇔ **Cs^+-illite** + Na^+	3.03 ± 0.85	3.03 ± 0.85
$K^+ + Na^+$-illite ⇔ **K^+-illite** + Na^+	2.1 ± 0.2	2.1 ± 0.2
$Ca^{2+} + 2Na^+$-illite ⇔ **Ca^{2+}-illite** + $2Na^+$	0.0 ± 0.1	-0.3 ± 0.1
$Mg^{2+} + 2Na^+$-illite ⇔ **Mg^{2+}-illite** + $2Na^+$	0.0 ± 0.1	-0.3 ± 0.1
$Sr^{2+} + 2Na^+$-illite ⇔ **Sr^{2+}-illite** + $2Na^+$	0.0 ± 0.1	-0.3 ± 0.1
Site type	**Planar sites (PS)**	
% of CEC	~80%	
Site capacity (meq kg^{-1})	180	
Exchange equilibrium	**$\log_{10}[K_c]$**	**$\log_{10}[K_V]$**
$Cs^+ + Na^+$-illite ⇔ **Cs^+-illite** + Na^+	1.49 ± 0.74	1.49 ± 0.74
$K^+ + Na^+$-illite ⇔ **K^+-illite** + Na^+	1.1 ± 0.2	1.1 ± 0.2
$Ca^{2+} + 2Na^+$-illite ⇔ **Ca^{2+}-illite** + $2Na^+$	0.4 ± 0.2	0.1 ± 0.2
$Mg^{2+} + 2Na^+$-illite ⇔ **Mg^{2+}-illite** + $2Na^+$	0.4 ± 0.2	0.1 ± 0.2
$Sr^{2+} + 2Na^+$-illite ⇔ **Sr^{2+}-illite** + $2Na^+$	0.4 ± 0.2	0.1 ± 0.2

A.3 Cation exchange selectivity coefficients

Tab. A-3: CE reactions and corresponding selectivity coefficients (K_c and K_V) for Na-illite used in this report

Details in Marinich et al. (2024).

CE reaction	**$\log_{10}[K_c]$**	**$\log_{10}[K_V]$**
Na^+-clay + Cs^+ ⇔ **Cs^+-clay** + Na^+	1.49 ± 0.74	1.49 ± 0.74
Na^+-clay + K^+ ⇔ **K^+-clay** + Na^+	1.1 ± 0.2	1.1 ± 0.2
$2Na^+$-clay + Ba^{2+} ⇔ **Ba^{2+}-clay** + $2Na^+$	1.05	0.75
$2Na^+$-clay + Ca^{2+} ⇔ **Ca^{2+}-clay** + $2Na^+$	0.4 ± 0.2	0.1 ± 0.2
$2Na^+$-clay + Fe^{2+} ⇔ **Fe^{2+}-clay** + $2Na^+$	0.60	0.3
$2Na^+$-clay + Mg^{2+} ⇔ **Mg^{2+}-clay** + $2Na^+$	0.4 ± 0.2	0.1 ± 0.2
$2Na^+$-clay + Mn^{2+} ⇔ **Mn^{2+}-clay** + $2Na^+$	0.41 ± 0.47	0.11 ± 0.47
$2Na^+$-clay + Ni^{2+} ⇔ **Ni^{2+}-clay** + $2Na^+$	0.73 ± 0.07	0.43 ± 0.07
$2Na^+$-clay + Pb^{2+} ⇔ **Pb^{2+}-clay** + $2Na^+$	2.28 ± 0.65	1.98 ± 0.65
$2Na^+$-clay + Ra^{2+} ⇔ **Ra^{2+}-clay** + $2Na^+$	3.22 ± 0.12	2.92 ± 0.12
$2Na^+$-clay + Sr^{2+} ⇔ **Sr^{2+}-clay** + $2Na^+$	0.4 ± 0.2	0.1 ± 0.2
$3Na^+$-clay + Am^{3+} ⇔ **Am^{3+}-clay** + $3Na^+$	1.71 ± 0.09	1.23 ± 0.09
$3Na^+$-clay + Eu^{3+} ⇔ **Eu^{3+}-clay** + $3Na^+$	1.78 ± 0.15	1.3 ± 0.15
Na^+-clay + NpO_2^+ ⇔ **NpO_2^+-clay** + Na^+	0.04 ± 0.45	0.04 ± 0.45
$2Na^+$-clay + UO_2^{2+} ⇔ **UO_2^{2+}-clay** + $2Na^+$	0.65	0.35

Tab. A-4: CE reactions and corresponding selectivity coefficients (log K_c) for Na-montmorillonite used in this report

Details in Marinich et al. (2024).

CE reaction	**log [K_c]**	**log [K_V]**
Na^+-clay + Cs^+ ⇔ **Cs^+-clay** + Na^+	1.10 ± 0.37	1.10 ± 0.37
Na^+-clay + K^+ ⇔ **K^+-clay** + Na^+	0.602 ± 0.22	0.602 ± 0.22
$2Na^+$-clay + Ba^{2+} ⇔ **Ba^{2+}-clay** + $2Na^+$	0.9	0.6
$2Na^+$-clay + Ca^{2+} ⇔ **Ca^{2+}-clay** + $2Na^+$	0.415 ± 0.27	0.095 ± 0.27
$2Na^+$-clay + Fe^{2+} ⇔ **Fe^{2+}-clay** + $2Na^+$	1.33 ± 0.11	1.03 ± 0.11
$2Na^+$-clay + Mg^{2+} ⇔ **Mg^{2+}-clay** + $2Na^+$	0.342 ± 0.3	0.03 ± 0.3
$2Na^+$-clay + Mn^{2+} ⇔ **Mn^{2+}-clay** + $2Na^+$	0.48 ± 0.09	0.18 ± 0.09
$2Na^+$-clay + Ni^{2+} ⇔ **Ni^{2+}-clay** + $2Na^+$	0.57 ± 0.06	0.27 ± 0.06
$2Na^+$-clay + Pb^{2+} ⇔ **Pb^{2+}-clay** + $2Na^+$	1.18 ± 0.37	0.88 ± 0.37
$2Na^+$-clay + Ra^{2+} ⇔ **Ra^{2+}-clay** + $2Na^+$	1.34 ± 0.13	1.03 ± 0.13
$2Na^+$-clay + Sr^{2+} ⇔ **Sr^{2+}-clay** + $2Na^+$	0.415 ± 0.27	0.113 ± 0.27
$3Na^+$-clay + Am^{3+} ⇔ **Am^{3+}-clay** + $3Na^+$	1.64 ± 0.09	1.16 ± 0.09
$3Na^+$-clay + Eu^{3+} ⇔ **Eu^{3+}-clay** + $3Na^+$	1.53 ± 0.14	1.06 ± 0.14
Na^+-clay + NpO_2^+ ⇔ **NpO_2^+-clay** + Na^+	0.04 ± 0.12	0.04 ± 0.12
$2Na^+$-clay + UO_2^{2+} ⇔ **UO_2^{2+}-clay** + $2Na^+$	0.46 ± 0.3	0.16 ± 0.3

A.4 Surface complexation equilibrium constants

Tab. A-5: SC reactions and equilibrium constants for Na-illite used in this report
Details in Marinich et al. (2024).

SC formation reaction	$\log_{10}{}^{S}K$	$\log_{10}{}^{W1}K$
$\equiv SOH + Fe^{2+} \Leftrightarrow \mathbf{\equiv SOFe^{+}} + H^{+}$	1.28	-1.54
$\equiv SOH + Mn^{2+} \Leftrightarrow \mathbf{\equiv SOMn^{+}} + H^{+}$	0.98 ± 0.09	-2.4 ± 0.24
$\equiv SOH + Ni^{2+} \Leftrightarrow \mathbf{\equiv SONi^{+}} + H^{+}$ $\equiv SOH + Ni^{2+} + H_2O \Leftrightarrow \mathbf{\equiv SONiOH^{0}} + 2H^{+}$	0.65 ± 0.04 -7.92 ± 0.15	-1.92 ± 0.12
$\equiv SOH + Pb^{2+} \Leftrightarrow \mathbf{\equiv SOPb^{+}} + H^{+}$ $\equiv SOH + Pb^{2+} + H_2O \Leftrightarrow \mathbf{\equiv SOPbOH^{0}} + 2H^{+}$	2.90 ± 0.22 -5.11 ± 0.24	0.70 ± 0.29
$\equiv SOH + Am^{3+} \Leftrightarrow \mathbf{\equiv SOAm^{2+}} + H^{+}$ $\equiv SOH + Am^{3+} + H_2O \Leftrightarrow \mathbf{\equiv SOAmOH^{+}} + 2H^{+}$ $\equiv SOH + Am^{3+} + 2H_2O \Leftrightarrow \mathbf{\equiv SOAm(OH)_2^{0}} + 3H^{+}$	2.69 ± 0.26 -5.17 ± 1.55 -12.96 ± 0.07	
$\equiv SOH + Cm^{3+} \Leftrightarrow \mathbf{\equiv SOCm^{2+}} + H^{+}$ $\equiv SOH + Cm^{3+} + H_2O \Leftrightarrow \mathbf{\equiv SOCmOH^{+}} + 2H^{+}$	2.56 ± 0.2 -3.18 ± 0.38	
$\equiv SOH + Eu^{3+} \Leftrightarrow \mathbf{\equiv SOEu^{2+}} + H^{+}$ $\equiv SOH + Eu^{3+} + H_2O \Leftrightarrow \mathbf{\equiv SOEuOH^{+}} + 2H^{+}$ $\equiv SOH + Eu^{3+} + 3H_2O \Leftrightarrow \mathbf{\equiv SOEu(OH)_3^{-}} + 4H^{+}$	2.47 ± 0.4 -4.28 ± 0.17 -21.34 ± 0.17	1.00 ± 0.19
$\equiv SOH + Pu^{3+} \Leftrightarrow \mathbf{\equiv SOPu^{2+}} + H^{+}$ $\equiv SOH + Pu^{3+} + H_2O \Leftrightarrow \mathbf{\equiv SOPuOH^{+}} + 2H^{+}$ $\equiv SOH + Pu^{3+} + 2H_2O \Leftrightarrow \mathbf{\equiv SOPu(OH)_2^{0}} + 3H^{+}$	2.62 -3.88 -13	
$\equiv SOH + Np^{4+} \Leftrightarrow \mathbf{\equiv SONp^{3+}} + H^{+}$ $\equiv SOH + Np^{4+} + H_2O \Leftrightarrow \mathbf{\equiv SONpOH^{2+}} + 2H^{+}$ $\equiv SOH + Np^{4+} + 2H_2O \Leftrightarrow \mathbf{\equiv SONp(OH)_2^{+}} + 3H^{+}$ $\equiv SOH + Np^{4+} + 3H_2O \Leftrightarrow \mathbf{\equiv SONp(OH)_3^{0}} + 4H^{+}$	9.77 9.56 6.23 0.43	
$\equiv SOH + Pu^{4+} \Leftrightarrow \mathbf{\equiv SOPu^{3+}} + H^{+}$ $\equiv SOH + Pu^{4+} + H_2O \Leftrightarrow \mathbf{\equiv SOPuOH^{2+}} + 2H^{+}$ $\equiv SOH + Pu^{4+} + 2H_2O \Leftrightarrow \mathbf{\equiv SOPu(OH)_2^{+}} + 3H^{+}$ $\equiv SOH + Pu^{4+} + 3H_2O \Leftrightarrow \mathbf{\equiv SOPu(OH)_3^{0}} + 4H^{+}$	9.19 7.92 5.92 -0.63	
$\equiv SOH + Sn^{4+} + 3H_2O \Leftrightarrow \mathbf{\equiv SOSn(OH)_3^{0}} + 4H^{+}$ $\equiv SOH + Sn^{4+} + 4H_2O \Leftrightarrow \mathbf{\equiv SOSn(OH)_4^{-}} + 5H^{+}$ $\equiv SOH + Sn^{4+} + 5H_2O \Leftrightarrow \mathbf{\equiv SOSn(OH)_5^{2-}} + 6H^{+}$	15.86 ± 0.20 9.53 ± 0.29 1.02 ± 0.13	

Tab. A-5: Cont.

SC formation reaction	$\log_{10}{}^{S}K$	$\log_{10}{}^{W1}K$
≡SOH + Th^{4+} ⇔ **≡SOTh^{3+}** + H^+	6.73 ± 1.61	
≡SOH + Th^{4+} + H_2O ⇔ **≡SOThOH^{2+}** + $2H^+$	2.41 ± 0.91	
≡SOH + Th^{4+} + $3H_2O$ ⇔ **≡SOTh(OH)$_3^0$** + $4H^+$	-9.12 ± 1.56	
≡SOH + Th^{4+} + $4H_2O$ ⇔ **≡SOTh(OH)$_4^-$** + $5H^+$	-15.20 ± 0.13	
≡SOH + U^{4+} ⇔ **≡SOU^{3+}** + H^+	8.62	
≡SOH + U^{4+} + H_2O ⇔ **≡SOUOH^{2+}** + $2H^+$	7.18	
≡SOH + U^{4+} + $2H_2O$ ⇔ **≡SOU(OH)$_2^+$** + $3H^+$	3.7	
≡SOH + U^{4+} + $3H_2O$ ⇔ **≡SOU(OH)$_3^0$** + $4H^+$	-1.36	
≡SOH + $Nb(OH)_4^+$ + H_2O ⇔ **≡SONb(OH)$_5^-$** + $2H^+$	0.74 ± 0.22	
≡SOH + $Nb(OH)_4^+$ + $2H_2O$ ⇔ **≡SONb(OH)$_6^{2-}$** + $3H^+$	-5.74 ± 0.54	
≡SOH + NpO_2^+ ⇔ **≡SONpO$_2^0$** + H^+	-1.32 ± 0.22	
≡SOH + NpO_2^+ + H_2O ⇔ **≡SONpO$_2$OH$^-$** + $2H^+$	-10.06 ± 0.36	
≡SOH + $PaOOH^{+2}$ ⇔ **≡SOPaOOH$^+$** + H^+	6.51 ± 0.13	
≡SOH + $PaOOH^{+2}$ + H_2O ⇔ **≡SOPaO$_2$OH$^-$** + $3H^+$	-4.89 ± 0.14	
≡SOH + $PaOOH^{+2}$ + $2H_2O$ ⇔ **≡SOPaO$_2$(OH)$_2^{2-}$** + $4H^+$	-14.00 ± 0.21	
≡SOH + UO_2^{2+} ⇔ **≡SOUO$_2^+$** + H^+	2.37 ± 0.17	-0.83 ± 0.23
≡SOH + UO_2^{2+} + H_2O ⇔ **≡SOUO$_2$OH^0** + $2H^+$	-4.43 ± 0.82	-5.60 ± 0.13
≡SOH + UO_2^{2+} + $2H_2O$ ⇔ **≡SOUO$_2$(OH)$_2^-$** + $3H^+$	-11.07 ± 0.26	-12.32 ± 0.15
≡SOH + UO_2^{2+} + $3H_2O$ ⇔ **≡SOUO$_2$(OH)$_3^{2-}$** + $4H^+$	-19.29 ± 0.18	

Tab. A-6: SC reactions and equilibrium constants for Na-montmorillonite, as used in this report Details in Marinich et al. (2024).

SC formation reaction	$\log_{10}{}^{S}K$	$\log_{10}{}^{W1}K$
$\equiv SOH + Fe^{2+} \Leftrightarrow \equiv \mathbf{SOFe^{+}} + H^{+}$	1.70 ± 0.17	-1.62 ± 0.24
$\equiv SOH + Mn^{2+} \Leftrightarrow \equiv \mathbf{SOMn^{+}} + H^{+}$	-0.63 ± 0.17	-3.48 ± 0.12
$\equiv SOH + Ni^{2+} \Leftrightarrow \equiv \mathbf{SONi^{+}} + H^{+}$ $\equiv SOH + Ni^{2+} + H_2O \Leftrightarrow \equiv \mathbf{SONiOH^{0}} + 2H^{+}$	-0.81 ± 0.06 -9.43 ± 0.08	-3.54 ± 0.26
$\equiv SOH + Pb^{2+} \Leftrightarrow \equiv \mathbf{SOPb^{+}} + H^{+}$ $\equiv SOH + Pb^{2+} + H_2O \Leftrightarrow \equiv \mathbf{SOPbOH^{0}} + 2H^{+}$	1.37 ± 0.15 -7.78 ± 0.53	-1.30 ± 0.25
$\equiv SOH + Am^{3+} \Leftrightarrow \equiv \mathbf{SOAm^{2+}} + H^{+}$ $\equiv SOH + Am^{3+} + 2H_2O \Leftrightarrow \equiv \mathbf{SOAm(OH)_2^{0}} + 3H^{+}$	2.32 ± 0.12 -14.68 ± 0.15	
$\equiv SOH + Eu^{3+} \Leftrightarrow \equiv \mathbf{SOEu^{2+}} + H^{+}$ $\equiv SOH + Eu^{3+} + H_2O \Leftrightarrow \equiv \mathbf{SOEuOH^{+}} + 2H^{+}$ $\equiv SOH + Eu^{3+} + 3H_2O \Leftrightarrow \equiv \mathbf{SOEu(OH)_3^{-}} + 4H^{+}$	1.65 ± 0.10 -6.23 ± 0.3 -22.17 ± 0.17	-0.45 ± 0.16
$\equiv SOH + Pu^{3+} \Leftrightarrow \equiv \mathbf{SOPu^{2+}} + H^{+}$ $\equiv SOH + Pu^{3+} + H_2O \Leftrightarrow \equiv \mathbf{SOPuOH^{+}} + 2H^{+}$ $\equiv SOH + Pu^{3+} + 2H_2O \Leftrightarrow \equiv \mathbf{SOPu(OH)_2^{0}} + 3H^{+}$	1.91 -4.73 -14.07	
$\equiv SOH + Np^{4+} \Leftrightarrow \equiv \mathbf{SONp^{3+}} + H^{+}$ $\equiv SOH + Np^{4+} + H_2O \Leftrightarrow \equiv \mathbf{SONpOH^{2+}} + 2H^{+}$ $\equiv SOH + Np^{4+} + 2H_2O \Leftrightarrow \equiv \mathbf{SONp(OH)_2^{+}} + 3H^{+}$ $\equiv SOH + Np^{4+} + 3H_2O \Leftrightarrow \equiv \mathbf{SONp(OH)_3^{0}} + 4H^{+}$	10.19 9.97 6.56 0.59	
$\equiv SOH + Pu^{4+} \Leftrightarrow \equiv \mathbf{SOPu^{3+}} + H^{+}$ $\equiv SOH + Pu^{4+} + H_2O \Leftrightarrow \equiv \mathbf{SOPuOH^{2+}} + 2H^{+}$ $\equiv SOH + Pu^{4+} + 2H_2O \Leftrightarrow \equiv \mathbf{SOPu(OH)_2^{+}} + 3H^{+}$ $\equiv SOH + Pu^{4+} + 3H_2O \Leftrightarrow \equiv \mathbf{SOPu(OH)_3^{0}} + 4H^{+}$	9.59 8.29 6.23 -0.5	
$\equiv SOH + Sn^{4+} + 3H_2O \Leftrightarrow \equiv \mathbf{SOSn(OH)_3^{0}} + 4H^{+}$ $\equiv SOH + Sn^{4+} + 4H_2O \Leftrightarrow \equiv \mathbf{SOSn(OH)_4^{-}} + 5H^{+}$ $\equiv SOH + Sn^{4+} + 5H_2O \Leftrightarrow \equiv \mathbf{SOSn(OH)_5^{2-}} + 6H^{+}$	16.23 ± 0.16 -0.67 ± 0.11	13.74 ± 0.24 6.22 ± 0.17
$\equiv SOH + Th^{4+} \Leftrightarrow \equiv \mathbf{SOTh^{3+}} + H^{+}$ $\equiv SOH + Th^{4+} + H_2O \Leftrightarrow \equiv \mathbf{SOThOH^{2+}} + 2H^{+}$ $\equiv SOH + Th^{4+} + 3H_2O \Leftrightarrow \equiv \mathbf{SOTh(OH)_3^{0}} + 4H^{+}$ $\equiv SOH + Th^{4+} + 4H_2O \Leftrightarrow \equiv \mathbf{SOTh(OH)_4^{-}} + 5H^{+}$	7.30 ± 0.33 2.31 ± 0.86 -9.15 ± 0.29 -16.88 ± 0.17	
$\equiv SOH + U^{4+} \Leftrightarrow \equiv \mathbf{SOU^{3+}} + H^{+}$ $\equiv SOH + U^{4+} + H_2O \Leftrightarrow \equiv \mathbf{SOUOH^{2+}} + 2H^{+}$ $\equiv SOH + U^{4+} + 2H_2O \Leftrightarrow \equiv \mathbf{SOU(OH)_2^{+}} + 3H^{+}$ $\equiv SOH + U^{4+} + 3H_2O \Leftrightarrow \equiv \mathbf{SOU(OH)_3^{0}} + 4H^{+}$	9.01 7.53 3.95 -1.26	

Tab. A-6: Cont.

SC formation reaction	$\log_{10}{}^{S}K$	$\log_{10}{}^{W1}K$
$\equiv SOH + Nb(OH)_4^+ + H_2O \Leftrightarrow \mathbf{\equiv SONb(OH)_5^-} + 2H^+$	**0.73 ± 0.23**	**-2.40 ± 0.23**
$\equiv SOH + Nb(OH)_4^+ + 2H_2O \Leftrightarrow \mathbf{\equiv SONb(OH)_6^{2-}} + 3H^+$		**-11.11 ± 0.65**
$\equiv SOH + NpO_2^+ \Leftrightarrow \mathbf{\equiv SONpO_2^0} + H^+$	-2.63 ± 0.11	
$\equiv SOH + NpO_2^+ + H_2O \Leftrightarrow \mathbf{\equiv SONpO_2OH^-} + 2H^+$	-12.56 ± 0.23	
$\equiv SOH + PaOOH^{+2} \Leftrightarrow \mathbf{\equiv SOPaOOH^+} + H^+$	6.71 ± 0.20	
$\equiv SOH + PaOOH^{+2} \Leftrightarrow \mathbf{\equiv SOPaO_2^0} + 2H^+$	1.04 ± 0.28	
$\equiv SOH + PaOOH^{+2} + H_2O \Leftrightarrow \mathbf{\equiv SOPaO_2OH^-} + 3H^+$	-6.79 ± 0.31	
$\equiv SOH + PaOOH^{+2} + 2H_2O \Leftrightarrow \mathbf{\equiv SOPaO_2(OH)_2^{2-}} + 4H^+$	-15.95 ± 0.23	
$\equiv SOH + UO_2^{2+} \Leftrightarrow \mathbf{\equiv SOUO_2^+} + H^+$	2.93 ± 0.10	0.07 ± 0.31
$\equiv SOH + UO_2^{2+} + H_2O \Leftrightarrow \mathbf{\equiv SOUO_2OH^0} + 2H^+$	-4.21 ± 0.40	-5.83 ± 0.33
$\equiv SOH + UO_2^{2+} + 3H_2O \Leftrightarrow \mathbf{\equiv SOUO_2(OH)_3^{2-}} + 4H^+$	-21.12 ± 0.69	

Tab. A-7: SC constants for Ra(II) on weak 2-type sites, $\equiv S^{W2}OH$, of illite and montmorillonite as used in this report

Details in Marinich et al. (2024). At porewater conditions only CE of Ra is dominant.

Mineral	Surface complex formation reaction	$\log_{10}{}^{w2}K$
Illite	$\equiv SOH + Ra^{2+} \Leftrightarrow \mathbf{\equiv SORa^+} + H^+$	-3.85 ± 0.30
Montmorillonite		-4.80 ± 0.21

App. B Metal hydrolysis equilibrium constants

Tab. B-1: Hydrolysis reactions and values for the constants from the PSI/Nagra TDB 2020 used in this report

The original references are supplied, except for the Co(II) data, which were taken from the ThermoChimie thermodynamic database, version 11a (Giffaut et al. 2014).

Metal	Hydrolysis reactions	log ^{OH}K	Reference
Fe(II)	$Fe^{2+} + H_2O \Leftrightarrow FeOH^+ + H^+$	-9.43	Brown & Ekberg (2016)
	$Fe^{2+} + 2H_2O \Leftrightarrow Fe(OH)_2^0 + 2H^+$	-20.52	
	$Fe^{2+} + 3H_2O \Leftrightarrow Fe(OH)_3^- + 3H^+$	-32.68	
Mn(II)	$Mn^{2+} + H_2O \Leftrightarrow MnOH^+ + H^+$	-10.58	Brown & Ekberg (2016)
	$Mn^{2+} + 2H_2O \Leftrightarrow Mn(OH)_2^0 + 2H^+$	-22.18	
	$Mn^{2+} + 3H_2O \Leftrightarrow Mn(OH)_3^- + 3H^+$	-34.34	
	$Mn^{2+} + 4H_2O \Leftrightarrow Mn(OH)_4^{2-} + 4H^+$	-48.28	
Ni(II)	$Ni^{2+} + H_2O \Leftrightarrow NiOH^+ + H^+$	-9.54	Gamsjäger et al. (2005)
	$Ni^{2+} + 2H_2O \Leftrightarrow Ni(OH)_2^0 + 2H^+$	-18	
	$Ni^{2+} + 3H_2O \Leftrightarrow Ni(OH)_3^- + 3H^+$	-29.2	
Pb(II)	$Pb^{2+} + H_2O \Leftrightarrow PbOH^+ + H^+$	-7.46	Powell et al. (2009)
	$Pb^{2+} + 2H_2O \Leftrightarrow Pb(OH)_2^0 + 2H^+$	-16.94	
	$Pb^{2+} + 3H_2O \Leftrightarrow Pb(OH)_3^- + 3H^+$	-28.03	
Ra(II)	$Ra^{2+} + H_2O \Leftrightarrow RaOH^+ + H^+$	-13.7	Hummel & Thoenen (2023) (linear regression)
Am(III)	$Am^{3+} + H_2O \Leftrightarrow AmOH^{2+} + H^+$	-7.2	Guillaumont et al. (2003)
	$Am^{3+} + 2H_2O \Leftrightarrow Am(OH)_2^+ + 2H^+$	-15.1	
	$Am^{3+} + 3H_2O \Leftrightarrow Am(OH)_3^0 + 3H^+$	-26.2	
Eu(III)	$Eu^{3+} + H_2O \Leftrightarrow EuOH^{2+} + H^+$	-7.64	Hummel et al. (2002)
	$Eu^{3+} + 2H_2O \Leftrightarrow Eu(OH)_2^+ + 2H^+$	-15.1	
	$Eu^{3+} + 3H_2O \Leftrightarrow Eu(OH)_3^0 + 3H^+$	-23.7	
	$Eu^{3+} + 4H_2O \Leftrightarrow Eu(OH)_4^- + 4H^+$	-36.2	
Sn(IV)	$Sn^{4+} + 4H_2O \Leftrightarrow Sn(OH)_4^0 + 4H^+$	7.54	OECD/NEA (2012)
	$Sn^{4+} + 5H_2O \Leftrightarrow Sn(OH)_5^- + 5H^+$	-8.6	
	$Sn^{4+} + 6H_2O \Leftrightarrow Sn(OH)_6^{2-} + 6H^+$	-18.67	

Tab. B-1: Cont.

Metal	Hydrolysis reactions	log ^{OH}K	Reference
Th(IV)	$Th^{4+} + H_2O \Leftrightarrow ThOH^{3+} + H^+$	-2.5	Rand et al. (2009)
	$Th^{4+} + 2H_2O \Leftrightarrow Th(OH)_2^{2+} + 2H^+$	-6.2	
	$Th^{4+} + 4H_2O \Leftrightarrow Th(OH)_4^0 + 4H^+$	-17.4	
Nb(V)	$Nb(OH)_4^+ + H_2O \Leftrightarrow Nb(OH)_5^0 + H^+$	-1.89	Hummel & Thoenen (2023)
	$Nb(OH)^{4+} + 2H_2O \Leftrightarrow Nb(OH)_6^- + 2H^+$	-6.69	
	$Nb(OH)^{4+} + 3H_2O \Leftrightarrow Nb(OH)_7^{2-} + 3H^+$	-16.09	
Np(V)	$NpO_2^+ + H_2O \Leftrightarrow NpO_2(OH)^0 + H^+$	-11.3	Lemire et al. (2001)
	$NpO_2^+ + 2H_2O \Leftrightarrow NpO_2(OH)_2^- + 2H^+$	-23.6	
Pa(V)	$PaO(OH)^{2+} + H_2O \Leftrightarrow PaO(OH)_2^+ + H^+$	-1.26	Hummel & Thoenen (2023)
	$PaO(OH)_2^+ + H_2O \Leftrightarrow PaO(OH)_3^0 + H^+$	-5.04	
	$PaO(OH)_3^0 + H_2O \Leftrightarrow PaO(OH)_4^- + H^+$	-9.4	
U(VI)	$UO_2^{2+} + H_2O \Leftrightarrow UO_2OH^+ + H^+$	-5.25	Guillaumont et al. (2003)
	$UO_2^{2+} + 2H_2O \Leftrightarrow UO_2(OH)_2^0 + 2H^+$	-12.15	"
	$UO_2^{2+} + 3H_2O \Leftrightarrow UO_2(OH)_3^- + 3H^+$	-20.25	"
	$UO_2^{2+} + 4H_2O \Leftrightarrow UO_2(OH)_4^{2-} + 4H^+$	-32.4	"
	$2UO_2^{2+} + H_2O \Leftrightarrow (UO_2)_2OH^{3+} + H^+$	-2.7	Grenthe et al. (1992)
	$2UO_2^{2+} + 2H_2O \Leftrightarrow (UO_2)_2(OH)_2^{2+} + 2H^+$	-5.62	"
	$3UO_2^{2+}\ 4H_2O \Leftrightarrow (UO_2)_3(OH)_4^{2+} + 4H^+$	-11.9	"
	$3UO_2^{2+}\ 5H_2O \Leftrightarrow (UO_2)_3(OH)_5^+ + 5H^+$	-15.55	"
	$3UO_2^{2+}\ 7H_2O \Leftrightarrow (UO_2)_3(OH)_7^- + 7H^+$	-32.2	Guillaumont et al. (2003)
	$4UO_2^{2+}\ 7H_2O \Leftrightarrow (UO_2)_4(OH)_7^+ + 7H^+$	-21.9	Grenthe et al. (1992)

App. C Comparison of the reference SDB-E2 and SDB-E3 for Opalinus Clay and MX-80

The SDBs for Opalinus Clay and MX-80 bentonite in the present report, denoted as SDB-E3, are compared with the corresponding SDBs from SGT-E2 in NTB 12-04 (Baeyens et al. 2014b). Details on the new calculation methodology used for SDB-E3 compared to SDB-E2 are described in Chapter 2. The comparison is limited to the SDBs for Opalinus Clay (*Tab. 5.2* in NTB 12-04) and MX-80 bentonite (*Tab. 8.6* in NTB 12-04) for the reference porewater compositions. A key point to note is that SDB-E2 was derived for an illite/smectite content of 33 wt.% for Opalinus Clay (see *Tab. 3.1* in NTB 12-04) and a montmorillonite content of 75 wt.% for MX-80 bentonite (*Tab. 8.1* in NTB 12-04). Thus, to facilitate comparison in the following figures, the R_d values for SDB-E3 are taken from the LUTs at the corresponding clay mineral contents of Opalinus Clay (33 wt.%) and MX-80 bentonite (75 wt.%). Following this procedure, the comparison will show the difference in R_d values under the most comparable conditions. The error bars for SDB-E2 data represent the model uncertainty factor from Baeyens et al. (2014b). For SDB-E3, the error bars depict the upper and lower values of the 95% confidence interval derived from uncertainties of model parameters, detailed in Chapter 6. For elements C, Ca, Sr, Pu, Np and U with no model uncertainty, based on available measured data, the error bars represent an assumed model uncertainty factor of 3, as in Baeyens et al. (2014b).

The reference porewaters for Opalinus Clay and MX-80 bentonite used for the two SDBs are not identical. The MX-80 bentonite porewater composition for SGT-E2 is found in *Tab. 8.2* of NTB 12-04, while for this report it is summarised in Tab. 3-1. For Opalinus Clay, the porewater composition for SGT-E2 is given in *Tab. 3.8* of NTB 12-04, while for the present report it is compiled in Tab. 3-2. With respect to pH, ionic strength, pe and C_{inorg}, the reference porewater for JO resembles the reference Opalinus Clay porewater of Stage 2 and the reference SDB for JO is thus selected for the comparison. In the case of MX-80 bentonite, there is only one reference porewater and this is similar for both SDBs of Stage 2 and Stage 3.

The results of the R_d data comparison of SDB-E2 and SDB-E3 for Opalinus Clay from JO and MX-80 bentonite are shown in Fig. C-1 and Fig. C-2, respectively.

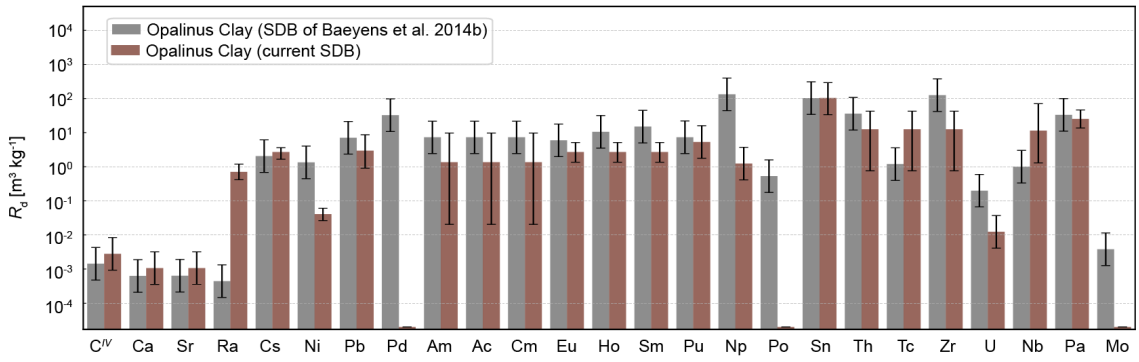

Fig. C-1: Comparison of calculated R_d values for Opalinus Clay for SGT-E2 (Baeyens et al. 2014b) (grey bars) and this report using the new methodology (brown bars)

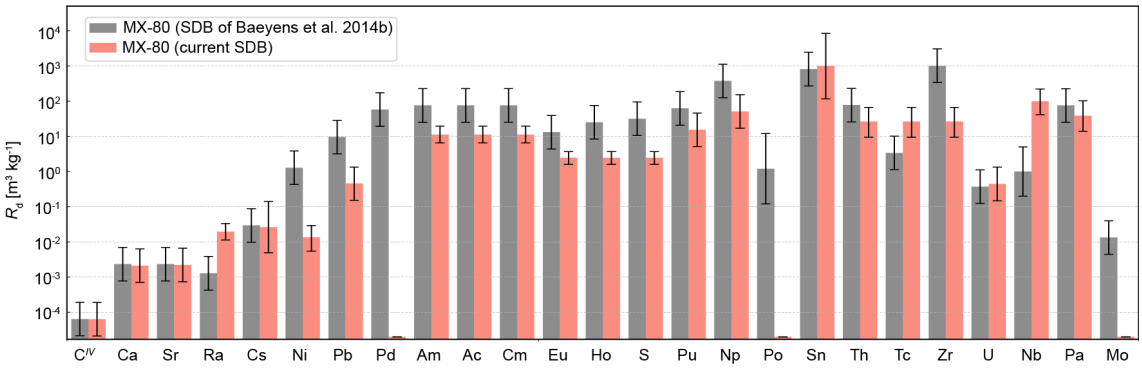

Fig. C-2: Comparison of calculated R_d values for MX-80 bentonite for SGT-E2 (Baeyens et al. 2014b) (grey bars) and this current report using the new methodology (pink bars)

For most elements that show differences, the newly calculated R_d values are smaller when compared to those of the previous SDB-E2. As a result of the updates to the PSI/Nagra TDB 2020 of the aqueous thermodynamic database, the elements Pd, Po and Mo are predicted to be present as non-sorbing aqueous species (i.e. Me^0) (Section 4.6), hence their vastly decreased R_d values in this report. For Ni and Pb, the R_d value decrease is due to the competition with ferrous iron and manganese that are present in the porewater in significant concentrations (10^{-5} to 10^{-4} M). This competition was not accounted for in the SDB-E2 calculations. The decrease in the calculated R_d values for the trivalent radionuclides Am, Ac, Cm, Eu, Ho, Sm and Pu is due to the new sorption model derived from experimental data (Marinich et al. 2024) and updates to the standard properties of aqueous species in the PSI/Nagra TDB 2020.

The R_d values of Zr are different since they were previously taken from Sn as chemical analogue, whereas in this report Th was taken as an analogue for Zr (Section 4.4). The R_d decrease for Np, predicted to be present as Np^{IV}, is due to changes to the aqueous speciation model arising from the addition of the dominant $Np^{IV}(OH)_2(CO_3)_2^{2-}$ species in the PSI/Nagra TDB 2020 update (Hummel & Thoenen 2023). As this anionic species is assumed to be non-sorbing, the model predicts a decrease in R_d compared to the SDB of SGT-E2. For U, the decreased R_d values in this report arise from changes in the aqueous speciation due to calcium-uranyl-carbonate species being significantly more stable in the updated PSI/Nagra TDB 2020 database (Hummel & Thoenen 2023), which leads to lower calculated R_d values.

Higher R_d values compared to the SDB of SGT-E2 are calculated for the elements Ra, Tc and Nb. For Ra, this arises from a new model based on recent experimental data (Marinich et al. 2024). For the current SDB, the Tc values were taken from Th by analogy, while in the SDB of SGT-E2, its value was estimated to be lower than Th and additionally reduced through the Tc speciation factor. No measured source data were available for the uptake of Nb on clay minerals and its R_d values in the SDB of SGT-E2 were estimated based on conservative assumptions. Since then, a Nb sorption model was derived in Marinich et al. (2024) based on experimental data, which was used in the calculations for this report.

Finally, the R_d values for inorganic C^{IV} are almost identical in SDB-E2 and SDB-E3 for both MX-80 bentonite and Opalinus Clay. The differences in R_d values for C^{IV} are solely due to the differences in C^{IV} concentrations in the refence porewater compositions in both SDBs. It should be noted that the R_d values for the SDB of this report are taken from Tab. 4-8 (which refer to 100 wt.% calcite), which were scaled to the same calcite content fractions of 0.7 wt.% (MX-80 bentonite) and 13 wt.% (Opalinus Clay) used in the SDB of SGT-E2.